Dissertation

submitted to the
Combined Faculty of Natural Sciences and Mathematics
of Heidelberg University, Germany
for the degree of
Doctor of Natural Sciences

Put forward by
Patrick Froß
born in: Koblenz
Oral examination: 13.10.2020

Electron-nuclear correlation, singly-excited Rydberg states and electron emission asymmetry in multiphoton ionization of H_2

Referees: Priv.-Doz. Dr. Robert Moshammer

Apl. Prof. Dr. Andreas Wolf

Abstract In this thesis multiphoton ionization of molecular hydrogen is investigated by using 50 fs laser pulses with 400 nm central wavelength and a Cold Target Recoil Ion Momentum Spectrometer (COLTRIMS), known as Reaction Microscope (ReMi). It was found that singly excited Rydberg states play a dominant role in the bound ionization process. In order to examine the importance of these Rydberg states for the dissociative ionization, the electron nuclear correlation and electron emission asymmetry was studied experimentally and theoretically. The kinetic energy distribution of the ions is simulated by numerically solving the time-dependent Schrödinger equation, whereas the electron localization asymmetry is modeled with a semiclassical theory. The presented findings indicate that dissociation via the H_2^+ $1s\sigma_g$ state is much less pronounced than commonly believed. Singly-excited Rydberg states are found to play the most important role in multiphoton bound and dissociative ionization of molecular hydrogen with 400 nm photons.

The second part of the thesis reports about a pump-probe measurement using a pulse shaper setup in 4f geometry. To our knowledge this is the first report about combining a pulse shaper with a ReMi. The experimental data is compared to a former pump-probe measurement that uses a Mach-Zehnder interferometer to confirm the correct operation of the pulse shaper.

Zusammenfassung In dieser Arbeit wird die Multiphoton-Ionisation von molekularem Wasserstoff unter Zuhilfenahme von 50 fs kurzen Laserpulsen mit 400 nm Zentralwellenlänge und einem Cold Target Recoil Ion Momentum Spektrometer (COLTRIMS), auch bekannt als Reaktionsmikroskop (ReMi), untersucht. Es zeigt sich, dass einfachangeregte Rydbergzustände eine dominante Rolle in der gebundenen Einfachionisation von H_2 spielen. Um die Bedeutung dieser Rydbergzustände für den Mechanismus der dissoziativen Ionisation zu ergründen, wurde die Elektron-Kern-Korrelation sowie die Emissionsasymmetrie der Elektronen experimentell und theoretisch studiert. Die kinetische Energieverteilung der Ionen wird durch numerisches Lösen der zeitabhängigen Schrödingergleichung simuliert, wohingegen die Emissionsasymmetrie der Elektronen mittels einer semiklassischen Theorie modelliert wird. Die präsentierten Ergebnisse zeigen, dass Dissoziation über den H_2^+ $1s\sigma_g$ Zustand deutlich schwächer ausgeprägt ist als gemeinhin angenommen wird. Vielmehr spielen bei einer Wellenlänge von 400 nm einfach angeregte Rydbergzustände in der gebundenen und dissoziierenden Ionisation von H_2 die bedeutende Rolle.

Der zweite Teil der Arbeit berichtet über eine Pump-Probe Messung unter Benutzung eines Pulsformer-Aufbaus in 4f-Geometrie. Unseres Wissen nach ist dies der erste Bericht über die Kombination eines Pulsformers mit einem ReMi. Die experimentellen Daten im Vergleich zu einer früheren Pump-Probe Messung mittels eines Mach-Zehnder Interferometers bestätigen den korrekten Betrieb des Pulsformers.

Contents

1. Introduction

The invention of the laser in 1960 by Maiman [1] has revolutionized our life in numerous branches such as medicine, science, communication, industry and entertainment electronics. Since then decades were needed to go from the first monochromatic continuous wave to short pulsed lasers. After the discovery of mode-locking in a Ti:Sa laser by Spence *et al.* [2] the basis for nowadays femtosecond pulse generation was founded. A Femtosecond (0.000,000,000,000,001 seconds) is the typical time scale for atoms and molecules to rearrange during chemical reactions. In 1999 Ahmed H. Zewail was awarded the Nobel Prize in Chemistry for establishing and pioneering a new scientific field that is known as *Femtochemistry*. His idea is simple and astonishing at the same time: Two short femtosecond laser pulses are used for interaction with a molecule. The first stronger *pump* pulse triggers an inner dynamics in a molecule for example by exciting it. After a certain time-delay the second weaker *probe* pulse serves as a fast snapshot camera that records the momentary molecular state. This method allows to track the temporal dynamics of chemical reactions in general.

Femtochemistry is not only about understanding underlying mechanisms but also controlling them. Besides the famous pump-probe technique also single-pulse methods can be used for this purpose. Carrier-envelope phase (CEP) stabilized few-cycle pulses [3] and Two-Color Fields [4–8] are nowadays used to control the electron localization during dissociative ionization of diatomic molecules. This is convenient since electron localization can be understood in terms of a fairly simple semi-classical WKB-model by Palacios *et al.* [9] and Fischer *et al.* [10]. This allows for direct comparison between experiment and theory. In the present thesis the analysis of electron localization asymmetry in dissociative ionization will play a major role in understanding which molecular states contribute dominantly.

For the case of bound ionization of molecular hydrogen most theoretical models reduce the problem to the two lowest singly-ionized states, the $1s\sigma_g$ and $2p\sigma_u$ states, because all calculated transition dipole matrix elements to other excited states are far smaller [11]. However, there are a couple of experimental observations indicating, that for multiphoton

ionization also intermediate states are important to model the data. Schellhammer [12] reports clear evidence for the population of singly-excited Rydberg states in multiphoton ionization of H_2 with 400 nm photons. Also Mi *et al.* [7] suspects, that autoionizing Rydberg states contribute with small electron energies up to 0.5 eV. In the course of this thesis new observations will be presented that verify and show, that Rydberg states can not be neglected in multiphoton ionization at 400 nm. In fact, the data indicate that Rydberg states are populated more dominantly than the $1s\sigma_g$ and $2p\sigma_u$ states.

The easiest chemical reactions that can be observed are fragmentation processes of small molecules. H_2^+ as the most fundamental molecule known to mankind has lots of inherent symmetries. This makes it easy to describe the hydrogen molecule with theory models that solve or approximate the quantum mechanical Schrödinger equation in one or another way compared to other molecules. Thus, H_2 is one of only few systems that allow for comparison between experiment and accurate theoretical predictions. For this reason the present thesis concentrates on H_2 exclusively.

An ultrashort laser pulse alone is not sufficient to unravel the molecular dynamics of photoionization processes. In addition information about the particle fragments has to be collected in order to gain an understanding of their movements and states during the course of the reaction. One of the first ion and electron imaging techniques are Product Imaging [13] and its improved version called Velocity Map Imaging [14]. They allow to record momentum distributions of charged particles with the help of a position-sensitive detector, e.g. a phosphor screen. It is possible to retrieve the momentum distribution from the collective detector image that forms, when a huge number of particles impinges on the detector within a certain integration time. However, these methods require the investigated ionization process to be cylindrically symmetric in space. The invention of microchannel plate delay-line detectors and the Reaction Microscope (ReMi) imaging technique allows to detect and reconstruct the complete three-dimensional momentum vectors of ions and electrons after the interaction with a laser pulse in coincidence and independent from the symmetry of the ionization process. This powerful advantage of the ReMi fulfills a fundamental criterion for accurate investigation of chemical reactions - a kinematically complete measurement of all particles.

Although sophisticated techniques like bichromatic pump-probe methods already allow to retrieve and disentangle lots of information from the pump- and probe-steps via background-free detection [15] the most versatile laser instrument in femtochemistry nowadays is the so-called pulse shaper because it allows to modify the polarization and temporal profile of an incoming laser pulse in an arbitrary way. This provides ultimate

control over the laser field. Controlling quantum-dynamical processes with the help of laser light is known as coherent control, which enables the selection of chemical reactions with the help of pump-dump schemes [16, 17] or the Brumer-Shapiro technique via quantum path interference using one- and three-photon absorption processes [18]. One part of the thesis deals with the alignment and test of a Zero-Dispersion Compressor pulse shaper setup in 4f-geometry. It was first experimentally realized in the ultrafast coherent dynamics working group under the supervision of Prof. Dr. Matthias Wollenhaupt from the University of Oldenburg and rebuilt at the Max-Planck-Institut für Kernphysik by Stefanie Kerbstadt [19]. The combination of a pulse-shaper with a ReMi represents the current state-of-the-art device to investigate and control atomic and molecular dynamics because it allows full control over the laser field and to retrieve kinematically complete and coincident three-dimensional momentum distributions of ions and electrons at the same time. To our knowledge this is the first report of combining a pulse shaper with a ReMi.

The thesis is organized as follows: First a theoretical background (chapter 2) about nonlinear optics, ultrashort pulses, spectral pulse shaping and strong-field laser-matter interaction in molecules provides necessary knowledge to understand the following sections. Chapter 3 & 4 give a compact overview over important physical phenomena and technologies concerning ultrashort strong femtosecond laser pulses and their interaction with atoms and molecules. Chapter 5 introduces to the experimental setups and methods. Finally the results are presented and discussed in chapter 6. The reader is encouraged to keep in mind that the thesis consists of two individual experiments: The main part deals with single-pulse measurements at a central wavelength of 400 nm. The final part reports about 800 nm pump-probe test measurements with a pulse-shaper that prove its correct operation.

2. Theoretical Background

2.1. Nonlinear optics

If a medium is placed inside a fast oscillating electric field, the electrons of the atoms and molecules will be affected by this field, whereas the heavy ions remain at their original positions. As a result of the electronic transposition there will be a gradient in the electric charge distribution across the atoms and molecules in the medium, which results in a measurable electrical polarization.

For weak electrical field strengths the polarization vector of an isotropic medium will be proportional to the E-field-vector in first order approximation. But in the general case of nonisotropic media in arbitrary strong electric fields the polarization has to be taylor-expanded. The following description of nonlinear optics is inspired by the book "Nonlinear Optics" by Zheltikov *et al.* [20].

Let us assume an arbitrary electric field and write it as a sum of monochromatic plane waves.

$$\mathbf{E}(t) = \sum_i \mathbf{E}_i(\omega_i) \exp\left(i\mathbf{k}_i\mathbf{r} - \omega_i t\right) + c.c..$$

The electric polarization can be calculated straight forward [20, p. 163] via

$$\begin{aligned}\mathbf{P}(t) = &\int \chi^{(1)}(t-t') \cdot \mathbf{E}(t')dt \\ &+ \iint \chi^{(2)}(t-t_1, t-t_2) \cdot \mathbf{E}(t_1)\mathbf{E}(t_2)dt_1dt_2 \\ &+ \iiint \chi^{(3)}(t-t_1, t-t_2, t-t_3) \cdot \mathbf{E}(t_1)\mathbf{E}(t_2)\mathbf{E}(t_3)dt_1dt_2dt_3 + \dots .\end{aligned}$$

Here $\chi^{(n)}$ describes the susceptibility tensor of rank $n+1$. Performing the Fourier transform on the time-dependent electric polarization and using the Fourier series of the

electric field above yields [20, pp. 163]

$$\begin{aligned}\mathbf{P}(\omega) =& \chi^{(1)}(\omega)\cdot\mathbf{E}(\omega) + \chi^{(2)}(\omega;\omega_i,\omega_j)\cdot\mathbf{E}(\omega_i)\mathbf{E}(\omega_j) \\ &+ \chi^{(3)}(\omega;\omega_i,\omega_j,\omega_k)\cdot\mathbf{E}(\omega_i)\mathbf{E}(\omega_j)\mathbf{E}(\omega_k) + \dots \end{aligned} \tag{2.1}$$

with

$$\begin{aligned}\chi^{(1)}(\omega) &= \int \chi^{(1)}(t)\exp(i\omega t)dt \\ \chi^{(2)}(\omega;\omega_i,\omega_j) &= \chi^{(2)}(\omega=\omega_i+\omega_j) \\ &= \iint \chi^{(2)}(t_1,t_2)\exp\left[i(\omega_i t_1+\omega_j t_2)\right]dt_1dt_2 \\ \chi^{(3)}(\omega;\omega_i,\omega_j,\omega_k) &= \chi^{(3)}(\omega=\omega_i+\omega_j+\omega_k) \\ &= \iiint \chi^{(3)}(t_1,t_2,t_3)\exp\left[i(\omega_i t_1+\omega_j t_2+\omega_k t_3)\right]dt_1dt_2dt_3\,.\end{aligned}$$

The first order in eq. (2.1) describes the well known linear polarization.

2.1.1. Second-order nonlinearity and second-harmonic generation

The second order of the electric polarization (eq. 2.1) describes three-wave mixing phenomena because two incident frequencies ω_1 and ω_2 form an outgoing frequency component $\omega_3 = \omega_1 \pm \omega_2$. This process is known as sum frequency and difference frequency generation. One important application of sum frequency generation called Second Harmonic Generation (SHG) takes place, when two incident photons with same frequencies $\omega_1 = \omega_2$ combine to one photon with twice the initial frequency. When two photons recombine their energies to one photon, its energy has to double due to energy conservation. Also the momentum of the three wave vectors has to be conserved meaning that the wave-vector mismatch $\Delta k = 2k_1 - k_3$ has to vanish for maximum SHG conversion efficiency. The ideal case where $\Delta k = 0$ is called phase matching. Using the dispersion relation $k(\omega) = \omega\frac{n(\omega)}{c}$, where c is the speed of light, the phase-matching condition $\Delta k = 0$ is equivalent to matching the frequency-dependent refractive indices $n(\omega) = n(2\omega)$. In order to achieve phase matching conditions birefringent materials are used. They have two distinct axes, the so-called ordinary and extraordinary axis. While the refractive index along the ordinary axis is essentially independent of the incidence angle between incoming laser beam and the optical axis of the crystal, the refractive index along the extraordinary axis is not (fig. 2.1). There is an incidence angle at which

the refractive index of the SHG frequency equals the refractive index of the fundamental component leading to the desired phase matching condition.

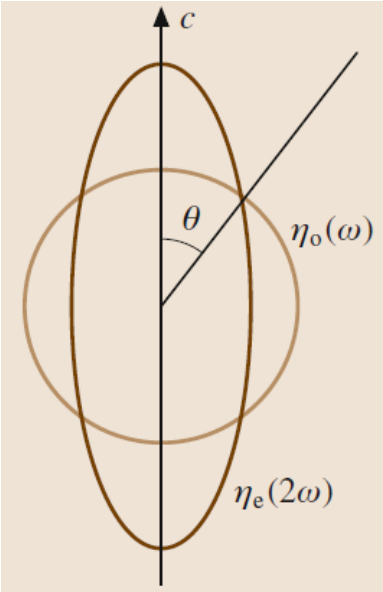

Figure 2.1.: Phase matching in birefringent materials. c is the optical axis of the crystal, θ is the angle between the optical axis and the light propagation direction and $n_0(\omega)$ and $n_e(2\omega)$ describe cross sections trough the refractive index ellipsoids of the ordinary and the extraordinary axes at the fundamental pump and second harmonic frequencies respectively. Figure taken from Zheltikov *et al.* [20, p. 166].

From symmetry considerations it can be shown that even-order susceptibilities have to vanish in centrosymmetric media [21, ch. 1.4.3]. For this reason SHG is only possible in materials without inversion symmetries.

2.1.2. Third-order nonlinearity and optical Kerr effect

In case the second order polarization term in eq. (2.1) is small compared to the first and third order, the refractive index of the medium receives a linear dependence on the laser intensity

$$n = n_0 + n_2 I \tag{2.2}$$

where $n_0 = \sqrt{1 + \chi^{(1)^2}}$ and $n_2 = (2\pi/n_0)^2 \chi^{(3)}(\omega; \omega, \omega, -\omega)$ are the linear and third-order refractive indices. This is called the optical Kerr effect. For a more detailed explanation

on the optical Kerr effect please see *Introduction to Nonlinear Optics,* ch. 5 by New [22] and the chapter "Nonlinear Optics" by Zheltikov *et al.* [20].

The optical Kerr effect is the fundamental principle enabling the pulse compression and pulse amplification techniques called Self-phase modulation and Self-focusing.

Self-Phase modulation

Due to the time dependence of the refractive index (eq. (2.2)) each frequency component aquires a time-dependent phase when travelling a distance L

$$\Phi_\omega(t) = \Phi_\omega(t=0) + \frac{\omega}{c} n_2 I(t) L \,.$$

Here $I(t)$ describes the intensity envelope of the laser pulse. Since frequency is defined as the partial derivative of the phase, each frequency component of the electric field is shifted by $\Delta\omega$, which is proportional to the temporal derivative of the intensity.

$$\Delta\omega = \frac{\omega}{c} n_2 L \frac{\partial I(t)}{\partial t}$$

In case of a typical laser pulse $I(t)$ first rises in time until the pulse reaches its peak intensity, and afterwards it declines again. Therefore the temporal derivative will be positive at the beginning, zero at the peak and negative at the end of the pulse. Consequently the top frequency components of a laser pulse are shifted to higher frequencies, while the tail components are shifted to lower frequencies. Finally the laser pulse is spectrally broadened. This is a prerequisite for ultrashort compressed pulses. If group velocity dispersion is neglected, it can be shown that the pulse envelope shape is preserved when passing the nonlinear medium (see Zheltikov *et al.* [20, p. 169]).

Self-focusing

For simplicity let us assume a gaussian intensity profile $I(r) = I_0 \exp(-r^2/a)$, where I_0 describes the peak intensity on the optical axis of the laser beam, r the radial distance from the optical axis and a the width of the distribution. If this intensity envelope propagates through a Kerr medium, its refractive index will depend on the radial distance from the optical laser axis according to eq. (2.2). Thus the refractive index will be the largest on the optical axis and decreases with increasing r. The central part of the beam will be focused tightest while the pulse's flanks are merely refracted at all. This phenomenon is also known as self-focusing. By using an aperture after the Kerr-medium

a continuous wave (cw) buildup is prohibited, whereas a pulsed mode is enhanced as it is not cut by the aperture (fig. 2.2). If the refraction of the Kerr lens gets too big

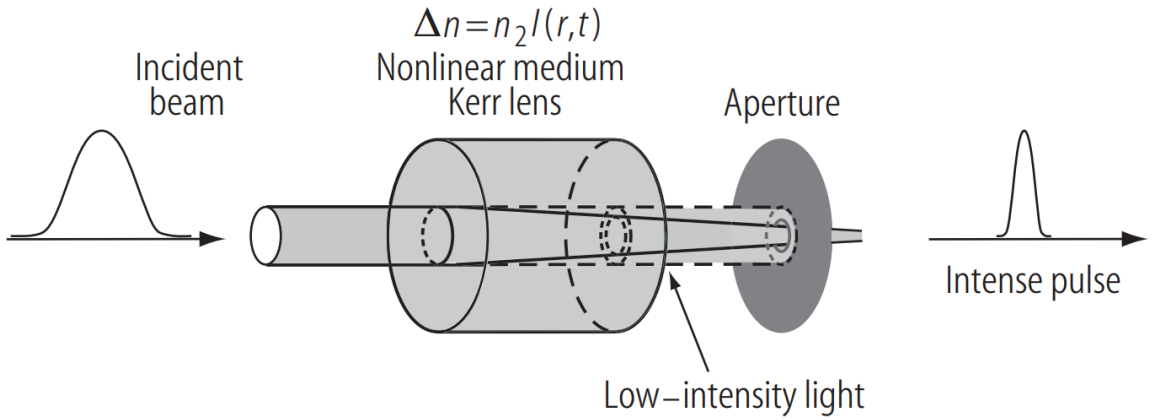

Figure 2.2.: Principle of Kerr-Lens Modelocking with hard aperture [23, p. 91]

the intensity inside the medium exceeds the destruction threshold leading to irreversible damage.

2.2. Ultrashort, intense pulses

It is well known in mathematics that an arbitrary continuous periodic function can be written as an infinite sum of cosine and sine functions, that all have the same zero phase. Each cosine and sine term carries a temporal frequency. The knowledge of these temporal frequencies and their weighting factors allows the reconstruction of the original pulse in time domain. This concept can be generalized to nonperiodic functions, which is known as the continuous Fourier transformation. It allows for two equivalent representations of arbitrary electromagnetic waves in time and frequency domain

$$\mathbf{E}(t,\mathbf{r}) = \frac{1}{(2\pi)^2}\int d\omega \tilde{\mathbf{E}}(\omega,\mathbf{r})\,\mathrm{e}^{i\omega t}$$
$$\tilde{\mathbf{E}}(\omega,\mathbf{r}) = \frac{1}{(2\pi)^2}\int dt \mathbf{E}(t,\mathbf{r})\,\mathrm{e}^{-i\omega t}\ .$$

Let us split the temporal electric field into its real and imaginary part $\mathbf{E}(t,\mathbf{r}) = \mathrm{Re}\,[\mathbf{E}(t,\mathbf{r})] + i\,\mathrm{Im}\,[\mathbf{E}(t,\mathbf{r})]$ and $\mathrm{e}^{-i\omega t} = \cos(\omega t) - i\sin(\omega t)$. Then its Fourier transform

can be rewritten as

$$\tilde{\mathbf{E}}(\omega,\mathbf{r}) \propto \int dt\,\mathrm{Re}\left[\mathbf{E}(t,\mathbf{r})\right]\cos(\omega t) - i\int dt\,\mathrm{Re}\left[\mathbf{E}(t,\mathbf{r})\right]\sin(\omega t) + i\int dt\,\mathrm{Im}\left[\mathbf{E}(t,\mathbf{r})\right]\cos(\omega t) + \int dt\,\mathrm{Im}\left[\mathbf{E}(t,\mathbf{r})\right]\sin(\omega t)\,.$$

For electric fields the imaginary part vanishes and thus the last two integral terms vanish. One can see from the two terms that $\tilde{\mathbf{E}}(-\omega,\mathbf{r}) = \tilde{\mathbf{E}}^*(\omega,\mathbf{r})$. This means that it is sufficient to only know the Fourier transform of the positive frequency components in order to reconstruct the original function.

It is in the nature of the Fourier transform that the original function and its Fourier transform can never be arbitrarily well localized. If the original function has a small width, then its Fourier transform must be broad and vice versa.

Laser pulses are characterized by periodically emerging bursts of electromagnetic radiation that are temporarily well separated from each other. The electric field of pulsed lasers can in general be expressed in terms of the product of a carrier envelope function $f(t)$ and a sinusoidal oscillation with time-dependent phase $\Phi(t)$.

$$\mathbf{E}(t) = \mathbf{E}_0 f(t) cos(\Phi(t))$$

The envelope and phase functions determine the shape of the pulses. Especially the phase $\Phi(t)$ determines the energy of the laser field.

2.2.1. Mode-locking

In a typical laser only those modes survive that generate a standing wave, which is only the case if the cavity length is equal to a multiple of half the wavelength. Since the different modes propagate independently from each other, they do not have an overall fixed phase relation. In case of a high number of modes the average output electric field is essentially constant over time. But if the modes always have the same phase difference to the neighboring frequency mode, then the output electric field is pulsed. Fig. 2.3 shows the effect of the modal phase relation on the temporal shape of the electric field for a superposition of multiple cosine waves. The bigger the overall frequency bandwidth the shorter and more intense the pulses will get according to the Uncertainty Principle of Fourier Transformation. The shortest pulse that can be produced with a given frequency bandwidth is called bandwidth- or fourier-limited.

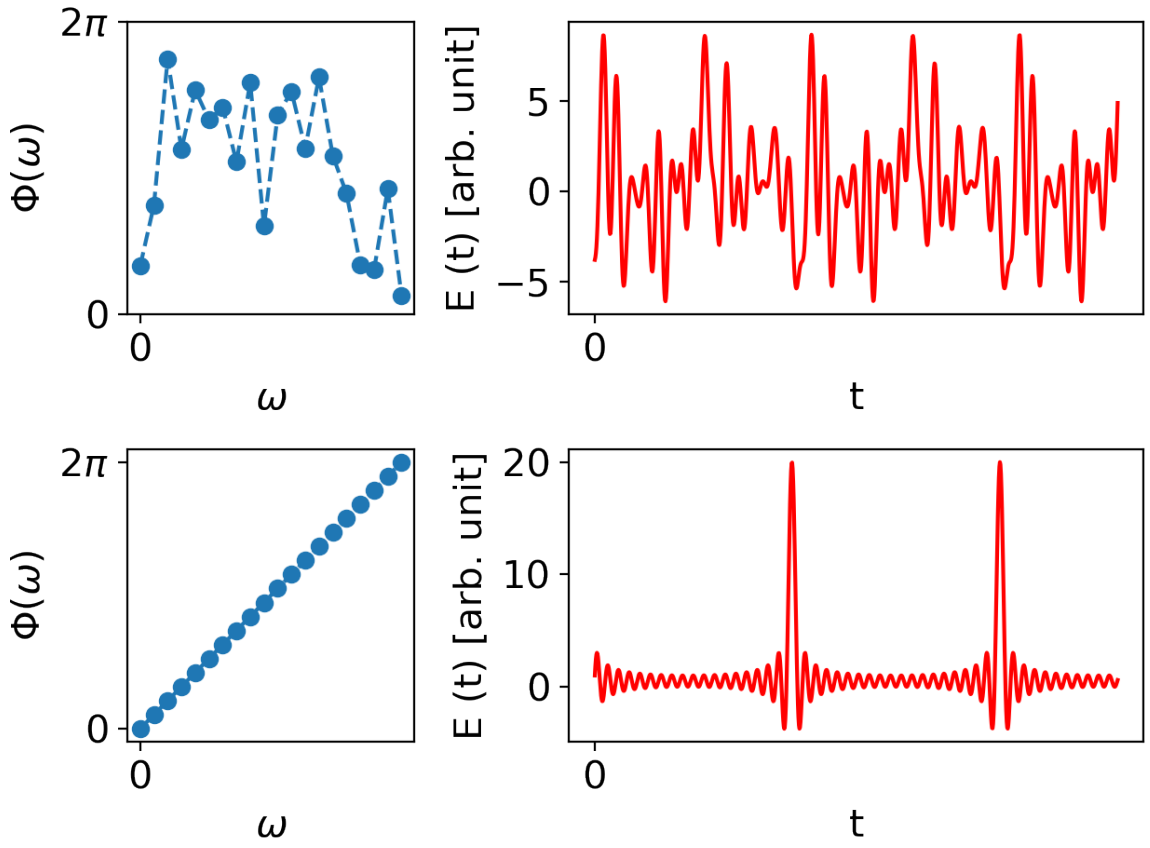

Figure 2.3.: Temporal profile of the electric field E(t) for a superposition of multiple plane waves with constant amplitude at different phase relations $\Phi(\omega)$.

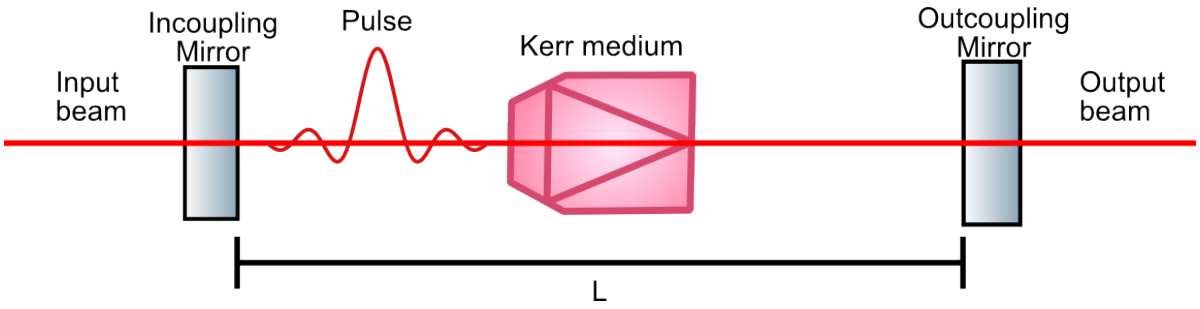

Figure 2.4.: Schematic setup of a cavity with Kerr medium for passive mode locking

In order to switch from cw-mode to mode locking small temporal changes of the field strength are required. These preliminary pulses can then be filtered from the cw components according to the Self-focusing effect like explained in sec. 2.1.2 resulting in a stable pulsed operation mode. Fig. 2.4 shows the schematic setup and working principle of Kerr-lens-mode-locking in the time domain. An incoming laser pulse enters

the cavity where it is amplified according to the Self-focusing effect and part of the pulse is transmitted by the outcoupling mirror. If the cavity length is chosen to properly match the round trip time of the pulse, then multiple pulses from adjacent round trips can coherently add up to form even stronger pulses. The very first preliminary laser pulses are initiated by temporarily kicking the end mirror of the cavity towards the incident laser beam. This stimulates power fluctuations which generates an initial pulse. Thereafter the pulse amplification process runs on its own until the optical losses equal the amplification gain and balance is reached.

2.2.2. Generation and amplification of femtosecond laser pulses

In order to optically amplify laser pulses an active gain medium is pumped by a high power pump laser leading to population inversion. The seed beam, that is to be amplified, stimulates the coherent emission of photons by triggering transitions from excited to relaxed states of the material (fig. 2.5b). Population inversion leads to a transition from the ground to the excited electronic bands. Before the stimulated emission takes place the excited bands relax to the vibronic ground state. Titanium-sapphire (Ti:Sa, Ti:Al_2O_3) is a sapphire (Al_2O_3) crystal, that is doped with titanium-ions (Ti^{3+}), meaning that some Al^{3+}-ions are substituted by Ti^{3+}-ions. Ti:Sa is a very common and favored gain medium because it has a broad absorption bandwidth and the maximum absorption peaks at roughly 500nm, which is ideal for pumping with frequency-doubled Nd:YAG lasers (fig. 2.5a). Also Ti:Sa exhibits a large stimulated emission cross section causing tremendous gain in amplification.

Current mode-locked laser designs do not necessarily use hard apertures to get rid of the cw components like explained in fig. 2.2. The Kerr medium is put into an optical cavity and pumped with an external laser source that is tightly focused into the crystal (fig 2.6). Since only the intense laser pulses have a big overlap with the pump laser profile the pulses are amplified, whereas the collimated cw-mode experiences higher losses.

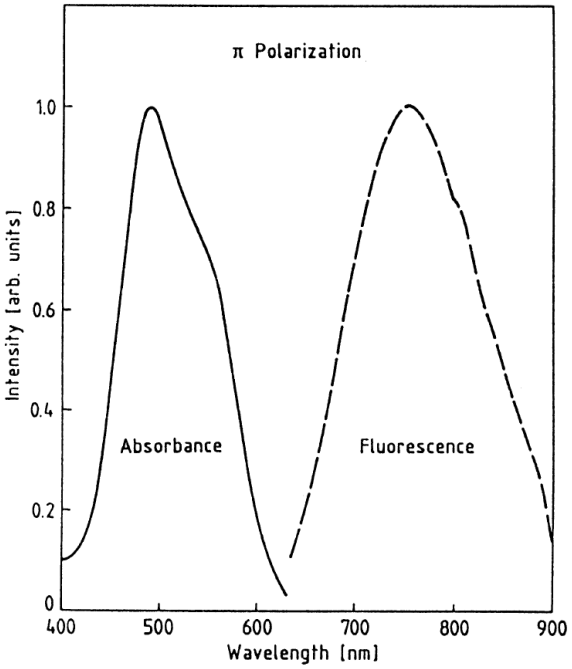

(a) Absorption and fluorescence spectra of Ti:Al_2O_3 for light that is linearly polarized in the plane of incidence

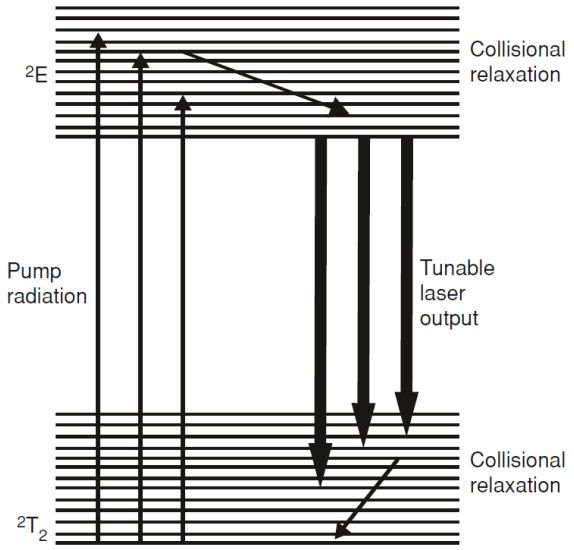

(b) Schematic energy level diagram of Ti:Al_2O_3. $^2T_2$ and ^2E are the ground and excited electronic band structures that get addressed by the 500nm light from the Nd:YAG pump laser.

Figure 2.5.: Figures from Koechner [24, p. 89]

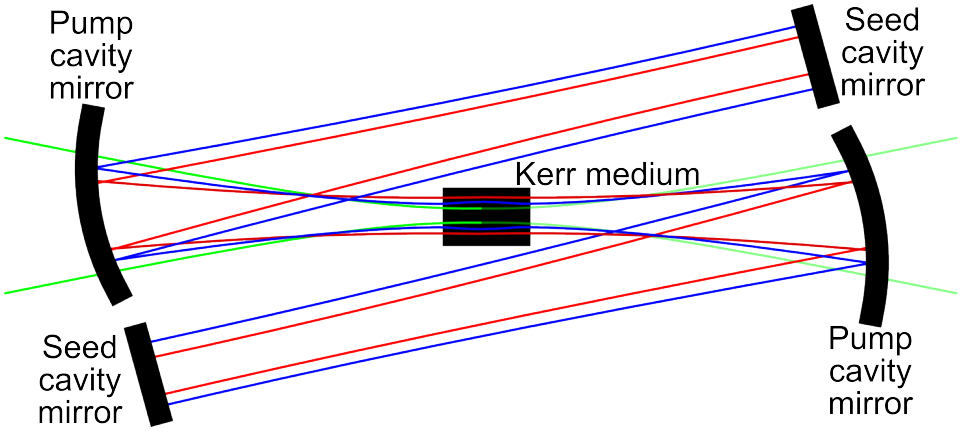

Figure 2.6.: Principle of Kerr-Lens Modelocking without hard aperture in a cavity.[1]Intensity profiles of seed laser pulses (blue), pump laser (green) and cw (red) are shown.

[1]Wikimedia Commons contributors. File:Kerr-lens modelocking.svg. [Online; accessed 18-April-2018], public domain. Wikimedia Commons, the free media repository. 2016. url: https://commons.wikimedia.org/w/index.php?title=File:Kerr-lens_modelocking.svg&oldid=227031907.

2.2.3. Dispersion

In optical physics dispersion in general describes the dependence of the light propagation on one or more wave parameters. One specific and very important kind of dispersion is the chromatic dispersion. It describes the dependence of the phase velocity $v_p = \frac{\omega}{k(\omega)}$ on the frequency ω where k is the wavenumber, or equivalently the frequency dependence of the wavenumber $k(\omega)$. In a general treatment $k(\omega)$ can be taylor-expanded around a central frequency ω_0.

$$k(\omega) = k(\omega_0) + \frac{\partial k(\omega_0)}{\partial \omega}(\omega - \omega_0) + \frac{1}{2}\frac{\partial^2 k(\omega_0)}{\partial \omega^2}(\omega - \omega_0)^2 + \frac{1}{6}\frac{\partial^3 k(\omega_0)}{\partial \omega^3}(\omega - \omega_0)^3 + \dots . \tag{2.3}$$

Since the spatial phase of a monochromatic wave is proportional to the wavenumber the above Taylor-expansion also reflects the spatial phase. The constant and linear terms in eq. (2.3) do not change the temporal shape of the laser pulse. $\frac{\partial k(\omega_0)}{\partial \omega}$ is called the group velocity and describes an overall temporal delay of the pulse. The quadratic and cubic terms $\frac{\partial^2 k}{\partial \omega^2}$ and $\frac{\partial^3 k}{\partial \omega^3}$ are called Group Delay Dispersion (GDD) and Third-order Dispersion (TOD) and lead to the fact that individual frequency components are delayed differently during propagation. For positive GDD k increases with increasing ω which means that the phase velocity $v_p = \frac{\omega}{k}$ gets smaller. Consequently light with higher frequencies gets transported slower than lower frequencies. This is known as normal dispersion. In time-domain this results in an up-chirp, meaning the frequencies at the top of the pulse will be higher than in the tail leading to longer pulse durations. This is an undesired effect in the generation of ultrashort pulses that is present in most transparent media. So the delay between red and blue components have to be reversed in the course of the pulse generation. Therefore materials with negative GDD are used in order to introduce anomalous dispersion analogously leading to a down-chirp or compensation of a previous up-chirp.

In our laser setup there are two types of optical elements that are used to compensate dispersive effects.

Chirped Mirrors consist of multiple dielectric layers alternating in their refractive indices. This kind of system is known as Bragg grating. Reflection of the incident light happens if the Bragg-condition is fulfilled. For a given incidence angle with respect to the surface normal of the mirror Bragg reflection is only possible for a certain wavelength

called the Bragg-wavelength λ_{dB}. If the distance between the layers is changed like shown in fig. 2.7 λ_{dB} changes with the penetration depth allowing red light to penetrate deeper into the material than blue light. Finally the red components will be delayed with respect to the blue components due to longer optical pathways - the laser pulse has acquired an anomalous dispersion. Previous normal dispersion effects can be compensated this way ideally resulting in bandwidth-limited pulses.

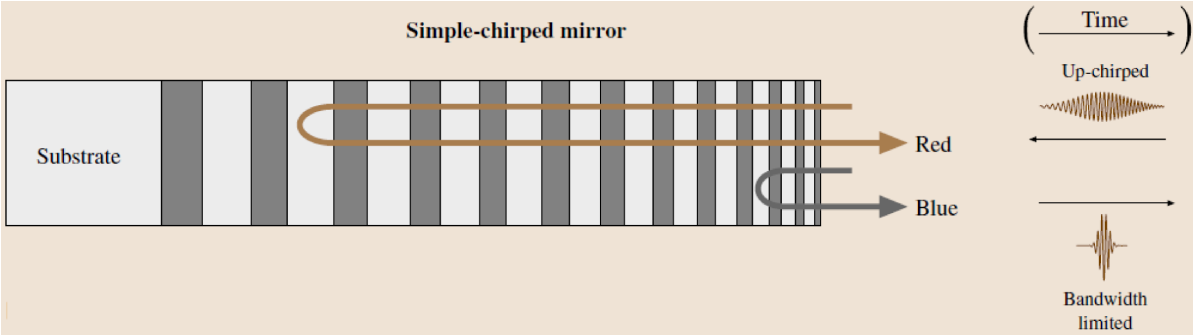

Figure 2.7.: Anomalous dispersion via Chirped Mirrors [25, p. 1063]

Prism Compressors consist of two prisms that disperse incoming light depending on the frequency components. Short wavelengths are refracted stronger than long wavelengths. Although the blue wavelength travels a larger distance in air it is possible to make the red component aquire more temporal phase by choosing a proper geometry due to longer optical pathways inside the prisms (fig. 2.8). The mirror after the second prism reflects the beams exactly backwards and the light travels the same way back. Unfortunately prism compressors tend to introduce higher order normal dispersion. This is why prism compressors are often used together with chirped mirrors.

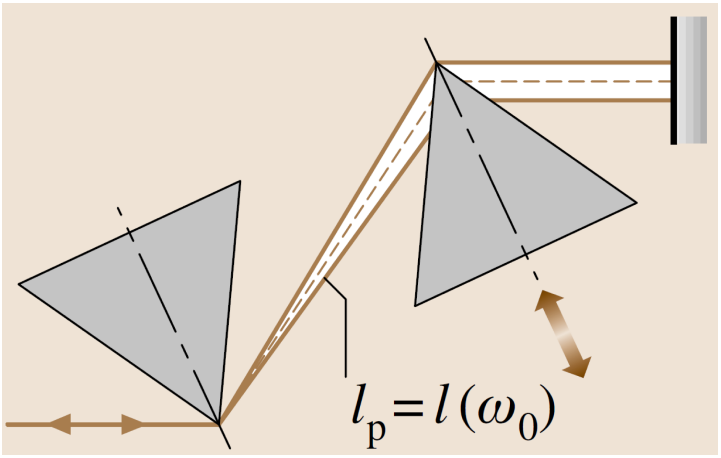

Figure 2.8.: Anomalous dispersion via prism compressor [25, p. 1059]. The optical path length depends on the frequency components and leads to a relative phase shift between the different frequencies of the laser spectrum.

2.3. Spectral pulse shaping

The method of short-pulse-generation, as presented in sec. 2.2, opens up a way to control the pulse duration. Ultimate controllability over laser light however does not just involve the pulse duration but the complete temporal and spatial profile.

The basic idea of spectrally shaping the temporal profile of a pulse is based on the following scheme:

1. Spatial decomposition of the different frequency components inherent in the pulse

2. Application of arbitrary amplitude modulations and phase shifts to each frequency component individually

3. Spatial recombination of all frequency components

Fig. 2.9 outlines the mathematical process of temporal phase shaping. The decomposition of a time-dependent electric field into its frequency components can be achieved in terms of the Fourier transformation. The inverse transformation enables the retrieval of the time-dependent electric field with modified spectral amplitudes and phases.

Mathematically the modified Fourier transform $\tilde{E}_{mod}(\omega, \Phi + \Delta\Phi)$ is generated by multiplying a modulation function of the following form $\tilde{M}(\omega) = |\tilde{M}| \exp^{i\Delta\Phi(\omega)}$ where $\Delta\Phi(\omega)$ is the desired frequency-dependent phase shift that is to be introduced. The original Fourier transform can be written in polar form as $\tilde{E}(\omega, \Phi) = |\tilde{E}(\omega, \Phi)| \, \mathrm{e}^{i\Phi(\omega)}$. Thus, the

$$E(t,\Phi) \xrightarrow{\mathcal{F}} \tilde{E}(\omega,\Phi) \xrightarrow{\cdot\tilde{M}(\omega)} \tilde{E}_{mod}(\omega,\Phi+\Delta\Phi) \xrightarrow{\mathcal{F}^{-1}} E_{mod}(t,\Phi+\Delta\Phi)$$

Figure 2.9.: The fundamental idea of temporal phase shaping. $\mathcal{F}$ and $\mathcal{F}^{-1}$ represent the forward and inverse Fourier transformations. ω and Φ describe the frequency and phase of the electric field components.

phase shifted spectral field reads

$$\tilde{E}_{mod}(\omega,\Phi+\Delta\Phi) = |\tilde{M}|\,\mathrm{e}^{i\Delta\Phi(\omega)}\,|\tilde{E}(\omega,\Phi)|\,\mathrm{e}^{i\Phi(\omega)}$$

Depending on the properties of the modulation function $\tilde{M}(\omega)$ different types of pulse shaping are possible:

Spectral Amplitude Modulation If $|\tilde{M}| < 1$, the weighting factors of the spectral Fourier components $|\tilde{E}_{mod}(\omega,\Phi+\Delta\Phi)|$ and thus also the temporal profile will be changed. The case $|\tilde{M}| > 1$ is not possible with nowadays available pulse shaping techniques since individual frequency components can not be actively amplified but only attenuated.

Spectral Phase Modulation If $|\tilde{M}| = 1$ the frequency spectrum remains unchanged while the spectral phases are modified. So the modified electric field still consists of the same frequency components with the same weighting factors but they are delayed with respect to each other.

Polarisation Shaping If the incident electric field is split into two orthogonal polarization components, that can be shaped individually each with its own modulation function $\tilde{M}_x(\omega), \tilde{M}_y(\omega)$, it is possible to not only change the temporal pulse profile but also the state of polarization, e.g. from linear to circular polarization and vice versa.

2.3.1. Calculating the exiting spectral electric field with Jones formalism

As for all nonlinear optical processes the effect of an optical element on the incident electric field can be represented as a two-dimensional matrix, the so-called Jones matrix.

The two dimensional outgoing electric field vector $\vec{E}_{out}$ results from

$$\vec{E}_{out} = \mathbf{M}\vec{E}_{in} \quad \text{with } \vec{E}_{in} = \begin{pmatrix} E_{in,x} \\ E_{in,y} \end{pmatrix},$$

where $\mathbf{M}$ is the Jones matrix of the respective optical element. The effect of a series of elements is described by the product of the individual Jones matrices. For a phase retardation of $\Delta\Phi$ with the fast axis in x direction the Jones matrix is

$$\mathbf{M}_{\Delta\Phi(\omega)} = \begin{pmatrix} 1 & 0 \\ 0 & \mathrm{e}^{i\Delta\Phi(\omega)} \end{pmatrix}$$

The matrix of a device whose optical axis is rotated by an angle of Θ can be retrieved via $\mathbf{M}_{\Delta\Phi(\omega)}(\Theta) = \mathbf{R}(\theta)\mathbf{M}_{\Delta\Phi(\omega)}\mathbf{R}(-\theta)$ where

$$\mathbf{R}(\Theta) = \begin{pmatrix} cos(\Theta) & sin(\Theta) \\ -sin(\Theta) & cos(\Theta) \end{pmatrix}$$

Let's consider a linearly polarized electric field oriented in x direction. The incoming spectral components can be written as $\vec{\tilde{E}}_{in}(\omega) = \begin{pmatrix} \tilde{E}_{in,x}(\omega) \\ 0 \end{pmatrix}$. Furthermore let's assume that our pulse-shaping device consists of two tunable phase retarders which are orthogonal to each other and turned by an angle of 45° with respect to the incident laser polarization (see fig. 2.10). The full transformation matrix for this case reads

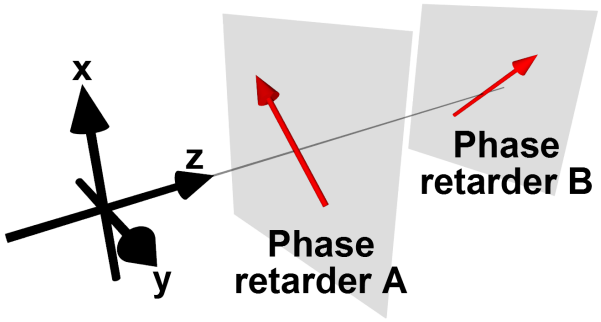

Figure 2.10.: Orientation of incident laser polarization in x direction and the two orthogonal phase retarders (red arrows) ±45° off the x-axis for the presented calculation in Jones-Formalism. The laser propagates along the z-axis.

$$\mathbf{T}_{\Delta\Phi_A(\omega),\Delta\Phi_B(\omega)} = \mathbf{R}\left(\frac{\pi}{4}\right)\mathbf{M}_{\Delta\Phi_B(\omega)}\mathbf{R}\left(-\frac{\pi}{4}\right)\mathbf{R}\left(-\frac{\pi}{4}\right)\mathbf{M}_{\Delta\Phi_A(\omega)}\mathbf{R}\left(\frac{\pi}{4}\right) \tag{2.4}$$

The final field after the phase shaping device can be calculated according to:

$$\begin{aligned}\vec{\tilde{E}}_{out} &= \mathbf{T}_{\Delta\Phi_A(\omega),\Delta\Phi_B(\omega)}\vec{\tilde{E}}_{in}(\omega) \\ &= \exp\left[\mathrm{i}\left(\frac{\Delta\Phi_A(\omega)+\Delta\Phi_B(\omega)}{2}\right)\right]\begin{pmatrix}\cos\left(\dfrac{\Delta\Phi_A(\omega)-\Delta\Phi_B(\omega)}{2}\right)\\ \sin\left(\dfrac{\Delta\Phi_B(\omega)-\Delta\Phi_A(\omega)}{2}\right)\exp\left(\mathrm{i}\dfrac{\pi}{2}\right)\end{pmatrix}\tilde{E}_{in,x}(\omega)\,.\end{aligned} \tag{2.5}$$

For a detailed derivation of 2.5 from (2.4) please see Kerbstadt [19, pp. 127-128].

The setup geometry from fig. 2.10 resembles the actual experimental setup (see sec. 5.2) and therefore eq. (2.5) can be used to theoretically retrieve the modified electric field after the pulse shaper. Moreover it can be used to calculate the necessary phase shifts to accomplish a desired electric field shape.

2.4. Strong field laser-matter interactions

As for all non-relativistic problems in quantum mechanics the dynamics of an atom or molecule, that is ionized by a strong laser field, is governed by the time-dependent Schrödinger equation

$$\mathrm{i}\hbar\frac{\partial}{\partial t}|\,\psi(t)\rangle = \hat{H}|\,\psi(t)\rangle$$

For simplicity let us first consider a single-electron atom with nuclear charge number Z. The Hamilton operator $\hat{H}$ can be written as

$$\hat{H} = \hat{T} + \hat{V}_C + \hat{H}_{\mathrm{int}}\,,$$

where $\hat{T}$, $\hat{V}_C$ and $\hat{H}_{\mathrm{int}}$ describe the kinetic energy operator, the Coulomb potential of the atomic core and the laser-matter interaction operator respectively. By setting the origin of the coordinate system to the position of the proton we get the Hamiltonian of the unperturbed atom $\hat{H}_0$

$$\hat{H}_0 = \hat{T} + \hat{V}_C = -\frac{\hbar^2}{2m_e}\Delta - \frac{Ze}{4\pi\varepsilon_0|\mathbf{r}|}\,.$$

The interaction Hamiltonian $\hat{H}_{\text{int}}$ in the general form is determined by the Hamiltonian of a particle with charge q in an electromagnetic field, which is given by the minimally coupled Hamiltonian $\hat{H}_q = \frac{1}{2m}\left(-i\hbar\nabla - q\mathbf{A}\right)^2 + q\phi$, where $\mathbf{A}$ and ϕ describe the vector and scalar potential of the electric field. By choosing the so-called Coulomb gauge $\nabla \cdot \mathbf{A} = 0$ and $\phi = 0$ the complete Hamiltonian reads

$$\begin{aligned}\hat{H} &= \frac{1}{2m_e}\left(-\mathrm{i}\hbar\nabla + e\mathbf{A}\right)^2 - \frac{Ze}{4\pi\varepsilon_0|\mathbf{r}|} \\ &= -\frac{\hbar^2}{2m_e}\Delta - \frac{\mathrm{i}e\hbar}{m_e}\mathbf{A}\cdot\nabla + \frac{e^2}{2m_e}\mathbf{A}^2 - \frac{Ze}{4\pi\varepsilon_0|\mathbf{r}|}\end{aligned} \tag{2.6}$$

In general the vector potential $\mathbf{A}(\vec{r}, t)$ is position and time dependent and can be expanded in terms of plane waves.

$$\mathbf{A} = \sum_{\mathbf{k}} \varepsilon_{\mathbf{k}} \left[q(t)_{\mathbf{k}} \mathrm{e}^{\mathrm{i}\mathbf{kr}} + q^*(t)_{\mathbf{k}} \mathrm{e}^{-\mathrm{i}\mathbf{kr}}\right]$$

For many applications, such as the atom interaction with visible light, it is justified that the wave vector $k = \frac{\omega}{c}$ is so small, that $\mathbf{kr} \ll 1$ for the region of interest. Subsequently the spatial part of a monochromatic plane wave $\mathrm{e}^{-\mathrm{i}\mathbf{kr}} \approx 1 + \mathbf{k}\cdot\mathbf{r} + \cdots$ can be Taylor-expanded around 0.

Changing the gauge to the so-called length gauge results in an easier but equivalent expression for the complete Hamiltonian [26, p. 80].

$$\hat{H} = \hat{T} + \hat{V}_C + H_{int} = -\frac{\hbar^2}{2m_e}\Delta - \frac{Ze}{4\pi\varepsilon_0|\mathbf{r}|} - e\mathbf{r}\mathbf{E}(t) \tag{2.7}$$

The aforementioned Taylor expansion of the vector potential is called dipole approximation because the interaction Hamiltonian as shown in eq. (2.7) is equivalent to the Hamilton operator of a dipole with constituent charges e in an electric field. Please note that in eqs. (2.6) and (2.7) the electric field is treated purely classically. It does not involve any quantization of the laser field. Thus, the full Hamiltonian is semi-classical.

Despite the dipole approximation eq. (2.6) has no explicit solution in terms of an easily evaluable mathematical expression. Instead, it is necessary to solve the Schrödinger equation with the above Hamiltonian numerically by using proper algorithms and assumptions or to introduce some further approximations that simplify the problem even further.

Relativistic effects start to play a role as soon as the kinetic energy of the electron is of

the same order than the electron's rest mass energy. A reasonable quantity to quantify the kinetic energy of a free electron in a monochromatic laser field with amplitude E_0 is the so-called ponderomotive energy U_p. It describes the cycle-averaged gain in kinetic energy of the electron due to a sinusoidal laser field.

$$U_p = \frac{e^2 E_0^2}{4 m_e \omega^2}$$

So, relativistic effects kick in as soon as

$$\frac{U_p}{m_e c^2} = 1.33 \cdot 10^{-5} \frac{E_0^2}{\omega^2} [\text{in a.u.}] \gtrsim 1$$

In order to quantify the significance of relativistic effects for an electron, that is bound to a Coulomb potential, we can use the virial theorem. In our case the Coulomb potential has the order -1 and thus the virial theorem states that the (time averaged) potential energy of the electron is minus two times the (time averaged) kinetic energy. Since the virial theorem is universal for quantum mechanics as well as classical mechanics, we can therefore substitute the classical energies for the time averaged quantities. In the Bohr atom model, this is equivalent to the equilibrium between Coulomb and centripetal force that is required to keep the electron on the same orbit around the nucleus.

$$\begin{aligned} -E_{pot} &= 2E_{kin} \\ \longrightarrow \frac{Ze}{4\pi\varepsilon r_e^2} &= \frac{m_e v_e^2}{r_e} \end{aligned}$$

By using Bohr's postulate of quantized angular momentum $L = m_e v_e r_e = n\hbar$ for classical, round electron orbits we get a simple expression for the electron's velocity

$$\begin{aligned} v_e &= \frac{Z}{n} [\text{in a.u.}] \\ \longrightarrow \frac{v_e}{c} &= \frac{Z}{n} \alpha [\text{in a.u.}] \end{aligned}$$

where Z,n and $\alpha \approx 0.0073$ describe the nuclear charge, the principal quantum number and the fine-structure constant, respectively. So, in case of atomic hydrogen and the lowest principal quantum number $n = 1$ the ratio is $v_e/c = \alpha \approx 0.73\%$. For this reason relativistic effects are neglected throughout this thesis.

2.4.1. The undisturbed molecule

As for all quantum mechanical problems the stationary Schrödinger equation has to be solved. The Hamiltonian for a molecule with n electrons and N nuclei is

$$\hat{\mathbf{H}}(\{\mathbf{r}\},\{\mathbf{R}\}) = \hat{\mathbf{T}}_{\mathbf{r}}(\{\mathbf{r}\}) + \hat{\mathbf{T}_{\mathbf{R}}}(\{\mathbf{r}\}) + \hat{\mathbf{V}}(\{\mathbf{r}\},\{\mathbf{R}\})\,. \tag{2.8}$$

$\hat{\mathbf{T}}_{\mathbf{r}}$ is the kinetic energies of the electrons, $\hat{\mathbf{T}_{\mathbf{R}}}$ is the kinetic energies of the nuclei and $\hat{\mathbf{V}}$ the potential energies between all charged particles.

Born-Oppenheimer Approximation

Since the general Hamiltonian from eq. (2.8) is too complex to be solved analytically approximations have to be introduced. The Born-Oppenheimer approximation starts with a product ansatz for the total wavefunction that separates the nuclear from the electronic motion

$$\Psi(\{\mathbf{r}\},\{\mathbf{R}\}) = \Phi(\{\mathbf{r}\})\Psi(\{\mathbf{R}\})\,, \tag{2.9}$$

where $\Phi(\{\mathbf{r}\})$ and $\Psi(\{\mathbf{R}\})$ are the decoupled electronic and nuclear wave functions, respectively. Plugging eq. (2.9) into the stationary Schrödinger equation with the Hamiltonian from eq. (2.8) and neglecting spatial derivatives of $\Phi(\{\mathbf{r}\})$ with respect to the internuclear distances $\{\mathbf{R}\}$ (see Hertel & Schulz [27, pp. 139-143] for more details) results in two separate equations for the nuclear and the electronic wavefunctions

$$\begin{aligned}\left(\hat{\mathbf{T}}_{\mathbf{r}}(\{\mathbf{r}\}) + \hat{\mathbf{V}}(\{\mathbf{r}\},\{\mathbf{R}\})\right)\Phi_\gamma(\{\mathbf{r}\};\{\mathbf{R}\}) &= V_\gamma(\{\mathbf{R}\})\Phi_\gamma(\{\mathbf{r}\};\{\mathbf{R}\}) \\ \left(\hat{\mathbf{T}_{\mathbf{R}}}(\{\mathbf{R}\}) + V_\gamma(\{\mathbf{R}\})\right)\Psi_k(\{\mathbf{R}\}) &= E_k\Psi_k(\{\mathbf{R}\})\,.\end{aligned} \tag{2.10}$$

Here, the indices γ, k label the different eigenfunctions for the electronic and nuclear eigenvalue problems from above. The internuclear coordinates are treated like parameters in the electronic motion because compared to the time scale of the electronic motion the nuclei are frozen in space. The variation of the internuclear distance within the electronic motion is neglected in the Born-Oppenheimer approximation. Thus, the electronic eigenvalue problem yields electronic eigenenergies $V_\gamma(\{\mathbf{R}\})$ that depend on the internuclear distances. These functions are called potential energy curves (in case of diatomic molecules) or surfaces (in case of polyatomic molecules) because they describe the effective potential, in which the nuclei move for a given electronic state Φ_γ.

Morse Oscillator model

In order to understand the nuclear motion, it is essential to know the potential energy curve $V_\gamma(\{\mathbf{R}\})$. Fortunately, it is possible to extract this potential from spectroscopic data by using for example the RKR method (Mantz *et al.* [28] and Fleming & Narahari Rao [29]). For a detailed description of the procedure the interested reader is referred to the original papers (Rydberg [30], Klein [31], and Rees [32]). It turns out, that most of the bound potential energy curves of diatomic molecules can be nicely fitted to a function with only three parameters (see e.g. [27, p. 146, fig. 7.3]) that was first introduced by P.M. Morse - the so called Morse potential $V_M(R)$

$$V_M(R) = D_e \left[1 - \mathrm{e}^{-a(R-R_0)}\right] .$$

D_e is the well depth, a describes the well width and R_0 is the equilibrium bond distance. If the Morse Potential form is plugged into the nuclear Schrödinger equation (2.10) and rotations of the molecule are neglected, it can be shown that there are analytical solutions [33]. The vibrational eigenenergies are

$$E_{k,vib} = \left[\left(k+\frac{1}{2}\right) - \frac{1}{2\lambda}\left(k+\frac{1}{2}\right)^2\right]\hbar\omega_0 \quad \text{with} \quad \lambda = \frac{\sqrt{2mD}}{a\hbar} \quad \omega_0 = \sqrt{\frac{2Da^2}{m}}$$

For more information on e.g. the analytical expression for the eigenstate wavefunctions please see Dahl & Springborg [33].

Molecular orbitals and term symbols

The one-electron wavefunction of atoms is well described by a set of four quantum numbers (n, l, m, m_s). According to the Pauli Principle two or more electrons in an atom can never have the same quadruple of quantum numbers. The electronic states of an atom are occupied based on the corresponding state energy starting from lowest to highest values. From the analysis of the hydrogen Schrödinger equation it is clear that the eigenenergies scale with $\frac{Z^2}{n^2}$. Consequently electrons first occupy orbitals with low n. Theory and experimental data on the quantum defect explain well that within a shell with quantum number n the energy levels increase with the angular quantum number l. Hund's second rule explains that within an nl-shell the energy is minimized for maximum total spin S. All these findings found the basis of the famous Aufbau-Principle of the periodic system of elements.

The most straight-forward approach to construct molecular orbitals are linear combinations of atomic orbitals (LCAO). Whereas the Coulomb potential of an atom is spherically symmetric, the potential of a diatomic molecule has cylindrical symmetry. (n, l, m, m_s) is no longer an appropriate set of quantum numbers to describe the single-electron wavefunctions of a molecule. For further explanations for constructing and filling molecular orbitals the interested reader is referred to one of the many textbooks on molecular physics, e.g. "Diatomic Molecules" by Hertel & Schulz.

The general term symbol used for molecular orbitals is ${}^{2S+1}\Lambda_{g,u}$. Here $\Lambda = \Sigma, \Pi, \Delta, \cdots (= 0, 1, 2, \cdots)$ is the projection of the total angular momentum of all electrons and S is the total spin of all electrons. The additional subscript g, u represent the German words *gerade* and *ungerade* and indicate the wavefunction behavior under inversion symmetry, this means how the sign of the wavefunction changes if the spatial vector $\vec{r} \to -\vec{r}$ is reversed. In the case $\Lambda = \Sigma$ all reflection symmetry operations with respect to all possible planes containing the internuclear axis can be either symmetric or antisymmetric, which is indicated as Σ^+ or Σ^-. Fig. 2.1 gives a simple overview over the existing quantum numbers that are important to describe diatomic molecular orbitals.

Kind of angular momentum	Operator	Quantum number	
		Total	projection onto z-axis
Orbital angular momentum	$\widehat{\boldsymbol{L}}$	L	Λ
Electron spin	$\widehat{\boldsymbol{S}}$	S	Σ
Electron total angular momentum	$\widehat{\boldsymbol{J}}_\mathrm{e} = \widehat{\boldsymbol{L}} + \widehat{\boldsymbol{S}}$	J_e	Ω
Nuclear rotation	$\widehat{\boldsymbol{N}}$	N	0
Total angular momentum	$\widehat{\boldsymbol{J}} = \widehat{\boldsymbol{L}} + \widehat{\boldsymbol{S}} + \widehat{\boldsymbol{N}}$	J	Ω
Total without spin	$\widehat{\boldsymbol{K}} = \widehat{\boldsymbol{L}} + \widehat{\boldsymbol{N}}$	K	Λ

Table 2.1.: Quantum numbers of diatomic molecules. Table taken from [34, p. 199]

For homonuclear molecules like H_2^+ the notation of single-electron-orbitals is even simpler. The term symbol reads $nl\lambda_{g,u}^{(*)}$ where n and l describe the main and angular quantum numbers of the united atomic orbitals that are linearly combined. $\lambda = \sigma, \pi, \delta, \cdots (= 0, 1, 2, \cdots)$ is the quantum number associated to the z-component of the total angular momentum operator $\hat{L}_z$ and the asterisk * indicates that the orbital is antibonding. The subscript g, u again indicates the behavior under inversion symmetry.

2.4.2. The disturbed molecule

Introduction to point group theory and molecular selection rules

An easy to understand introduction of point group theory and its application in molecular physics can be found in Engelke [35].

Molecular symmetry is an important tool in physics and chemistry in order to derive chemical properties and spectroscopic transitions of molecules. It allows to derive molecular orbitals and selection rules from first principles.

A geometrical symmetry of a molecule can always be described in terms of a symmetry operation (identity, rotation around an axis, reflection on a plane, inversion on a point, improper rotation). If the symmetry operation yields a transformed molecule, that can not be distinguished from the original one, than the molecule is said to obey the underlying symmetry. Every symmetry operation can be written as a matrix, given a basis set (e.g. vectors or atomic/molecular wavefunctions). The set of all inherent symmetries of a molecule form a so-called point group. The name reveals that for all symmetry operations of the point group there is at least one point that stays fixed in position. The set of matrices representing the symmetry operation is called a possible representation of the point group. There are infinitely many matrix representations to a point group since there are infinitely many basis sets we can choose to setup the matrices. A matrix representation A can be transferred to a block diagonal form via similarity transformations of the form $A' = Q^{-1} \cdot A \cdot Q$, which can not be further simplified. The set of these block diagonal matrices is called an irreducible representation of the point group. There might be several possible irreducible representations of a point group, but since similarity transformations leave the character of a matrix unchanged it is a good quantity to describe the transformation for each symmetry operation of the individual irreducible representations. These character values are given in form of so-called character tables (see fig. 2.2). The first column lists all irreducible representations of the $D_{\infty h}$ point group, which includes all homonuclear molecules like H_2. The solutions of the Schrödinger equation for a given molecular symmetry have to transform like one of the irreducible representations. Therefore the irreducible representations are labeled according to the corresponding molecular states. The first column in fig. 2.2 lists the symmetry operations of the point group. Each following column describes how the respective irreducible representation (first entry of each row) transforms under the symmetry operations of the point group. The last two columns list possible basis functions for the individual irreducible representations, meaning that these functions

$D_{\infty h}$	E	$2C_\infty^\Phi$	...	$\infty\sigma_v$	i	$2S_\infty^\Phi$	...	∞C_2	Possible basis functions	
Σ_g^+	1	1	...	1	1	1	...	1		$x^2 + y^2, z^2$
Σ_g^-	1	1	...	−1	1	1	...	−1	R_z	
Π_g	2	$2\cos\Phi$	...	0	2	$-2\cos\Phi$	...	0	(R_x, R_y)	(xz, yz)
Δ_g	2	$2\cos 2\Phi$	...	0	2	$2\cos\Phi$	...	0		$(x^2 - y^2, xy)$
...	...	...	...	...	...	...	...	...		
Σ_u^+	1	1	...	1	−1	−1	...	−1	z	
Σ_u^-	1	1	...	−1	−1	−1	...	1		
Π_u	2	$2\cos\Phi$	...	0	−2	$2\cos\Phi$	...	0	(x, y)	
Δ_u	2	$2\cos 2\Phi$	...	0	−2	$-2\cos 2\Phi$	...	0		
...	...	...	...	...	...	...	...	...		

Table 2.2.: Character table for the $D_{\infty h}$ point group. E is the identity operation. $2C_\infty^\Phi$ are the rotation operations around the molecular axis. $\infty\sigma_v$ describe the reflections on a plane which contains the molecular axis. i is the inversion operation. $2S_\infty^\Phi$ are the improper rotations around the molecular axis. ∞C_2 is the two-fold rotation around an axis perpendicularly bisecting the molecular axis. The red boxes indicate the rows that are important for the present thesis. Table taken from [36, p. 301]

show the exact same behavior like their associated representations for the complete set of point group operations.

At this point it is necessary to mention an important theorem of point group theory: Every point group owns a fully symmetric irreducible representation meaning, that its character table column consists of ones exclusively. In fig. 2.2 the molecular ground state Σ_g^+ is the fully symmetric irreducible representation of the $D_{\infty h}$ point group.

In order to determine allowed and forbidden spectroscopic transitions the dipole transition matrix element $-E\langle\Psi_f|z|\Psi_i\rangle$ has to be evaluated, where E describes the electric field strength. By taking advantage of the molecular symmetry and point group theory it is possible to find out whether the dipole matrix element vanishes or not without having to calculate the integral explicitly. If we want to evaluate for example the following dipole matrix element $-E\langle\Sigma_g^+|z|\Sigma_u^+\rangle$, we first have to find the irreducible transformations that correspond to each factor. For the molecular states they can directly be found in the character table (fig. 2.2) since the representations are named accordingly. The z-operator transforms like Σ_u^+ as can be seen from the second last column of the table. In a next step the characters of the direct product of representations $\Sigma_g^+ \times \Sigma_u^+ \times \Sigma_u^+$ with respect to the point group's symmetry operations has to be calculated. The character of the direct product of two irreducible presentations can be calculated easily when the

character table is available. It's calculated by multiplying the characters column-wise. Finally we find $\Sigma_g^+ \times \Sigma_u^+ \times \Sigma_u^+ = \Sigma_g^+$ which is the fully symmetric irreducible representation of the point group $D_{\infty h}$ (see tab. 2.3). This is equivalent of stating that the dipole matrix element does not vanish. We can repeat this method to find that $-E\langle\Sigma_g^+|z|\Sigma_g^+\rangle = 0$ because the direct product of the corresponding irreducible representations is not fully symmetric.

$D_{\infty h}$	E	$2C_\infty^\Phi$	$\infty\sigma_v$	i	$2S_\infty^\Phi$	∞C_2
Σ_g^+	1	1	1	1	1	1
Σ_u^+	1	1	1	-1	-1	-1
$\Sigma_u^+ \times \Sigma_u^+ \times \Sigma_g^+$	1^3	1^3	1^3	$(-1)^2 \times 1$	$(-1)^2 \times 1$	$(-1)^2 \times 1$
$= \Sigma_g^+$	1	1	1	1	1	1
$\Sigma_g^+ \times \Sigma_u^+ \times \Sigma_g^+$	1^3	1^3	1^3	-1×1^2	-1×1^2	-1×1^2
$= \Sigma_u^+$	1	1	1	-1	-1	-1

Table 2.3.: Character table for direct products of irreducible representations of the $D_{\infty h}$ group.

Dipole Selection Rules in diatomic molecules

Rotations and Vibrations The transition probability between two different single-electron molecular wavefunctions is given by the absolute value squared of the following dipole matrix element [27, pp. 167]

$$D_{fi} = \int \Psi_f^*(\mathbf{r},\mathbf{R}) D \Psi_i(\mathbf{r},\mathbf{R}) \mathrm{d}^3\mathbf{R}\mathrm{d}^3\mathbf{r} \quad \text{with } D = e\left(\tilde{Z}\mathbf{R} - \sum_i \mathbf{r}_i\right)\mathbf{e}_{rad}$$
$$\text{and } \tilde{Z} = \frac{Z_A R_A + Z_B R_B}{R_A + R_B},$$

where $\mathbf{e}_{rad}$ is the unit vector in direction of the radiation polarization. The nuclear wavefunction is separated in a radial and angular component like the following

$$\Psi_{\gamma\nu N}(\mathbf{R}) = \frac{\Re_{\gamma\nu N}(R)}{R} Y_{NM_N}(\Theta,\Phi)\,.$$

ν and N, N_M are the vibrational and rotational quantum numbers. The above separated Ansatz yields for the dipole transition matrix element

$$D_{fi} = \int \frac{\Re^*_{\gamma'\nu'N'}(R)}{R} Y^*_{N'M'_N}(\Theta,\Phi)\Phi^*_{\gamma'}(\mathbf{r};\mathbf{R}) D \\ \frac{\Re_{\gamma\nu N}(R)}{R} Y_{NM_N}(\Theta,\Phi)\Phi_{\gamma}(\mathbf{r};\mathbf{R})\mathrm{d}^3\mathbf{R}\mathrm{d}^3\mathbf{r}\,. \tag{2.11}$$

Here the quantum numbers $(\gamma'\nu'N'M'_N)$ and $(\gamma\nu NM_N)$ belong to the final and initial states, respectively.

A straight-forward calculation shows that if only the rotational quantum number N is allowed to change, only those transitions that fulfill $\Delta N = \pm 1$ and $\Delta M_N = 0, \pm 1$ will result in a non-vanishing dipole transition matrix element. It must be noticed at this point that purely rotational transitions can only be observed for molecules with a permanent dipole moment.

Vibrational transition in the dipole approximation can only exist if also the rotational quantum number changes. That's why these nuclear transitions are often also called rovibrational transitions. Treating the molecular potential curve as harmonic oscillator leads to vibrationally allowed transitions with $\Delta\nu = \pm 1$. By including anharmonicity also $\Delta\nu = \pm 2, \pm 3, \cdots$ transitions can take place.

Electron transitions and Franck-Condon Principle For simplicity we only consider a change in electronic and vibrational quantum numbers $\gamma\nu \to \gamma'\nu'$. In eq. (2.11) the integral over the first dipole term $\tilde{Z}e\mathbf{R}$ in $\mathrm{d}^3\mathbf{r}$ yields 0 because the electronic initial and final wavefunctions are orthogonal. The remaining integral over the second dipole term $\sum_i \mathbf{r}_i$ reads:

$$D_{fi} = \int \Re^*_{\gamma'\nu'N'}(R) D_{\gamma\to\gamma'} \Re_{\gamma\nu N}(R)\mathrm{dR}$$
$$\text{with} \quad D_{\gamma\to\gamma'} = e\mathbf{e}_{rad} \int \sum_i \Phi^*_{\gamma'}(\mathbf{r};\mathbf{R})\mathbf{r}_i\Phi_{\gamma}(\mathbf{r};\mathbf{R})\mathrm{d}\mathbf{r}^3$$

$D_{\gamma\to\gamma'}$ obviously depends on R. But according to the Born-Oppenheimer approximation it is merely a parameter for the electronic wavefunction. The so-called Condon approximation [37, 34, p. 306] uses the fact that the electronic part of the dipole moment $D_{\gamma\to\gamma'}$ in general varies only slowly with the internuclear distance R. Therefore the total dipole

moment is approximated in first order as

$$D_{fi} = \langle D_{\gamma\to\gamma'}\rangle \int \Re^*_{\gamma'\nu'N'}(R)\Re_{\gamma\nu N}(R)\mathrm{dR}\,,$$

where $\langle D_{\gamma\to\gamma'}\rangle$ describes the electronic part of the dipole moment that is averaged over the internuclear distance. The absolute value squared of the integral $\|\langle\langle\int \Re^*_{\gamma'\nu'N'}(R)\Re_{\gamma\nu N}(R)\mathrm{dR}\|^2$ is called Franck-Condon factor and quantifies the overlap of the initial and final nuclear wavefunctions. Since an electronic transition in molecules happens so fast, the nuclear motion can not adapt quickly enough. Thus, the electronic transition can only happen if the initial nuclear motion allows it. If either of the electronic or nuclear dipole moment contributions becomes zero, a dipole transition is impossible. Fig. 2.11 shows the Franck-Condon factors for the transition from the vibrational ground state of the electronic H_2 ground state to the different vibrational states of the $H_2^+1s\sigma_g$ curve.

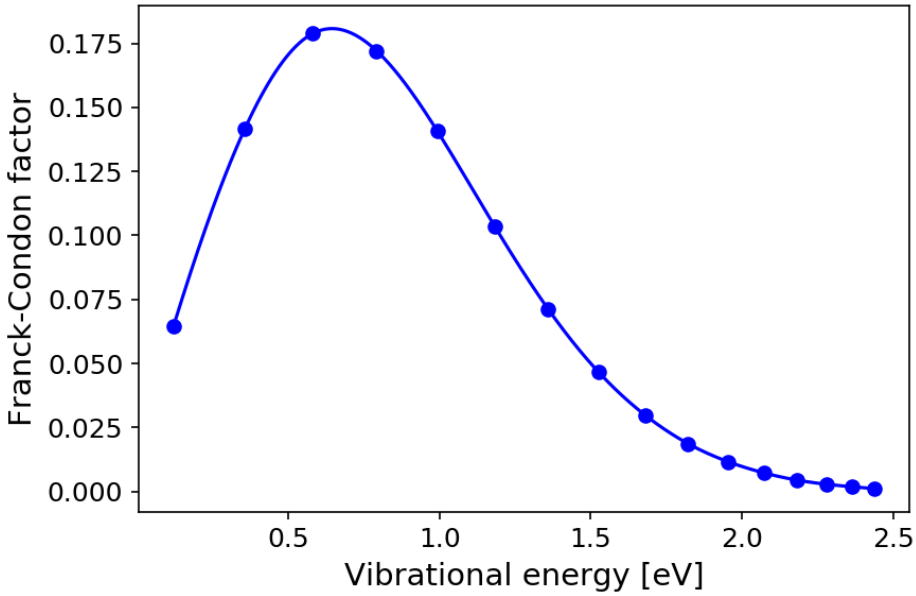

Figure 2.11.: Franck-Condon factors for the transition from the vibrational ground state of the electronic H_2 ground state to the different vibrational states of the $H_2^+1s\sigma_g$ curve as calculated by Wacks [38].

Like in the atomic case, it is possible to derive general dipole selection rules for diatomic molecules [34, pp. 309-310]. These are:

1. For the total angular momentum J: $\Delta J = 0, \pm 1$ and $\Delta M_J = 0, \pm 1$ but not $J = 0 \leftrightarrow J = 0$

2. For the total electron spin S: $\Delta S = 0$

Beyond these there are additional selection rules that depend on the coupling strengths between electronic orbital momentum, electronic spin momentum and nuclear angular momentum. The so-called Hund cases distinguish the different possible coupling strength cases. The interested reader is referred to "Diatomic Molecules", sec. 3.6.4 by Hertel & Schulz.

Nuclear dynamics of H_2^+ in a laser field with arbitrary time-dependence

Calculating the eigenstate of the H_2^+ molecule in an arbitrary electric field is only possible by numerical means. As already mentioned on page 20, eq. (2.7) describes the Hamiltonian operator of an electron in a Coulomb potential $\hat{V}_C$. For the H_2^+ molecule we get:

$$\hat{H} = -\frac{\hbar^2}{2m_e}\Delta - \frac{1}{4\pi\varepsilon_0}\left(\frac{1}{|\mathbf{r}+\mathbf{R}/2|} + \frac{1}{|\mathbf{r}-\mathbf{R}/2|}\right) - e\mathbf{r}\mathbf{E}(t)$$

where $\mathbf{R}$ describes the internuclear distance.

Using the Born-Oppenheimer approximation we arrived at two separated Schrödinger equations for the electronic and nuclear motion of the undisturbed molecule, respectively (see (2.10)). Solving the electronic part is still difficult because it involves the Coulomb potential with its well-known singularity and in addition the internuclear distance serves as an additional parameter that is to be included in the simulation as well. However, the nuclear dynamics is rather easy to simulate because there is an easy analytical model, the Morse oscillator, which can be used (see 2.4.1).

In order to theoretically describe the nuclear dynamics in the Born-Oppenheimer approximation, we have to solve the time-dependent nuclear Schrödinger equation. But since there is an interaction between the different nuclear states due to the laser field, that is mediated via the electrons, eq. (2.10) has to be modified to

$$\left(\hat{\mathbf{T}}_{\mathbf{R}}(\{\mathbf{R}\}) + V_\gamma(\{\mathbf{R}\}) + H_{\text{int}}\right)\Psi_k(\{\mathbf{R}\}) = \mathrm{i}\hbar\frac{\partial}{\partial t}\Psi_k(\{\mathbf{R}\})\,, \tag{2.12}$$

where H_{int} describes the dipole interaction between different electronic states. Let us

rewrite this in form of a matrix representation.

$$\mathrm{i}\hbar\frac{\partial}{\partial t}\begin{pmatrix}\Psi_1(\mathbf{R},t)\\ \Psi_2(\mathbf{R},t)\\ \vdots\\ \Psi_n(\mathbf{R},t)\end{pmatrix} = \begin{pmatrix}-\frac{p^2}{2\mu}+V_1(\mathbf{R},t) & D_{12} & \cdots & D_{1n}\\ D_{21} & -\frac{p^2}{2\mu}+V_2(\mathbf{R},t) & \cdots & D_{2n}\\ \vdots & \vdots & \ddots & \vdots\\ D_{n1} & D_{n2} & \cdots & -\frac{p^2}{2\mu}+V_n(\mathbf{R},t)\end{pmatrix}\begin{pmatrix}\Psi_1(\mathbf{R},t)\\ \Psi_2(\mathbf{R},t)\\ \vdots\\ \Psi_n(\mathbf{R},t)\end{pmatrix} \tag{2.13}$$

The off-diagonal elements are the dipole moments D_{ij} between the different electronic states Φ_i, Φ_j and describe their coupling to each other due to the interaction with the electric field.

$$D_{ij} = -e\,\langle\Phi_i\,|\,rE(t)\,|\,\Phi_j\rangle = -eE(t)\int_{-\infty}^{\infty}\Phi_i^*(r)r\Phi_j(r)\mathrm{d}r$$

Eq. (2.13) can be simulated to a comparatively high degree of accuracy by using a Split-Step-Algorithm, which is explained in more detail in the methodology sec. 5.4.

Light Dressed States in Floquet picture

Since laser light can be described in terms of waves, it is periodic in time. Thus, also the Hamiltonian of an atom or molecule in an external laser field is periodic. At any time t the Hamiltonian is the same as after the laser time period T: $H(t) = H(t+T)$. According to Floquet theory the following wavefunctions are solutions to the Schrödinger equation for a periodic Hamiltonian [26, pp. 45-48]

$$\Psi_\alpha(x,t) = \mathrm{e}^{-\mathrm{i}\,\epsilon_\alpha t/\hbar}\,\Phi_\alpha(x,t)\,,$$

$\Psi_\alpha(x,t)$ are called Floquet states. $\Phi_\alpha(x,t)$ is a periodic function with period T. Plugging this into the time-dependent Schrödinger equation and performing the time derivative yields the following Eigenvalue-Problem:

$$\mathcal{H}(t)\Phi_\alpha(x,t) = \epsilon_\alpha\Phi_\alpha(x,t) \tag{2.14}$$

where $\mathcal{H}(t) = H(t) - \mathrm{i}\,\hbar\partial_t$. Eq. (2.14) has the same structure as the stationary Schrödinger equation. ϵ_α and $\Phi_\alpha(x,t)$ are called quasi-energies and quasi-eigenfunctions.

$\{\Psi_\alpha(x,t)\}$ forms a complete set of basis states in the underlying Floquet space. Thus every wavefunction $\Psi(x,t)$ of the Floquet space can be written as a superposition of Floquet states:

$$\Psi(x,t) = \sum_\alpha c_\alpha \Psi_\alpha(x,t)$$

Due to the fact that $\Psi_\alpha(x,t)$ always has a strict temporal period of $T = \frac{2\pi}{\omega}$, the following quasifunctions $\Psi_\alpha(x,t)\,\mathrm{e}^{\mathrm{i}\,k\omega t}$ and quasienergies $\epsilon_\alpha + k\hbar\omega$ with $k = \pm 1, \pm 2, \cdots$ are equivalent to $\Psi_\alpha(x,t)\,\mathrm{e}^{\mathrm{i}\,\omega t}$ and $\epsilon_\alpha + \hbar\omega$.

Floquet Matrix Since $\Phi_\alpha(x,t)$ is periodic, we can extend it in terms of a Fourier series. In Bra-Ket-notation we get:

$$|\Phi_\alpha\rangle = \sum_{n=-\infty}^{\infty} |\Phi_\alpha^n\rangle\,\mathrm{e}^{-\mathrm{i}\,n\omega t}$$

If there is an orthonormal basis $\{|k\rangle\}$, such that $|\Phi_\alpha^n\rangle = \sum_{k=0}^{\infty} \Phi_{k,\alpha}^n\,|k\rangle$, then the Floquet-type Schrödinger equation (2.14) yields:

$$\sum_{n=-\infty}^{\infty}\sum_{k=0}^{\infty} \mathcal{H}\Phi_{k,\alpha}^n\,|k\rangle\,\mathrm{e}^{-\mathrm{i}\,n\omega t} = \sum_{n=-\infty}^{\infty}\sum_{k=0}^{\infty} \epsilon_\alpha \Phi_{k,\alpha}^n\,|k\rangle\,\mathrm{e}^{-\mathrm{i}\,n\omega t} \tag{2.15}$$

For better legibility we introduce the notation $|kn\rangle := |k\rangle\,\mathrm{e}^{-\mathrm{i}\,n\omega t}$. Multiplying eq. (2.15) with $\langle lm|$ from the left and integrating over one period of the laser field leads to

$$\sum_{n=-\infty}^{\infty}\sum_{k=0}^{\infty} \langle\langle lm\,|\,\mathcal{H}\,|\,kn\rangle\rangle \Phi_{k,\alpha}^n = \epsilon_\alpha \Phi_{l,\alpha}^m$$

where $\langle\langle\cdots\rangle\rangle = \frac{1}{T}\int_0^T \langle\cdots\rangle\,dt$. Using our notation $|kn\rangle := |k\rangle\,\mathrm{e}^{-\mathrm{i}\,n\omega t}$ from earlier, substituting $\mathcal{H}(t) = H(t) - \mathrm{i}\,\hbar\partial_t$ and performing the time derivative on the exponential factor results in:

$$\langle\langle lm\,|\,\mathcal{H}\,|\,kn\rangle\rangle = \left\langle l\,\middle|\,H^{[m-n]}\,\middle|\,k\right\rangle - n\hbar\omega\delta_{mn}\delta_{lk} \tag{2.16}$$

with $H^{[m-n]} = \frac{1}{T}\int_0^T dt H(t)\,\mathrm{e}^{i(m-n)\omega t}$. Eq. (2.16) tells us how to calculate the socalled Floquet-matrix of the eigenvalue problem from eq. (2.14). Let's consider a sinusoidal perturbation with $H(t) = H_0 + H_1 \sin\omega t$. H_0 is the Hamiltonian of the unperturbed

system and H_1 is the amplitude of the perturbation. The final Floquet matrix looks like this:

$$\begin{pmatrix}
\ddots & & & & & \\
& \boldsymbol{H_0} - 2\hbar\omega\mathbf{1} & \frac{1}{2\,\mathrm{i}}\boldsymbol{H_1} & \mathbf{0} & \mathbf{0} & \\
& -\frac{1}{2\,\mathrm{i}}\boldsymbol{H_1} & \boldsymbol{H_0} - 1\hbar\omega\mathbf{1} & \frac{1}{2\,\mathrm{i}}\boldsymbol{H_1} & \mathbf{0} & \\
& \mathbf{0} & -\frac{1}{2\,\mathrm{i}}\boldsymbol{H_1} & \boldsymbol{H_0} & \frac{1}{2\,\mathrm{i}}\boldsymbol{H_1} & \\
& \mathbf{0} & \mathbf{0} & -\frac{1}{2\,\mathrm{i}}\boldsymbol{H_1} & \boldsymbol{H_0} + 1\hbar\omega\mathbf{1} & \frac{1}{2\,\mathrm{i}}\boldsymbol{H_1} \\
& \mathbf{0} & \mathbf{0} & \mathbf{0} & -\frac{1}{2\,\mathrm{i}}\boldsymbol{H_1} & \boldsymbol{H_0} + 2\hbar\omega\mathbf{1} \\
& & & & & \ddots
\end{pmatrix}$$

Here $\mathbf{0}, \mathbf{1}, \boldsymbol{H_0}, \boldsymbol{H_1}$ are all block matrices of same size. For computational reasons their sizes as well as the number of Fourier terms $\pm 1\hbar\omega, \pm 2\hbar\omega, \cdots$ have to be truncated to a finite number.

The above derivation of the Floquet matrix is based on a purely classical treatment of the electric field. Shirley [39] discusses the relation to the quantized field theory. It can be shown that the signed integer $n = -\infty, \cdots, \infty$ can be interpreted as number of absorbed or emitted photons. So the quasi-energies and -eigenstates resemble the solution to the fully coupled system of atom/molecule plus laser field and describe the quantum states of this system depending on the number of absorbed/emitted photons.

Semiclassical WKB Approximation

The WKB approximation is named after Gregor Wentzel, Hendrik Anthony Kramers and Léon Brillouin who published it independently from each other and almost simulatenously in 1926 [40–42]. To arrive at this approximation let us consider the one-dimensional stationary Schrödinger equation in the position basis

$$-\frac{\hbar^2}{2m}\frac{d^2}{dx^2}\psi(x) + V(x)\psi(x) = E\psi(x)\,. \tag{2.17}$$

If the potential $V(x)$ is constant, the plane wave $A\,\mathrm{e}^{\pm ip_0/\hbar x}$ is a well-known solution. Therefore, it is intuitive to make the Ansatz $A\,\mathrm{e}^{\pm i/\hbar S(x)}$ for a slowly varying potential

$V(x)$. Inserting this Ansatz into (2.17) yields

$$-\frac{i\hbar}{2m}\frac{d^2S(x)}{dx^2}+\frac{1}{2m}\left[\frac{dS(x)}{dx}\right]^2+V(x)-E=0\,.$$

In a next step $S(x)$ is expanded in a power series of $\hbar$

$$S(x)=\sum_{i=0}^{\infty}\hbar^i S_i(x)\,.$$

Subsequently the Schrödinger equation now reads

$$-\frac{i\hbar}{2m}\sum_{i=0}^{\infty}\hbar^i\frac{d^2S_i(x)}{dx^2}+\frac{1}{2m}\left[\sum_{i=0}^{\infty}\hbar^i\frac{dS_i(x)}{dx}\right]^2+V(x)-E=0\,.$$

We can sort all the terms according to the order of $\hbar$. In the classical limit $\hbar\to 0$ all higher order terms besides $\hbar^0$ vanish and we get

$$\frac{1}{2m}\left[\frac{dS_0(x)}{dx}\right]^2+V(x)-E=0\,,$$

which has the following solution

$$S_0(x)=\pm\int_{x_0}^{x}\sqrt{2m(E-V(x'))}dx'\,.$$

Consequently the approximated solution to the stationary Schrödinger equation (2.17) is given by

$$\psi(x)=B\exp\left(\pm\frac{i}{\hbar}\int_{x_0}^{x}\sqrt{2m(E-V(x'))}dx'\right)\,,$$

where B describes the normalization factor. This explanation is a short but comprehensive derivation of the WKB approximation in one dimension. For a more detailed treatment please see Nolting [43, sec. 7.4].

Electron emission asymmetry in Dissociation

Since dissociation releases a proton, a neutral hydrogen atom and a free electron, the latter has three options during its emission: It can propagate in direction of the proton ($\alpha<90°$), of the neutral hydrogen atom ($\alpha>90°$) or perpendicular ($\alpha=90°$) to the

molecular axis. Whether the freed electron favors a certain direction during the bond

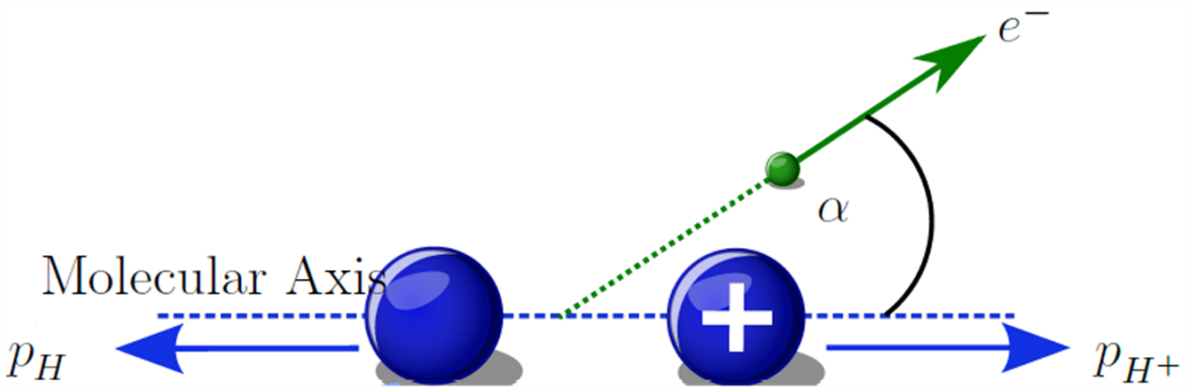

Figure 2.12.: Electron Localization Asymmetry in dissociation of H_2. Please note that this drawing describes the situation in the molecular center of mass frame. Figure taken and adapted from [44, p. 59]

breaking can be quantified via the so-called electron emission asymmetry parameter A. If the dissociation process is repeated $N = N_{\alpha<90^\circ} + N_{\alpha>90^\circ} + N_{\alpha=90^\circ}$ times, then the asymmetry parameter is defined as

$$A = \frac{N_{\alpha>90^\circ} - N_{\alpha<90^\circ}}{N_{\alpha>90^\circ} + N_{\alpha<90^\circ}} \,. \tag{2.18}$$

In the following the physical origin of the asymmetry will be explained synoptically. I will follow the explanation by Fischer [44, sec. 4.3.2 and 4.3.3]. For a detailed description please also see Palacios *et al.* [9] who first published the general theoretical framework.

When molecular hydrogen gets dissociated via multiple photons of equal energy there are several possible dissociation pathways as indicated in fig. 2.13. Here we restrict ourselves to two pathways - the direct and one-photon-dissociation. The final wavefunction of the dissociated molecule can thus be written as a linear combination of the Σ_g and Σ_u states times the wavefunction of the freed electron that is emitted in the course of the two different pathways. In order to get the correct electron wavefunction we take advantage of point group theory (see sec. 2.4.2). For each absorbed photon the parity of the emitted electron changes from gerade to ungerade and vice versa. Absorption of an odd photon number to go from the H_2 ground state to the H_2^+ $1s\sigma_g$ state would yield an ungerade electron wavefunction, whereas an even photon number absorption would yield a gerade electron wavefunction. This follows from the strict application of the dipole selection rule $\Delta l = \pm 1$ and starting with an $l = 0$ electron in the H_2 ground state. For simplicity we restrict ourselves to the lowest possible orbital momenta such

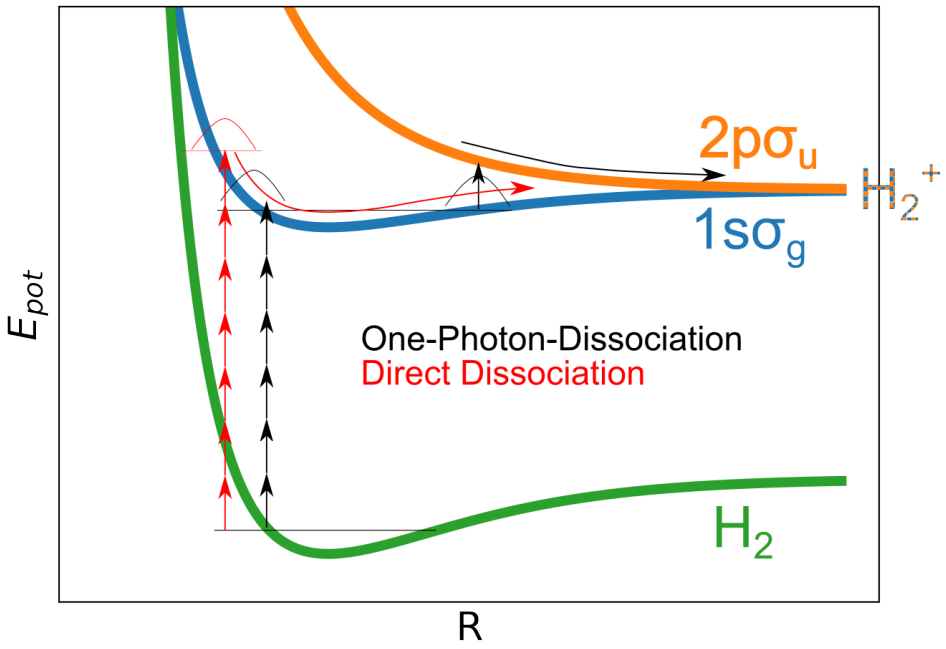

Figure 2.13.: Ionization pathways drawn in the potential curves of H_2. The process starts at the vibrational ground state of the ground electronic state (green). Then the molecule can either (i) absorb 7 photons and be transfered to the H_2^+ electronic ground state $1s\sigma_g$ (blue) from which it classically rolls down the potential towards infinite internuclear distance R$\rightarrow\infty$ where the molecule finally dissociates (red pathway) or (ii) first absorb 6 photons to the H_2^+ electronic ground state $1s\sigma_g$ and after some time absorb another photon to the first excited unbound $2p\sigma_u$ state where it classically rolls down the potential hill and dissociates towards R$\rightarrow\infty$ (black pathway).

that for each absorbed photon the wavefunction of the freed electron changes from σ_g to σ_u and vice versa. Since in the direct dissociation there is always one photon absorbed additionally, the parity of the emitted electron for the different pathways always has to be opposite. The final wavefunction can thus be written as:

$$|\Psi_f\rangle = c_1 |\Sigma_u\rangle |\sigma_g\rangle + c_2 |\Sigma_g\rangle |\sigma_u\rangle \quad \text{or} \quad |\Psi_f\rangle = c_1 |\Sigma_u\rangle |\sigma_u\rangle + c_2 |\Sigma_g\rangle |\sigma_g\rangle \tag{2.19}$$

The answer to the question which of the above wavefunction has to be chosen depends on the number of absorbed photons.

The next step is to retrieve a theoretical expression for the asymmetry parameter as defined in eq. (2.18). Let $P_{\alpha>90°}$ and $P_{\alpha<90°}$ be the operators that lead to an electron emission away from and towards the proton direction during dissociation, respectively.

So the asymmetry parameter can also be written as

$$A = \frac{\langle \Psi_f | P_{\alpha<90^\circ} | \Psi_f \rangle - \langle \Psi_f | P_{\alpha>90^\circ} | \Psi_f \rangle}{\langle \Psi_f | P_{\alpha<90^\circ} | \Psi_f \rangle + \langle \Psi_f | P_{\alpha>90^\circ} | \Psi_f \rangle} \tag{2.20}$$

$$P_{\alpha<90^\circ} = |n_{\rightrightarrows}\rangle \langle n_{\rightrightarrows}| + |n_{\leftleftarrows}\rangle \langle n_{\leftleftarrows}|$$
$$P_{\alpha>90^\circ} = |n_{\rightleftarrows}\rangle \langle n_{\rightleftarrows}| + |n_{\leftrightarrows}\rangle \langle n_{\leftrightarrows}|$$

$$|n_{\rightrightarrows}\rangle = |p_{\rightarrow}\rangle |e_{\rightarrow}\rangle, \quad |n_{\leftleftarrows}\rangle = |p_{\leftarrow}\rangle |e_{\leftarrow}\rangle$$
$$|n_{\rightleftarrows}\rangle = |p_{\rightarrow}\rangle |e_{\leftarrow}\rangle, \quad |n_{\leftrightarrows}\rangle = |p_{\leftarrow}\rangle |e_{\rightarrow}\rangle$$

n is the number of events and the upper arrow indicates the propagation direction of the proton whereas the lower arrow shows the direction of the freed electron. In order to evaluate the asymmetry parameter from eq. (2.20) it is necessary to change the basis set from $|p_{\rightarrow}\rangle, |p_{\leftarrow}\rangle, |e_{\rightarrow}\rangle, |e_{\leftarrow}\rangle$ to Σ_g, Σ_u and σ_g, σ_g (see fig. 2.14). Using all of the above

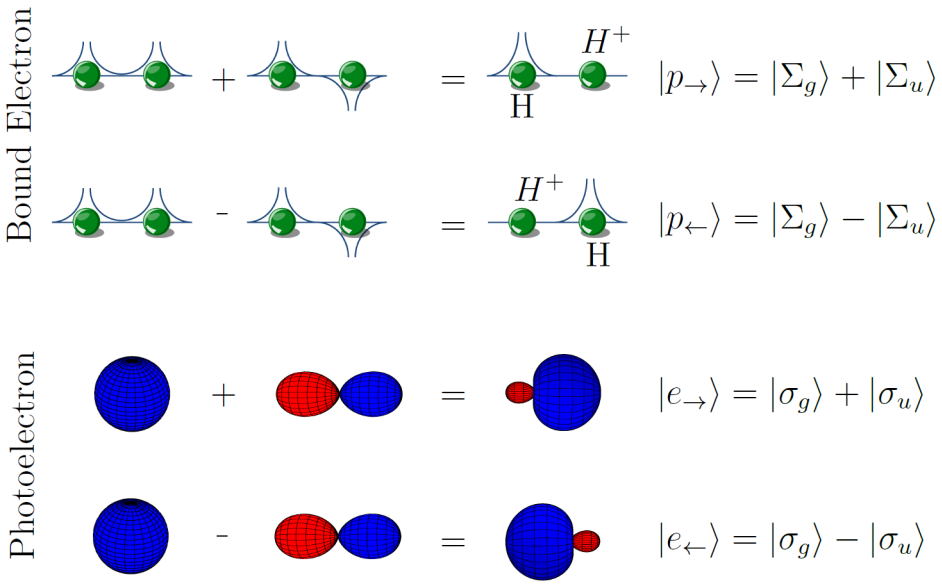

Figure 2.14.: Basis set of localized bound-electron and photoelectron states. The top two rows visualize the bound electron wavefunction of the dissociated H_2^+ while the lower two rows show the situation for the emitted free electron. For both electrons the electron can either locate/fly to the left or the right. The right side of this illustration describes how the localized wavefunctions can be rewritten as linear combinations of the wavefunctions Σ_g, Σ_u and σ_g, σ_g. Figure taken from [44, p. 65]

equations and exploiting the orthogonality relations $\langle \Sigma_i \,|\, \Sigma_j \rangle = \langle \sigma_i \,|\, \sigma_j \rangle = \delta_i j$ simplifies eq. (2.20) tremendously (see sec. A.2 for the derivation):

$$A = -\frac{2\mathrm{Re}[c_1 c_2^*]}{|c_1|^2 + |c_2|^2} \tag{2.21}$$

No matter what final wavefunction from eq. (2.19) is chosen, the result from eq. (2.21) will stay invariant.

Without loss of generality we rewrite the complex amplitudes c_1, c_2 from eq. (2.19) in polar form

$$c_{1,2} = r_{1,2} e^{i(\varphi_{1,2} + \xi_{1,2})} \tag{2.22}$$

Here φ and ξ describe the nuclear and electronic phases. The latter is considered constant, whereas the nuclear phase is calculated according to the WKB approximation

$$\varphi_{1,2} = \int_{R_0}^{R} \sqrt{2m(E - V_{1,2}(R'))} dR' \tag{2.23}$$

Inserting eqs. (2.22) and (2.23) into eq. (3.1) leads to

$$A = \cos(\underbrace{(\varphi_1 - \varphi_2)}_{\Delta\varphi} + \underbrace{(\xi_1 - \xi_2)}_{\Delta\xi})$$

Whereas $\Delta\varphi$ is numerically calculated, $\Delta\xi$ is determined from the comparison with experimental data.Due to the parity of the cosine function the sign of $\Delta\varphi$ does not matter for the correct simulation of the asymmetry as long as the constant offset $\Delta\xi$ is adequately adapted.

Fischer *et al.* [10] measured and analyzed the energy-dependent electron emission asymmetry caused by the interference of the H_2^+ ground and H_2 doubly excited Q_1-states in the dissociation process and found excellent qualitative agreement between experimental data and a successful semiclassical simulation like described above.

3. Photoionization of atoms

Since the invention of sub-picosecond laser pulses 40 years ago, numerous interesting effects were discovered, such as Tunneling ionization, Above-Threshold-Ionization (ATI) and High-Harmonic Generation. The following section aims at giving a compact overview of important physical phenomena and technologies concerning ultrashort strong femtosecond laser pulses.

3.1. Tunneling ionization

Let us imagine a one-electron atom in the electric field of a laser pulse. The total potential, in which the electron is moving, is given by the superposition of the nuclear Coulomb potential and the dipole laser-matter interaction potential due to the laser pulse. Please note that the dipole treatment is only valid if the central wavelength is much bigger than the size of the atom. At the time of maximal amplitude the electric field strength is E. Thus the total potential for a hydrogen atom is

$$V_{\text{tot}} = V_{\text{C}} + V_{\text{int}} = -\frac{1}{4\pi_0}\frac{1}{x} - E \cdot x \,.$$

As soon as V_{int} and V_{C} are comparable in magnitude the total potential will be distorted significantly. The inclination is maximum at maximum electric field strength. At these moments a potential hill of finite height and width is created for the bound electron (fig. 3.1). Although the electron does not have enough energy to classically overcome this barrier for E=0.5 au, according to the rules of quantum mechanics there is a non-zero probability for the electron to tunnel and leave the atom. For strong electric fields (E=1 au) the potential barrier will be lower than the binding energy of the electron allowing for ionization. This process is called over-the-barrier-ionization and is classically allowed.

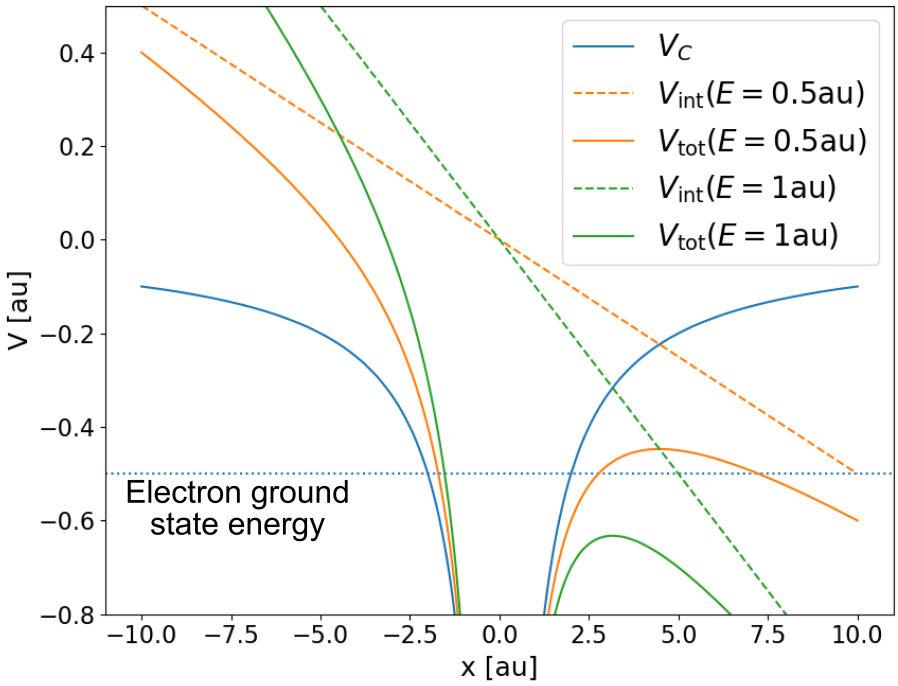

Figure 3.1.: Tunneling ionization through an inclined Coulomb potential for different electric field strengths. x and V describe the radial position and the potential energy of an electron in a hydrogen atom which is centered at x=0. See text for more explanation.

3.2. High harmonic generation

If a nonlinear medium gets irradiated by a strong femtosecond laser pulse, new laser frequencies equal to multiples of the original central frequency can be generated.

In the last decades High Harmonic Generation (HHG) was intensively studied in noble gases. Fig. 3.2 shows the typical structure of noble gas photoelectron energy spectra by Paulus *et al.* [45]. There is a region at intermediate harmonic orders for which the HHG efficiency is roughly constant and then followed by a sudden cutoff. Krause *et al.* [46] first empirically realized, that the cutoff occurs at I_P+3U_P, where I_P is the ionization potential of the atom and U_P the ponderomotive energy of the electron in the laser field. The theoretical model that can describe HHG in monoatomic media is called Three-Step- or Simple-Man's-Model and was mainly invented by Corkum et al. [47, 48]. Fig. 3.3 explains the idea of this model. A slowly varying strong laser field distorts the Coulomb potential of a quantum mechanically treated atom such, that there is a finite probability of tunneling in direction of lower potential energy or ionizing over the barrier. After the

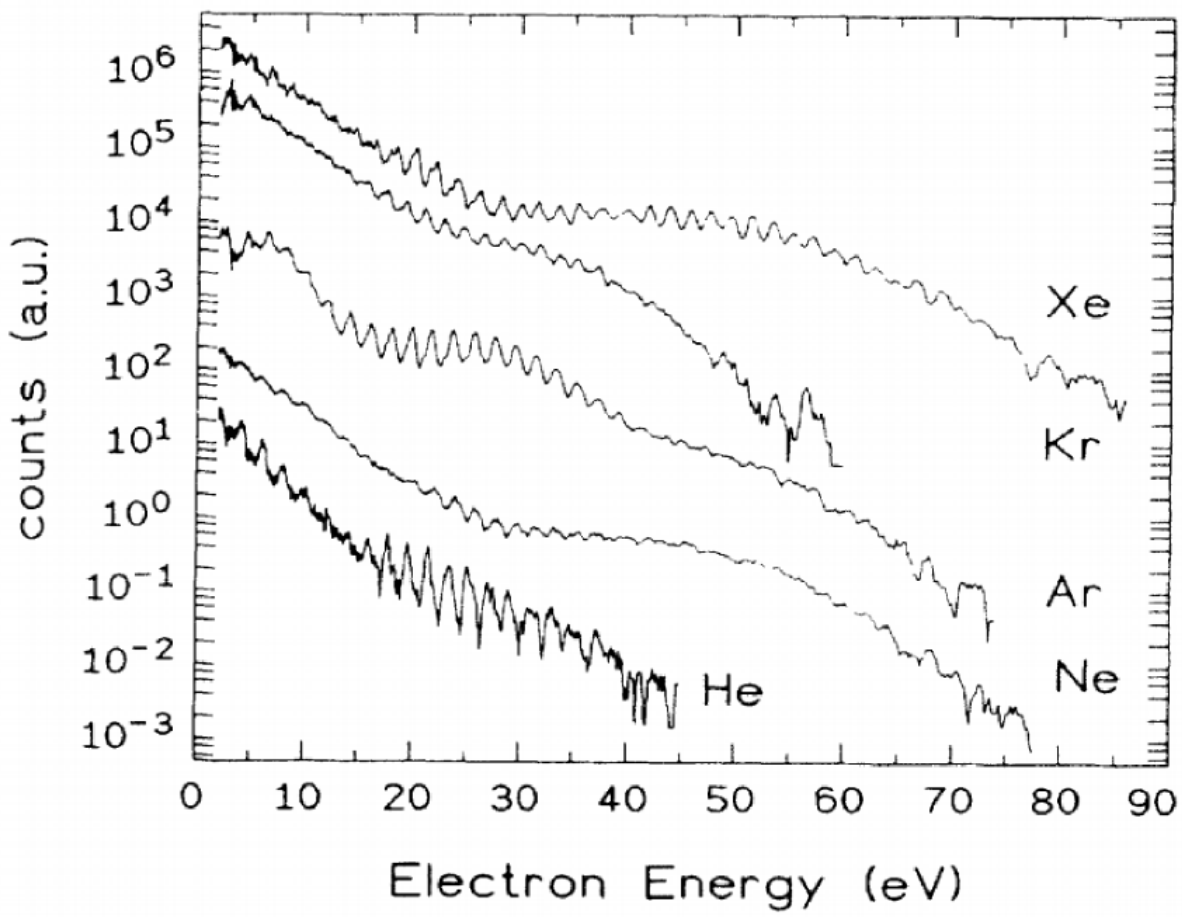

Figure 3.2.: Photoelectron energy spectra of noble gases. Experiments, results and figures by Paulus *et al.* [45]

electron has left the parent core, the Coulomb potential is neglected in comparison to the strong electric field, that is oscillating in time. After half a laser cycle the potential is bent along the opposite direction making the freed electron travel back to its parent ion. The movement of the free electron in the laser field is treated classically. At the location of the parent ion the electron recombines again leading to emission of radiation. The correct calculation yields a maximum radiation energy of $\sim 3.2U_P$ and is in excellent agreement with the empirical finding by Krause *et al.* [46]. The spectrum of the emitted XUV radiation is a frequency comb that peaks at multiples of the fundamental frequency. In case of monoatomic gases only odd multiples are accessible due to symmetry reasons. Nowadays attosecond pulses are generated by modelocking multiple adjacent higher harmonics. Thus, HHG is a key technology in the development of ultrashort laser pulses. In addition, HHG is able to extend the range of available laser wavelengths towards several tens of eV. However, Higher Harmonic conversion efficiencies are still in general

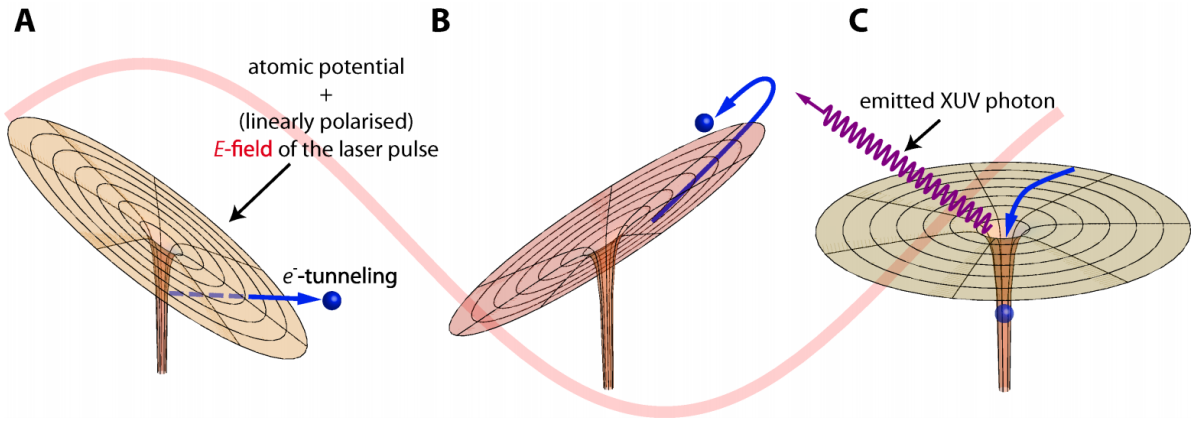

Figure 3.3.: Three-Step-Model. Figure taken from [49]

very low compared to other attosecond generation techniques. Brabec & Krausz [50] report about maximum harmonic conversion efficiencies of $\sim 10^{-6}$ in Argon. This can be a disadvantage for experiments that rely on sufficiently strong light intensities.

3.3. Multiphoton ionization

The term "multiphoton ionization" in principle means, that ionization can happen via absorption of multiple photons. For example in the case of atomic argon in its ground state an energy of 15.7 eV is required to remove the most weakly bound electron. If the pulsed laser field has a central wavelength of 400 nm, the mean photon energy is roughly 3.1 eV. So in order to ionize Argon at least 5 photons are required.

Which kind of ionization process - Tunneling or Multiphoton Ionization - takes place is most often characterized by the ratio of the time that would be required for tunneling ionization τ_T and half a period of the laser field $\tau_L/2$ [51]. This ratio γ is called Keldysh parameter and is calculated via

$$\gamma = \frac{\tau_T}{\tau_L/2} = \sqrt{\frac{I_P}{2U_P}} \quad \text{with} \quad U_P = \frac{e^2 E_0^2}{4 m_e \omega^2}\,.$$

I_P and U_P denote the ionization potential and the ponderomotive potential of an electron in a monochromatic laser field with angular frequency ω. U_P is the mean kinetic energy, that a free electron aquires during one laser cycle. For $\gamma < 1$ the electron has enough time to tunnel through the barrier and thus this domain is called the tunneling regime. Vice versa $\gamma > 1$ indicates, that the laser oscillates too fast for tunneling and thus this domain is called multiphoton regime. However, the concept of the Keldysh parameter

is sometimes misleading and inconsistent as discussed by Reiss, ch. 2.6. It should never be seen as a safe indicator for tunneling or multiphoton ionization. Instead it is better to consult laser frequency, laser intensity and ionization potential individually.

A theoretical treatment of multiphoton transition from bound to free continuum states in the framework of perturbation theory yields, that the leading-order contribution to ionization with n photons is proportional to the nth power of the incident intensity [53, p. 50]. In order to absorb several photons at a time, higher laser intensities are requires compared to single-photon transitions. This perturbative approach breaks down as soon as strong electric fields lead to a strong coupling between the atom/molecule and the laser field, which is known as the AC-Stark shift. In this case the atomic/molecular states can no longer be considered as unperturbed [54, p. 397].

Resonance-enhanced multiphoton ionzation

Resonance-enhanced multiphoton ionzation (REMPI) is a two-step process. First, n photons are simultaneously absorbed from the atom/molecule, which then undergoes a resonant transition to an excited, bound intermediate state without ionizing. Due to the resonance, the transition rate of this first step is usually significantly higher then the non-resonant case. During the lifetime of the intermediate state another m photons are absorbed simultaneously leading to a transition to free continuum states - the target atom/molecule is finally ionized. In order to achieve same ionization rates an (n+m)-REMPI process requires smaller laser intensities than a single multiphoton transition with n+m photons, since the transition probability decreases with increasing number of photons for a given laser intensity.

3.4. Above threshold ionization

Fig. 3.4 shows the photoelectron energy spectrum of xenon atoms, that are multiphoton-ionized in a laser field. All peaks are spaced equally with the photon energy. A bound electron, that is ionized in a strong field, can absorb more than the minimum required number of photons, that is necessary for ionization to the continuum. The excess energy above the ionization potential is given to the free electron in form of kinetic energy. Since the photon energy is quantized, the electron energy spectrum must also show this quantization. The energy balance reads

$$E_e = (n+s)\hbar\omega - I_P\,. \tag{3.1}$$

Here, n describes the minimum photon number required for ionization, s is the number of excess photons and I_P is the ionization potential. Let us consider weakly bound Rydberg states. If the laser electric field strength is strong enough, low bound Rydberg states will be affected by the laser. Since the Rydberg electrons are loosely bound to the nuclei, they can be considered free to some extent and will start to quiver in the laser field. This quivering motion takes energy from the laser field - on average this is given by the ponderomotive potential U_P. Consequently for ionization from a Rydberg state to take place, it is not enough to absorb an energy equal to I_P but $I_P + U_P$. One could say, that the ionization potential has shifted to higher values and thus eq. (3.1) modifies to

$$E_e = (n + s)\hbar\omega - (I_P + U_P)\,.$$

The width of the individual ATI peaks is mainly determined by the bandwith of the laser pulses and the ponderomotive energy of the electrons.

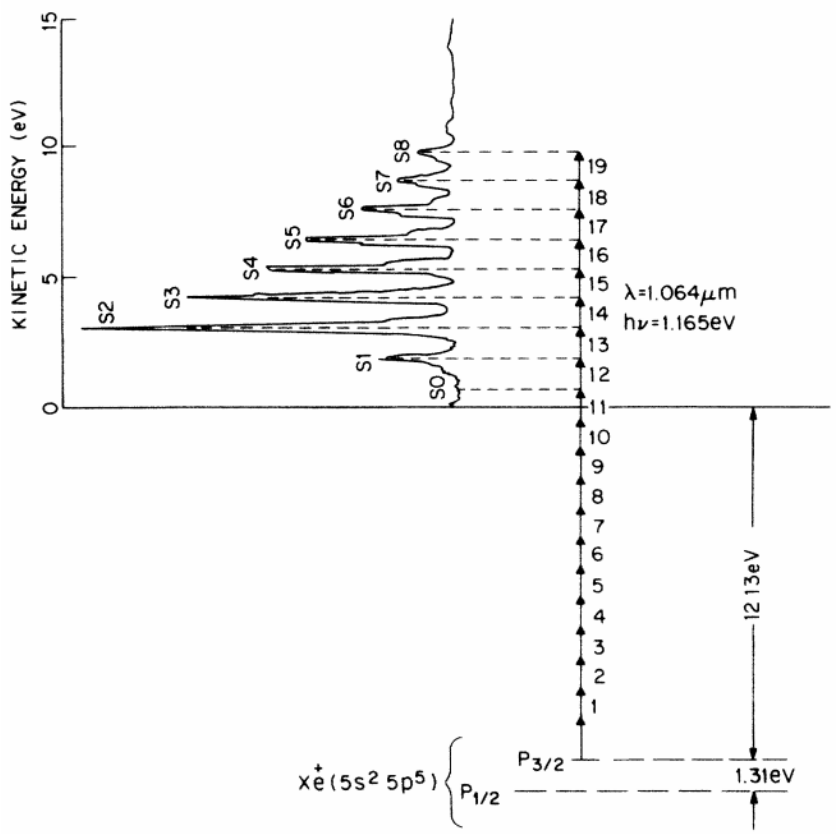

Figure 3.4.: Above-Threshold-Ionization from the $P_{3/2}$ state in Xenon with 100 ps pulses and 1064 nm wavelength. The electron kinetic energy spectrum is shown. The energy level diagram below visualizes the corresponding transitions. Experiment, results and figure by Freeman *et al.* [55]

3.5. Photoelectron angular distributions

The wavefunction of a photoelectron, that scatters from an ion, can be written as a superposition of spherical harmonics

$$\psi_e = \sum_{lm} c_{clm} e^{i\delta_l} Y_{lm}(\theta, \phi)\,,$$

where δ_l is a scattering-induced phase shift, l is the angular quantum number and m is the projection quantum number. This is known as the partial wave expansion in scattering theory. The quantity, that is usually measured in experiments, is the absolute

value squared of this wavefunction which takes the form [56, pp. 400-401]

$$I(\theta,\phi) \propto |\psi_e|^2 = \sum_{lm}\sum_{l'm'} c^*_{l'm'} c_{lm} e^{i(\delta_l - \delta_{l'})} Y^*_{l'm'}(\theta,\phi) Y_{lm}(\theta,\phi)$$
$$= \sum_{LM} B_{LM} Y_{LM}(\theta,\phi) \tag{3.2}$$

with $|l-l'| \leq L \leq l+l'$ and $M = m+m'$. θ is the angle between the laboratory frame axis and the photoelectron emission direction. The photoelectron angular distribution (PAD) from a one-photon ionization of an isotropic gas target is

$$I(\theta) \propto 1 + B_2 P_2(cos\theta)\,,$$

where P_l describes the l-th order Legendre polynomial [57]. B_2, often also written as β, is the so-called anisotropy parameter and holds phase information about the photon process.

According to Dill [58] eq. (3.2) is also applicable to the case of diatomic molecules, that are fixed in the laboratory frame. In this case (θ,ϕ) are the angles between the electron emission direction and the molecular axis. For reasons of symmetry L must always be even and only L-orders up to $2l_{max}$ contribute. l_{max} describes the highest orbital angular momentum of the partial waves. In case of linearly polarized laser pulses dipole selection rules demand $\Delta m = 0$. If initially the electron is in a ground state with $l = m = 0$, then only $m = 0$ terms are allowed in eq. (3.2). Since $Y_{l0}(\theta,\phi) \propto P_l(cos(\theta))$, the spherical harmonics can be reduced to Legendre polynomials. In addition the dipole selection rule $\Delta l = \pm 1$ prohibits contributions from partial waves with $l > l_{max} = N$, where N describes the number of absorbed photons. The resulting angular distribution reads

$$I(\theta) \propto \sum_{0}^{2N} B_l P_l(cos(\theta))\,.$$

4. Photoionization of molecules

The following chapter gives an overview of the current research status of photoionization of small molecules based on the example of H_2.

4.1. Two-step mechanism

When talking about the bound and dissociative ionization dynamics of molecular hydrogen, most theoretical concepts reduce the problem to the two lowest, singly-ionized states $1s\sigma_g$ and $2p\sigma_u$. In most cases this simplification is justified because all higher excited ionic states require far more energy and their transition dipole matrix elements are far smaller [11].

In case of multiphoton ionization dissociative ionization is mostly treated as a two-step process, which we call "Two-Step Mechanism" in all further correspondence. First, the neutral hydrogen molecule is promoted to the $1s\sigma_g$ curve and an electron is emitted. Only after some time, when the vibrational wavepacket has evolved towards larger internuclear distances, another photon absorption takes place and the $2p\sigma_u$ level is reached (see black pathway in fig. 2.13). This last step can only happen via absorption of an odd number of photons due to the rules of point group theory as introduced in sec. 2.4.2.

The idea of two independent absorption processes leads to an interesting implication: If the first step of dissociative ionization is identical to bound ionization, the measurement result of any quantum-mechanical observable for the bound and dissociative pathways has to be the same. In other words: From just looking at the emitted electron it is not possible to determine whether it was emitted during a bound or dissociative ionization process. Mi *et al.* [7] measured the electron energy spectra of bound and dissociative ionization. Besides a small energy region below 0.5 eV the spectra look identical as expected according to the Two-Step Mechanism. However, there is a slight deviation at low electron energies. Mi *et al.* [7] gives a possible explanation for this discrepancy including autoionizing Rydberg states. Nevertheless experimental evidence is missing to get further information on the exact ionization pathways.

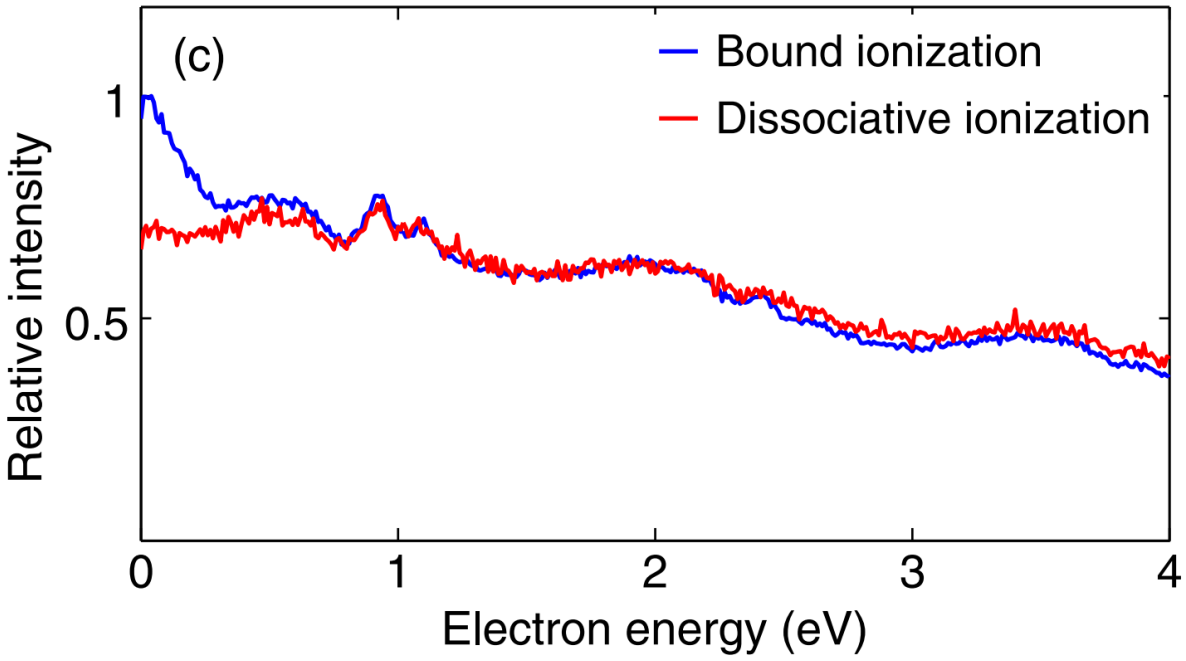

Figure 4.1.: Experiment, results and figure by Mi *et al.* [7]. Electron energy spectrum for bound and dissociative ionization of H_2 using 25 fs linearly polarized pulses with 800 nm central wavelength. The photofragments were imaged with a reaction microscope.

In this thesis we will provide more experimental data and explanations to the question of how bound and dissociative ionization differ from each other at larger photon energies.

4.2. Charge resonance enhanced ionization

In 1995 Seideman *et al.* [59] calculated that the ionization rate of a molecule increases significantly at large internuclear distances. In addition Zuo & Bandrauk [60] could theoretically show this for H_2^+ molecular ions, that are aligned parallel to a linearly polarized laser field (fig. 4.2). The maximum ionization yield is reached at the so called critical distance, where the chemical bond starts to break. One year later Constant *et al.* [61] observed this enhanced ionization at large internuclear distances in the ionization of I_2^+ in agreement with the calculations by Seideman *et al.* [59].

Theoretically, the enhanced ionization can be explained in terms of electron localization (see fig. 4.3). In the presence of a strong laser field the $1s\sigma_g$ and $2p\sigma_u$ states of H_2^+ superimpose to the σ_+ and σ_- states. These states describe electron localizations at one or the other nuclei. When the laser field oscillates, the energies of the two charge

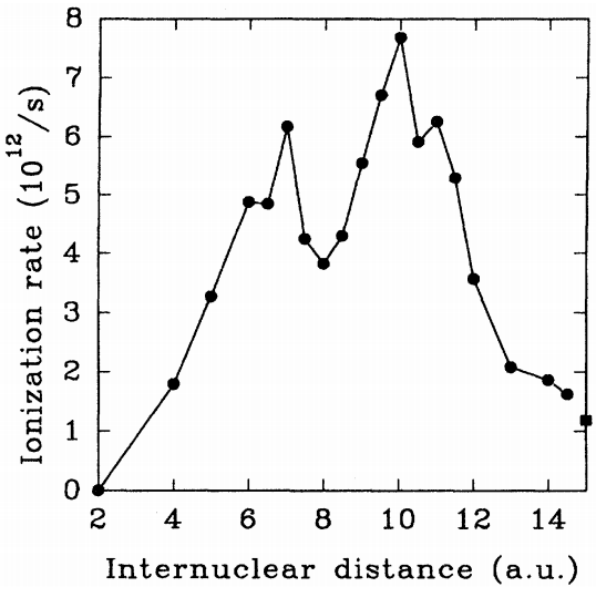

Figure 4.2.: Maximum in simulated ionization rate for H_2^+ at R=10au in 10^4W/cm^2, 1064-nm linearly polarized laser field compared to the ionization rate of atomic hydrogen (square on the right vertical axis). Simulation performed by and figure taken from Zuo & Bandrauk [60].

resonance states moves accordingly up and down. For small internuclear distances the electron can always go from the higher to the lower energetic state because the barrier between the two nuclei is smaller than the energy levels. As the internuclear distance increases the electron can be trapped in the higher energetic state. Mulliken was the first to discuss these states and named them charge resonance states. The electron can tunnel through the barrier and the H_2^+ molecule gets ionized (fig. 4.3 (c)). It turns out that there is a critical internuclear distance at which the neighboring nuclei leads to a decrease in the height of the tunnel barrier, such that the ionization happens just right above the barrier (fig. 4.3 (b)). Furthermore the higher coupling between the two states at higher internuclear distances leads to an increased population of the σ_+ state. These two effects in combination cause a maximum in the ionization rate at R$\approx 10au$.

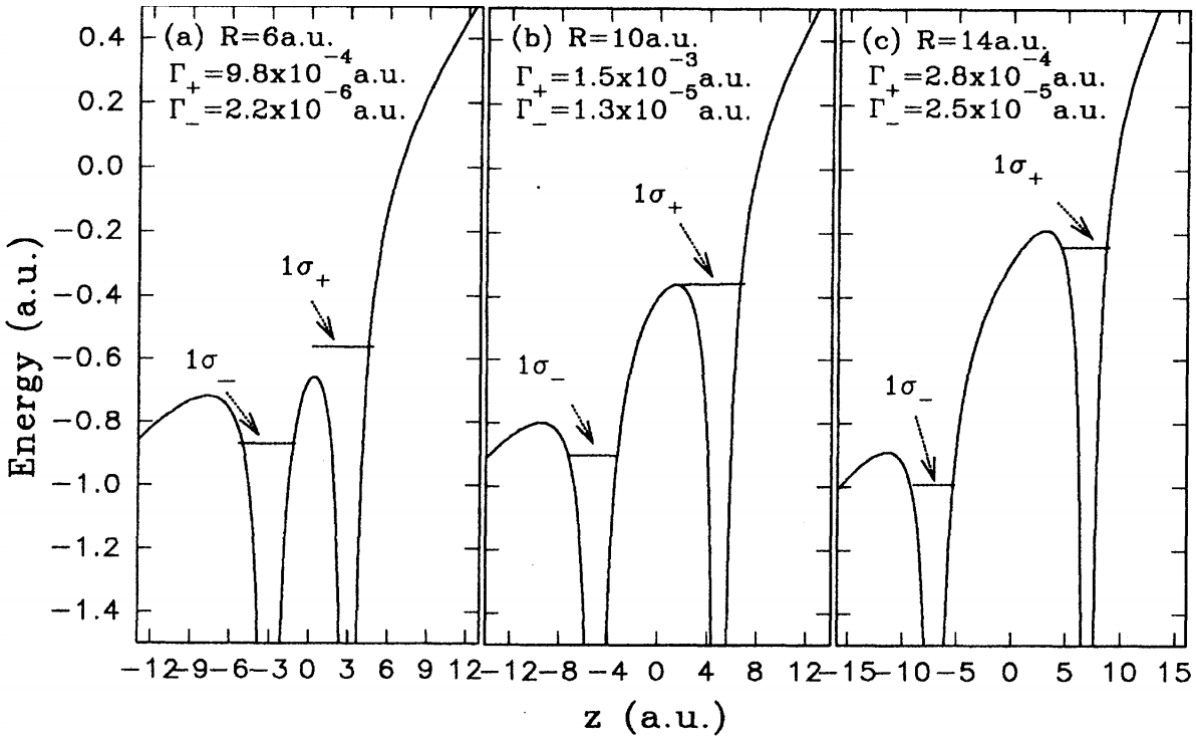

Figure 4.3.: Charge Resonance Enhanced Ionization due to efficient electron localization. See text for explanation. Figure taken from [60]

4.3. Bond-softening and -hardening

Fig. 4.4 shows the lowest potential energy curves of the H_2^+ molecular ion as black solid and dashed lines when no external electric field is present. If the molecule is oriented parallel to a strong, linearly polarized laser field, the electron density gets distorted and polarized. This dipole moment increases with internuclear distance and the electron gets pushed to one of the nuclei. Due to the interaction with the laser field the electronic energy levels will no longer look the same like in the undisturbed case. A bound state forms, which unfolds a local minimum in the potential energy curve (red line in fig. 4.4). At sufficiently large internuclear distance the bond is weakened such that the molecule "cannot hold any vibrational states" (Brabec [63, p. 198]) anymore and the system prefers an unbound molecular state, in which a proton and a neutral hydrogen atom repel each other.

This phenomenon, called Bond-Softening, can be theoretically described by using the Floquet picture (see sec. 2.4.2 and fig. 4.4). The resulting potential energy curves in blue and red show clearly that the dissociation barrier of the $1s\sigma_g$ curve is lowered, which is called Bond-Softening. The absorption of three photons is no longer a vertical

transition from the ground to the excited curve, but a horizontal run on the $|\sigma_u, n = 3\rangle$ curve. In an analogue way the blue curve forms a potential well where high vibrational states of the H_2^+ ion can be trapped which is called Bond-Hardening.

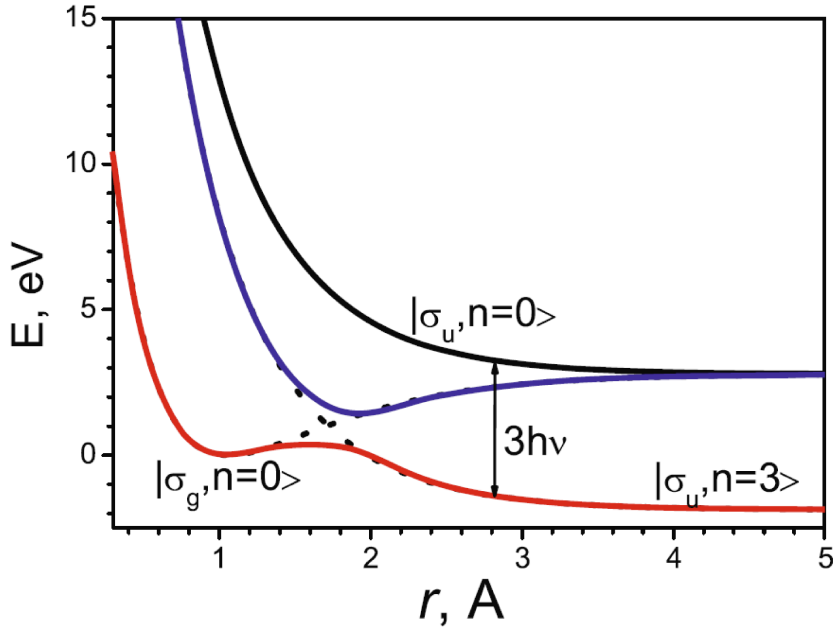

Figure 4.4.: Bond-Softening (red) and -Hardening (blue) for absorption of three photons explained via the Dressed Molecule Picture. The undressed $1s\sigma_g$ and $2p\sigma_u$ states of the H_2^+ ion are labeled $|\sigma_g, n = 0\rangle$ (black, dashed) and $|\sigma_u, n = 0\rangle$ (black, solid). The dressed states in red and blue avoid the crossing between the $|\sigma_g, n = 0\rangle$ ground state and the $|\sigma_u, n = 0\rangle$ excited curve, that is shifted down by three photons. Figure taken from Brabec [63, p. 198].

In 1981 Bandrauk & Sink theoretically predicted Bond-softening for the first time in the dissociation of Ar_2^+.

4.4. Asymmetric bond breaking in dissociation

Asymmetric bond breaking in dissociation refers to the fact that the bound electron can only locate on one of the two separating protons. Experiments showed, that it is possible to control at which of the two protons this electron will probably locate based on the electric field that is used. Ray *et al.* [4] used an 800-400 nm Two-Color Setup to create an asymmetric field. By tuning the phase shift between the 400 nm and 800 nm pulses the maximum electric field strength amplitude of the total pulse can point either down- or upwards. They observed that there is no general rule which of

the two ion emission directions (along or opposite to the electric field asymmetry) is preferred in dissociation. The ion emission direction depends on the ion kinetic energy and the underlying mechanism of dissociation in detail. Xu *et al.* [65] were able to control the bond breaking in real time by utilizing a 750 nm pump-probe experiment to investigate the time dynamics of the break-up. They found out that the electron localization happens 15fs after initial ionization of H_2 at an internuclear separation of 8a.u.

4.5. Electron-nuclear energy sharing

Like any other physical phenomena photoionization obeys energy conservation. The energy, that is released during the photoionization in form of kinetic and radiative energy, has to be the same as the energy that is given to the system in form of photons and energy previously stored in the molecule. How the energy is shared between the fragments depends on the individual system and reflects the dynamics of the fragmentation. This is why resolving the energy sharing is an important step towards understanding the molecular dynamics during and after laser interaction. In order to experimentally confirm energy conservation and to resolve how the energy is distributed, it is necessary to measure the kinetic energies of all photofragments.

In bound ionization the photon energy is partially shared between the H_2^+-ion and the emitted electron. Another part of the photon energy can be internally stored in the nuclear motion of the H_2^+-ion in form of vibrational and rotational energy. The nuclear states can act as an energy sink that can not be measured without destroying the molecule. Resolving the energy sharing in the case of bound ionization is therefore not directly possible.

When H_2^+ dissociates the proton and electron can only have kinetic and no potential energy since they do not belong to a bound system anymore. But in general the original H_2^+ might dissociate into a neutral ground state or excited hydrogen atom serving as an energy source. In theory however, calculations show that the H_2^+ molecular ion can be well described by a two-level-system ($1s\sigma_g$, $2p\sigma_u$) because these states are well separated from higher ones[11].

In fact, energy conservation could be confirmed and thoroughly explained in H_2 dissociation by Wu *et al.* [66] and Lu *et al.* [67]. In fig. 4.5(a) the kinetic energy sum of both ions, also called the kinetic energy release (KER), is plotted vs. the electron energy in a 2D histogram. This type of plot is called Joint-Energy-Spectrum (JES). One can see

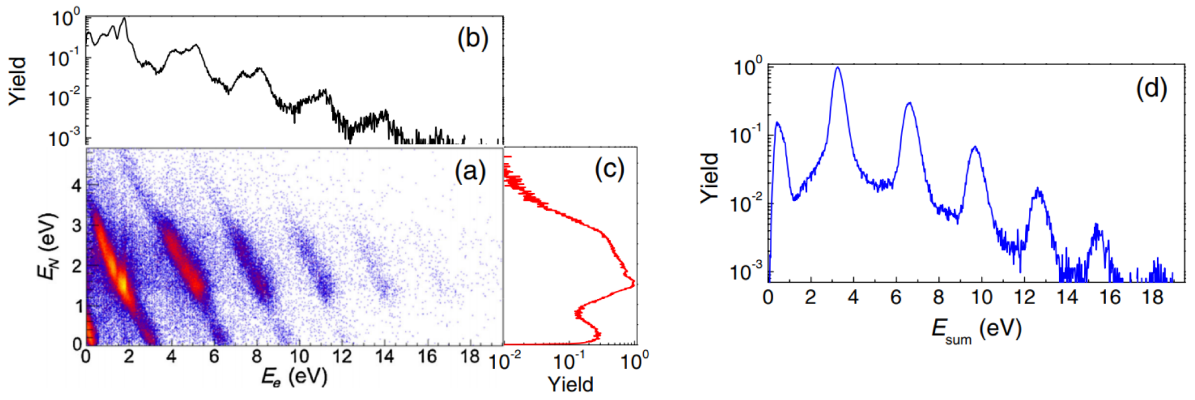

Figure 4.5.: Experiment, results and figure by Wu *et al.* [66]. Left: Joint-Energy-Spectrum (JES) for the dissociation channel of H_2 using 52fs linearly polarized pulses with 390nm central wavelength, I=5.9×10^{13}W/cm^2. Right: Histogram of the sum of ionic and electron kinetic energy. Photofragments were imaged with a reaction microscope.

distinctive, diagonal lines that are separated by the photon energy of roughly 3.1eV. Fig. 4.5(b) shows a histogram of the sum energy of ion, hydrogen atom and electron. Here the diagonal lines from fig. 4.5(a) appear as separated peaks. In order to realize why the lines are forming, it helps to write down the energy balance of the process.

$$n\omega = E_N + E_e + I_p + U_p \Leftrightarrow E_N + E_e = n\omega - (I_p + U_p)$$

Here I_p and U_p describe the ionization potential of H_2 and the ponderomotive potential respectively. It gets directly clear that the relation ship between E_N and E_e is linear with slope -1. So, the lines form due to energy conservation and thus they are called conservation lines.

Energy conservation of course also holds for any other ionization channel. Lu *et al.* [68] observed and explained the conservation lines also for double ionization (fig. 4.6). This time there are two protons and two electrons that enter in the energy balance. V_g describes the potential energy of the H_2 ground state.

$$E_N + E_{e1} + E_{e2} = n\omega - (V_g + U_{p1} + U_{p2})$$

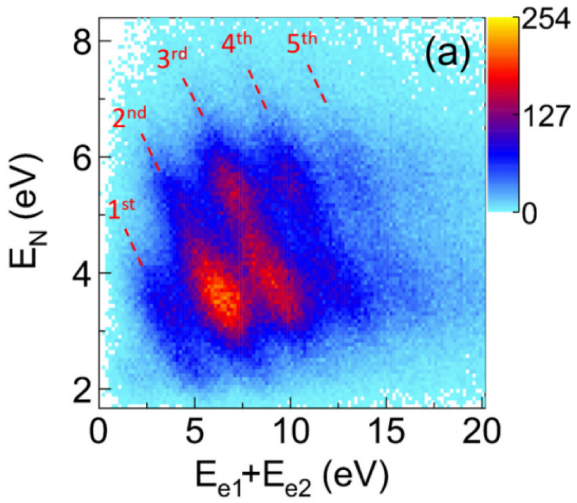

Figure 4.6.: Experiment, results and figure by Lu *et al.* [68]. JES for the double ionization channel of H_2 using 60fs linearly polarized pulses with 395nm central wavelength, I=1.1×10^{14}W/cm^2. Photofragments were imaged with a reaction microscope.

5. Experimental setups and methods

5.1. Femtolaser

Our Titan:Saphir(Ti:Sa)-lasersystem is able to produce ultrashort laser pulses. The setup, that was used in this thesis, is based on the chirped pulse amplification scheme after Strickland & Mourou [69] (fig. 5.1). In principle short pulses are first stretched in time in order to prevent any damage to the amplification medium due to too high laser intensity. This introduces a strong chirp to the laser pulses. Afterwards they are amplified by using a Kerr medium. Finally the pulses are compressed in time to get as short and intense pulses as possible with ideally no chirp. Fig. 5.2 shows an overview of

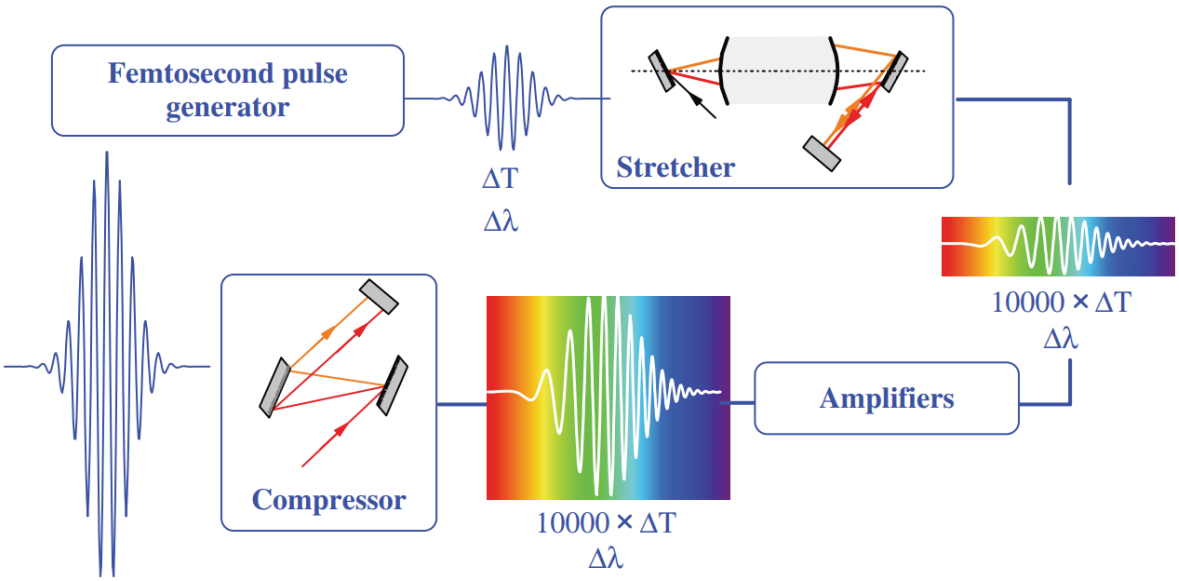

Figure 5.1.: Schematics of chirped pulse amplification [70, p. 18]. ΔT and $\Delta\lambda$ describe the pulse duration and spectral width of the laser pulses at the different stages during generation.

the different femtolaser modules. The oscillator module gets green light (530 nm) from

a frequency-doubled Nd:YVO continous-wave laser. Infrared pulses (800 nm central wavelength, 80 MHz repetition rate) are generated and stretched in time by a dispersion control unit. The long infrared pulses are guided to the amplifier module. Here a high power Nd:YLF pulsed laser (530 nm, 150 ns) is used to pump the Kerr medium, which amplifies the incoming IR pulses. In the last stage the pulses are compressed using chirped mirrors and prisms. Finally femtosecond pulses can be produced with a repetition rate of 3 kHz, pulse energies of the order of 1 mJ and durations down to 25 fs.

5.1.1. Oscillator

A green continous-wave laser beam enters a cavity with a Ti:Sa-crystal as the Kerr-medium inside. The Ti:Sa-crystal absorbs the green light and emits IR light. A trigger appliance allows to manually reduce the cavity length by several cm within a fraction of a second. This introduces a small power fluctuation of the continous wave, which initializes the pulse. This initial pulse is then amplified due to the Kerr lens effect like explained in sec. 2.1.2. The laser pulses are guided to the dispersion control unit. Here they pass two pairs of chirped mirrors to compensate for normal dispersion caused by all previous optical elements. Afterwards the pulse stretcher, a strongly dispersive element, introduces a frequency chirp and thereby elongates the pulses by a factor of $10^3 - 10^4$ [70, p. 20]. At the end a back-reflecting mirror is mounted to let the beam pass the stretcher a second time. Thus the peak intensity is drastically reduced.

5.1.2. Amplifier

The stretched pulses reach a second Ti:Sa-crystal in a cavity, which is pumped by a Nd:YLF pulsed laser operating at a repetition rate of 3 kHz. After having passed the crystal five times the IR pulses are sent through a Pockels cell. This fast switching time-gated polarisation device stores pulses for several round trips allowing only every 10th-20th pulse to couple out [70, p. 23]. This leads to a first amplification. Afterwards the preamplified pulses pass the Kerr medium another four times until they are finally guided to the compressor unit.

5.1.3. Compressor

After successful pulse amplification the pulse duration is decreased by compensating the normal dispersion caused by the stretcher in the oscillator module and optical elements

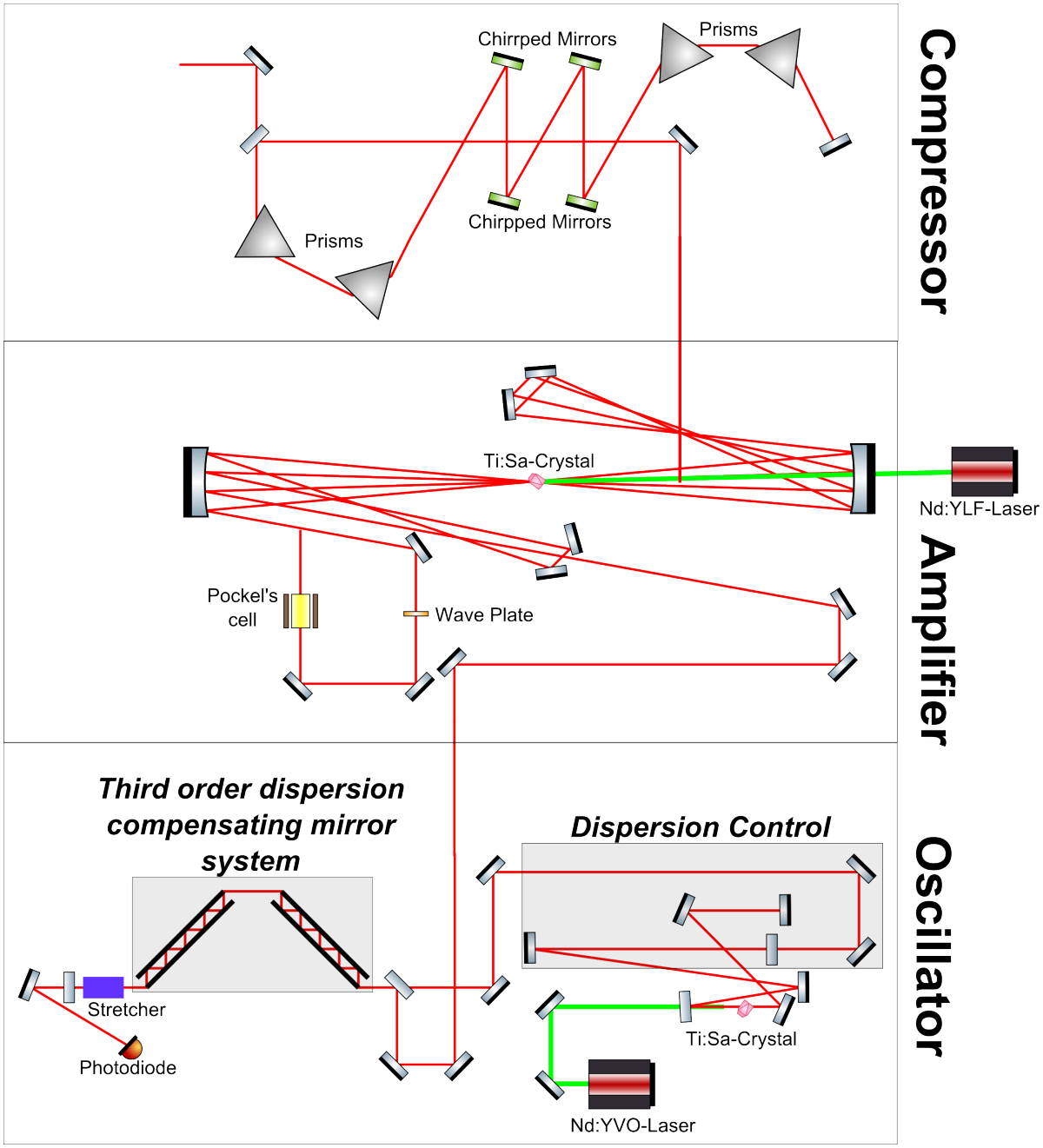

Figure 5.2.: Overview of the femtolaser setup. See text for explanation.

in the amplification stage. For this purpose chirped mirrors and a prism compressor are used like explained in Section 2.2.3. A detailed and comprehensive description of Ti:Sa-femtolasers can be found in [70].

Fig. 5.3 shows the measured laser spectrum and autocorrelation trace. The FWHM of the spectrum is roughly 50nm. In case of a gaussian pulse shape the FWHM of the temporal pulse profile is given by the autocorrelation FWHM divided by a deconvolution factor of $2\sqrt{2\ln(2)}$, which results in a measured pulse duration of 33fs [71, p. 993 table 2].

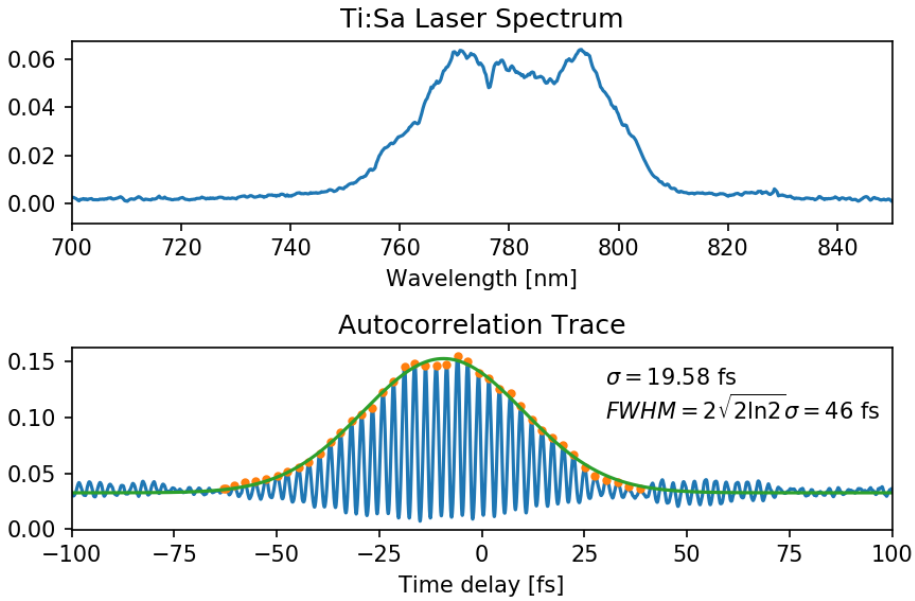

Figure 5.3.: Top: Wavelength spectrum of the Ti:Sa laser after the compressor. Bottom: Measurement of the pulse duration with a commercial Michelson interferometer-based autocorrelator (model "FEMTOMETER" by "spectra-physics"). The signal was fitted assuming a gaussian pulse.

5.2. Pulse shaper - Zero-dispersion compressor in 4f-geometry

All of the fundamental steps in the process of spectral pulse shaping from p. 16 can be realized by two optical elements: Holographic gratings and Spatial Light Modulators (SLM). Fig. 5.4 shows the spectral pulse shaping setup that was used during this thesis. The femtolaser pulses are guided through a holographic grating which splits up

the light into the different frequency components. In order to collimate the diverging multicolor beam a cylindrical mirror CM1 is used. The collimated beam passes two SLMs, where each frequency aquires an amplitude modulation and phase shift that can be arbitrarily chosen. Finally the multicolor beam is focused again with a second cylindrical mirror CM2 and spectrally recombined with another holographic grating HG2. The distances between HG1 and CM1, CM1 and SLM, SLM and CM2, CM2 and HG2 equal the focusing length of the cylindrical mirrors which is f=22.5cm, so the beam travels a distance of 4f inside the pulse shaper setup. The pulse shaper setup was

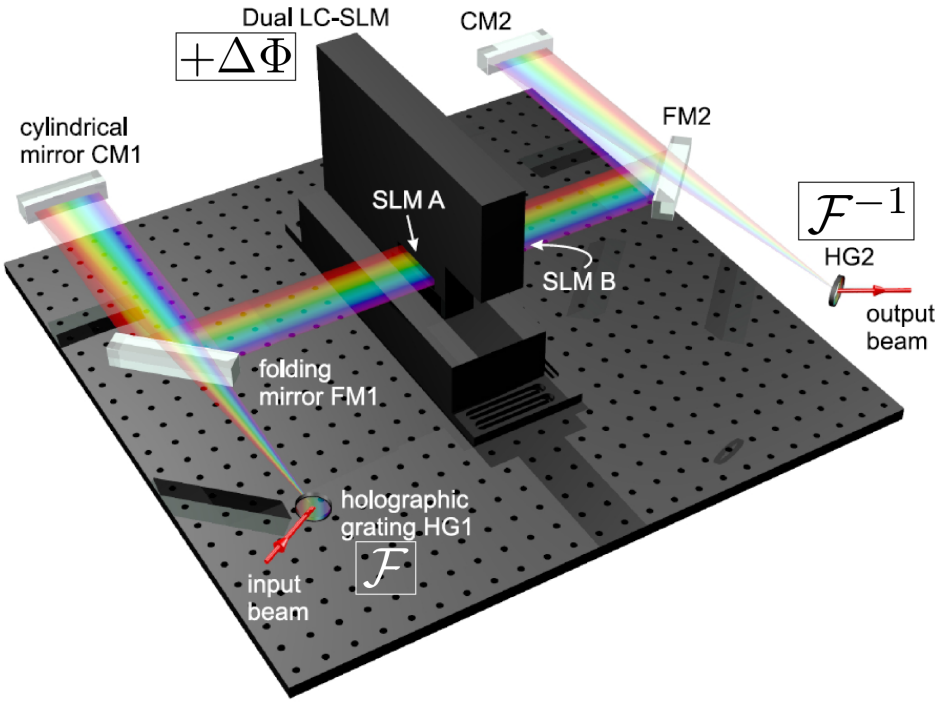

Figure 5.4.: Figure taken and adapted with kind approval from Kerbstadt [19]. The holographic gratings HG1 and HG2 are responsible for the spectral decomposition of the laser beam. The SLM applies the phase shifts to the different frequency components.

built in cooperation with Dr. Stefanie Kerbstadt from the Ultrafast Coherent Dynamics working group under the supervision of Prof. Dr. Matthias Wollenhaupt from the University of Oldenburg. For a complete and detailed description of this pulse shaper setup, its working principle, the alignment and calibration procedure as well as possible pulse characterization methods please see Kerbstadt [19]. In the following, the individual components of the pulse shaper setup are briefly explained.

5.2.1. Volume phase holographic grating

A Volume Phase Holographic (VPH) grating (see fig. 5.5a) is usually made from a photosensitive gelatin grating that is surrounded by fused silica plates. This gelatin material has a sinusoidal refractive index modulation pattern that allows light to diffract when it passes through like in conventional reflection gratings (see fig. 5.5c). The path difference through the mth diffraction order can be calculated via

$$m\lambda = a[\sin(\beta) + \sin(\alpha)]\,, \tag{5.1}$$

where a describes the line spacing of the grating. Different frequency components get diffracted under different outgoing angles. This allows for a spatial dispersion of the laser's frequency spectrum.

VPH gratings are blazed gratings in Littrow configuration, which means that they are optimized to achieve a maximum power efficiency in a given diffraction order for a given central wavelength. In this case it is the first order. In Littrow configuration the incident angle between the laser beam and the surface normal of the grating equals the outgoing angle. There is only one specific angle at which the power in the first diffraction order is maximum. In our case this angle is 10.8°. For the Littrow configuration eq. (5.1) simplifies to

$$2a\sin(\alpha) = m\lambda\,.$$

Here, gratings with 1500 lines per mm where used. This choice was found in calculations by Kerbstadt [19, sec. A.3] to yield an optimum resolution for the spectral bandwidth given by our Ti:Sa laser.

5.2.2. Spatial light modulator

Fig. 5.6a shows the layout of a liquid crystal display. One display consists of 640 individual liquid crystals plus electrodes and an alignment layer. The electrodes consist of a thin layer of Indium Tin Oxide (ITO) where voltages between 0 to 4.5V (Low Voltage) or 0 to 8V (High Voltage) can be applied independently from each other (fig. 5.6b). The liquid crystal molecules form an anisotropic medium. In case of no electric field the molecules are aligned parallel to the alignment layer. As soon as the electric field is switched on the molecules start to tilt towards the z-direction. The bigger the electric field the smaller the angle Θ between the z-direction and the molecular axis. The

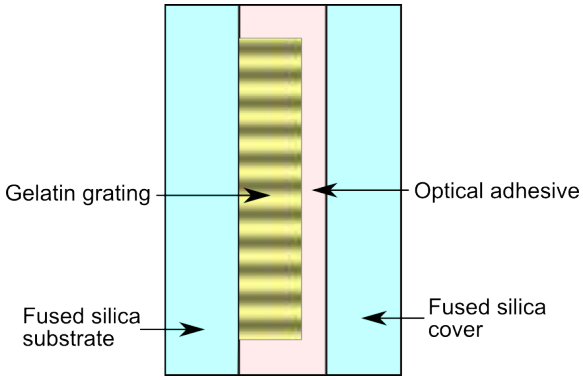

(a) Layout of a VPH grating. A fused silica substrate is coated with a gelatin plate. Next the gelatin layer is exposed to a holographic interference pattern like shown in fig. b). Afterwards the processed gelatin material is put into multiple liquid baths in order to obtain the desired refractive index modulation pattern. Finally a second fused silica cover is glued to the gelatin grating for protection.

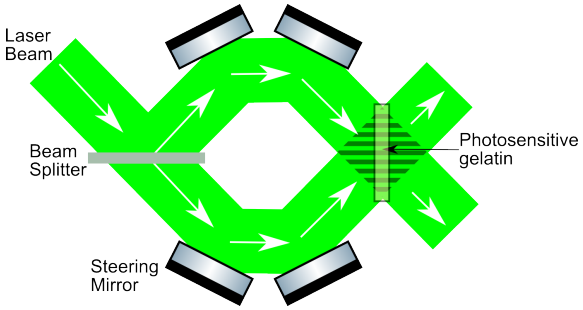

(b) Manufacturing process of a gelatin grating. A coherent monochromatic laser is split into two beams that get overlapped again at a well-defined angle such that a sinusoidal interference pattern forms. The photosensitive gelatin is placed in the crossing point of both beams in order to imprint the desired modulation pattern.

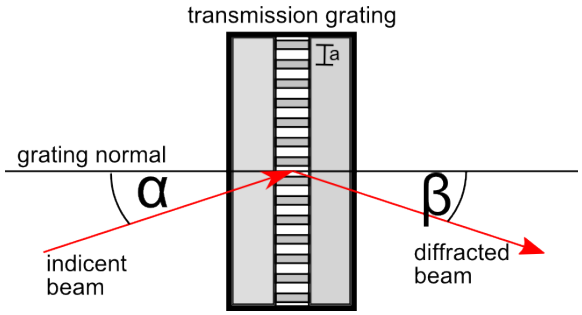

(c) Diffraction of light on a VPH transmission grating. The incident beam hits the grating under an angle α with respect to the surface normal. The zeroth diffraction order that does not experience any path difference passes straight trough while the first order is deflected by an angle β with respect to the surface normal.

Figure 5.5.: Layout, manufacturing process and beam path sketch for VPH gratings.

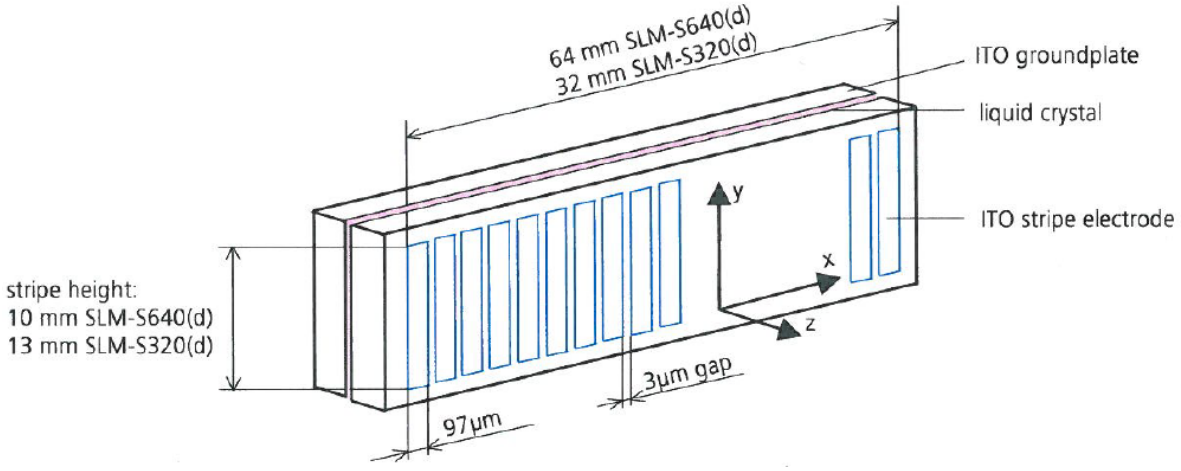

(a) Layout of a liquid crystal display. Each stripe (blue) is an individual electrode. In between the two glass plates (white) there is a liquid crystal cell (pink).

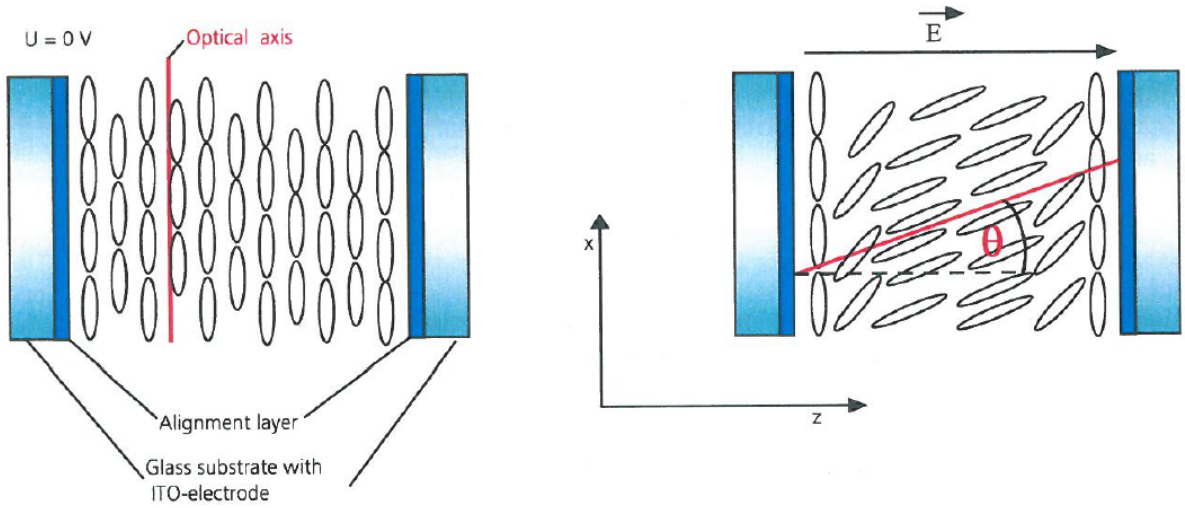

(b) Layout of a single liquid crystal cell. On top of the electrodes (interface between light and dark blue) there is an alignment layer to define the optical axis when no field is applied. In between a thin layer of liquid crystals acts as a birefringent medium.

Figure 5.6.: Figures taken from the technical documentation of the used SLM [72]

liquid crystal molecules act as a birefringent material. The optical axis is identical to the molecular axis. By changing the applied voltage and thereby Θ the effective refractive index can be changed in a well-behaved manner. Thus the incident polarization and absolute phase of an individual frequency component can be controlled.

The liquid crystal acts as a birefringent medium. The extraodinary component lies in the plane between laser propagation direction and the optical axis. Its refractive index $n_e(\omega, U)$ depends on the angle between optical axis and the laser propagation. The ordinary component is oriented perpendicular to the afore mentioned plane. Its

refractive index $n_o(\omega)$ is independent of θ. As for all birefringent materials the effective refractive index $n(\theta)$ along the extraordinary axis is

$$\frac{1}{n(\omega,\theta(U))^2} = \frac{\cos^2(\theta(U))}{n_0(\omega)^2} + \frac{\sin^2(\theta(U))}{n_e(\omega)^2}\,.$$

The angle $\theta(U)$ depends on the applied voltage. The acquired phase of the extraordinary and ordinary polarization components can be calculated via the optical path length. Here attention has to be paid to also consider the two glass plates (thickness g) around the liquid crystal cell (thickness d).

$$\begin{aligned}\phi_o &= \frac{\omega}{c}\left(n_0(\omega)d + 2n_g(\omega)g\right)\,,\\ \phi_e &= \frac{\omega}{c}\left(n(\omega,\theta(U))d + 2n_g(\omega)g\right)\,.\end{aligned}$$

The difference between the ordinary and extraordinary phase is

$$\Delta\phi(\omega,U) = \phi_e - \phi_o = \frac{\omega}{c}(n(\omega,\theta(U)) - n_o(\omega))d\,. \tag{5.2}$$

5.2.3. Calibration of the SLM

For the calibration of the SLM it is essential to know two things: the phase function $\Delta\phi(\omega,U)$ (phase-voltage calibration) from eq. (5.2) and which wavelength is assigned to which pixel of the SLM-displays (pixel-wavelength calibration). In order to measure $\Delta\phi(\omega,U)$, it is necessary to determine the refractive index difference $\Delta n(\omega,\theta(U)) = n(\omega,\theta(U)) - n_o(\omega)$, which we can rewrite using eq. 5.2.2 to get

$$\begin{aligned}\Delta n(\omega,\theta(U)) &= n_o(\omega)\left(\frac{n_e(\omega)/n_o(\omega)}{\sqrt{1+((n_e(\omega)/n_o(\omega))^2-1)\cos^2(\theta(U))}} - 1\right)\\ &= n_o(\omega)f(U)\end{aligned}$$

$f(U)$ is a function that is normalized to 1 and describes the voltage dependence of the phase difference $\Delta\phi(\omega,U)$. In order to perform the phase-voltage calibration $n_o(\omega)$ and $f(U)$ have to be determined. This procedure has been carried out and is explained in detail by Kerbstadt [19, sec. 3.1]. In the further course of this section only a very brief description of the calibration procedure is given. The interested reader is referred to Kerbstadt [19]. Two polarizers are installed in front of and after the SLM. Their polarization axes are turned $\pm 45°$ with respect to the table normal. The transmission

curve $T(\Delta\phi(U)) = \sin^2(\frac{\Delta\phi(U)}{2})$ as a function of the applied voltage is measured with the help of a photodiode [72]. The light source is a monochromatic HeNe-laser ($\lambda = 633nm$). To retrieve the phase function the transmission curve is inverted via

$$\Delta\phi(U) = 2k\pi \pm \arcsin\left(\sqrt{T}\right) \quad \text{with} \quad k = 0, 1, \cdots . \tag{5.3}$$

k and the sign of the arcsin-term is chosen based on the neighboring extreme values. The

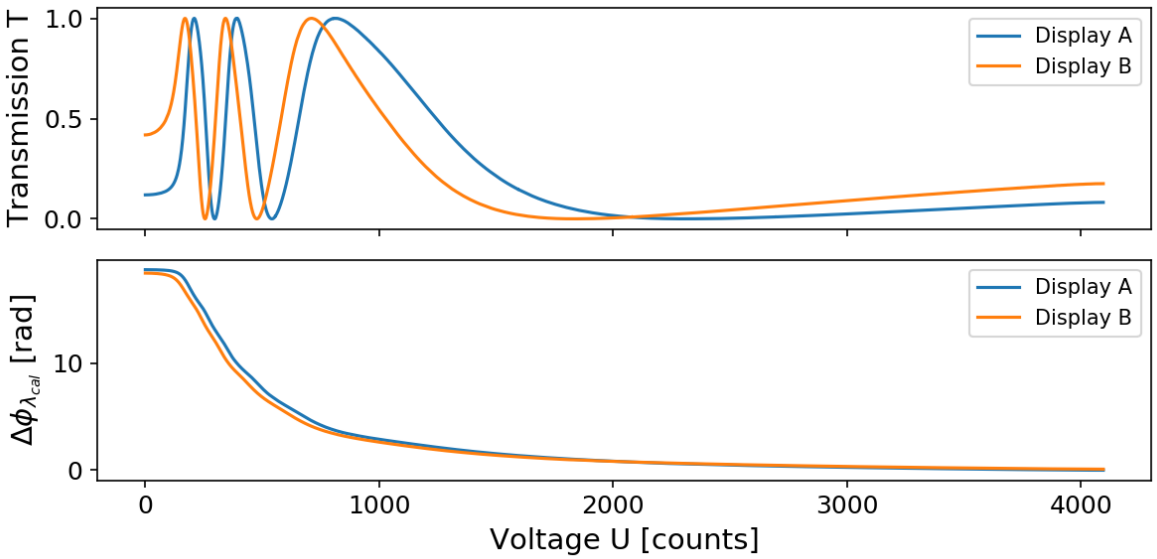

Figure 5.7.: Phase-voltage calibration. Top: Measured transmission curve as a function of the applied voltage for a calibration wavelength of 633nm (HeNe-laser) for each of the two SLM displays. In the low-voltage mode within a range of 0-4V the voltage can be tuned to 4095 equidistant values called counts in this plot. Bottom: Final phase function as retrieved from the inversion of the transmission curve (see eq. (5.3)). The data were taken and analyzed by Kerbstadt [19, sec. 3.1] in Oldenburg.

phase function $\Delta\phi_{\lambda_{cal}}$ describes the voltage dependence only at the specific wavelength λ_{cal} that was used in the calibration procedure. The general phase function for arbitrary wavelengths is given by [72, sec. 5.5.3]

$$\Delta\phi(U,\lambda) = \Delta\phi(U,\lambda_{cal})\frac{\lambda_{cal}}{\lambda}\frac{\Delta n(\lambda)}{\Delta n(\lambda_{cal})} \quad \text{with} \quad \Delta n = \frac{0.2002 \cdot \lambda}{\sqrt{\lambda^2 - (327,44nm)^2}}$$

For the wavelength pixel calibration two broadband polarizer plates with horizontal alignment with respect to the laser table have to be put - one in front and after the

SLM. The incoming laser pulse is p-polarized. At the end of the setup a spectrometer is placed to measure the transmitted spectrum. All the display pixels of the SLM have to be switched dark before the calibration by choosing the voltage at which the transmission curve $T(U)$ is minimal. Then one after another the transmission of each pixel is switched on and the spectrum is recorded (fig. 5.8 left). Each spectrum shows a narrow peak that accords to the transmitted wavelength. By using a peak-finding routine the central wavelength is determined. Here always the position of the peak maximum is used as the central wavelength (fig. 5.8 right).

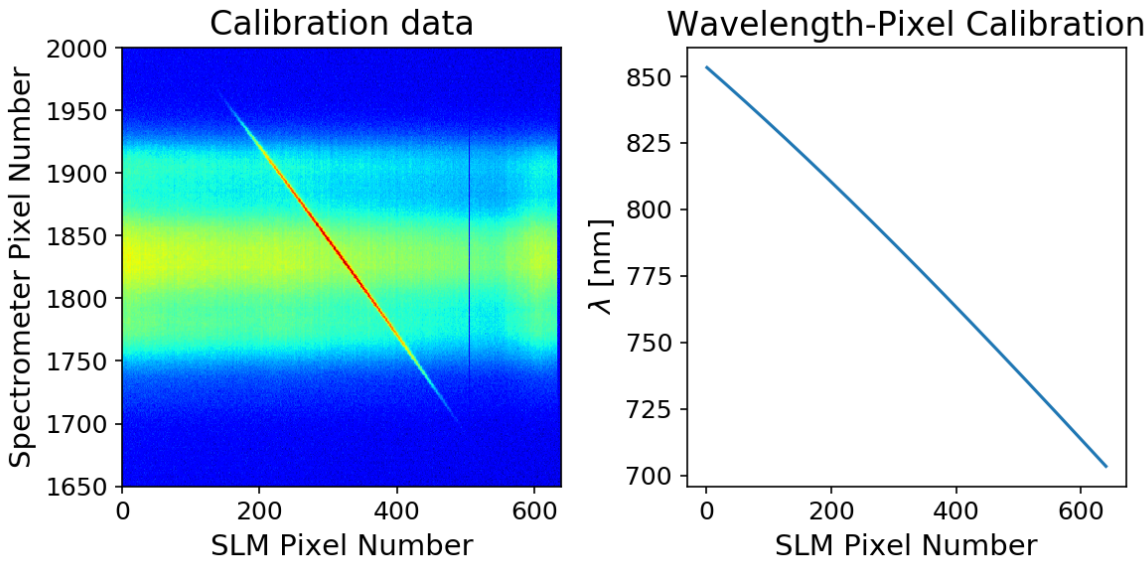

Figure 5.8.: Pixel-wavelength calibration. Left: Measured spectra for switching on the different SLM pixels. Right: Final pixel-wavelength calibration curve as determined from the maximum values of the left plot. The data were taken by Kerbstadt [19, sec. 3.1] in Oldenburg using a similar Ti:Sa-femtolaser as described in 5.1

5.2.4. Pulse compression and phase-shaping Software

Since the pulse shaper can apply arbitrary frequency-dependent phase shifts, it can also be used as a pulse compressor. To compensate for dispersive effects due to the optics in the laser and phase shaper setup the Group-Delay-Dispersion and Third-Order-Dispersion play the most important roles [19, p. 14]. In order to find the optimum phase shift to compensate for the GDD and TOD a LabView-Software written by Kerbstadt [19] is used (fig 5.9). The Software systematically sets different GDD (c_1) and TOD (c_2)

values, calculates the according phase function $\Delta\phi(\omega)$, finds the right voltages $U(pix)$ that have to be applied to each pixel of both SLM displays by using the calibration from sec. 5.2.3 and sends these to the SLM of the phase shaper. The shaped pulses are guided to the ReMi where they ionize H_2 molecules. The shorter the pulse the more intense it is and the higher the count rate of detected ions. This count rate is transferred from the ReMi to the software in form of a voltage that ranges between 0 and 10 Volts. The PC reads the count rate voltage using a National Instruments BNC-2110 box. The combination c_1, c_2 where the count rate is maximum is the optimum pulse compression and is used for all measurements to ensure the shortest possible pulses.

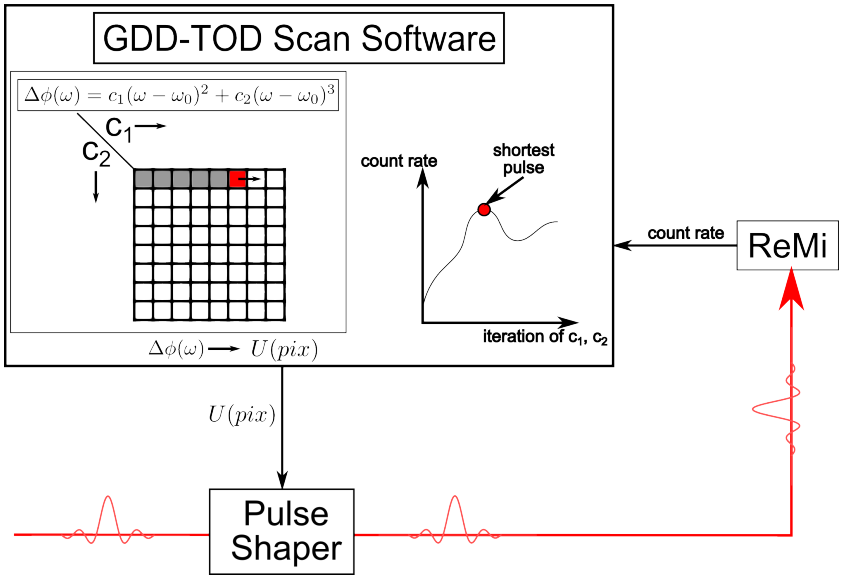

Figure 5.9.: Working principle of the GDD-TOD optimization software. See text for explanation.

In order to shape the compressed pulses another software allows to apply phase functions to each of the two SLM displays of the following form:

$$\Delta\phi(\omega) = A\sin(b(\omega-\omega_0)) + \sum_{i=0}^{12} c_i(\omega-\omega_0)^i$$

The parameters $A, b, \omega_0, \{c_i\}$ have to be entered manually. These can be set differently for display A and B in general. In addition the optimum GDD- and TOD-values for pulse compression from the previous GDD-TOD-Scan are automatically added to both displays. The software determines the right voltages per pixel based on the afore mentioned calibration and sends them to the SLM.

5.3. Reaction microscope

The Reaction Microscope, also known as Cold Target Recoil Ion Momentum Spectroscopy (COLTRIMS), is an imaging technique that allows for the measurement of the fragmentation of atoms and molecules. Photoionization of atoms and molecules sets free ions and electrons that are extracted to position and time sensitive detectors by means of electric and magnetic fields. From the received images and time-of-flight it is possible to reconstruct the full 3D momentum vectors of the charged fragments. Since the momentum vectors of ions and electrons from the same laser shot are retrieved, it is possible to select the particles that come from the same ionization event by checking for momentum conservation.

The general setup and principle of the apparatus is shown in 5.10. A cold supersonic gas jet is overlapped with a laser beam in the center of the spectrometer leading to ionization of the gas atoms. The pulsed laser beam is focused with the help of a focusing silver mirror (f=7.5 cm). The spectrometer itself consists of multiple ring electrodes with a spacing that is much smaller than the electrode's diameter. Neighboring electrodes are electrically connected via same ohmic resistances. By applying a voltage across the first and last electrodes the potential increases linear with the position inside the spectrometer and therefore a homogenous electric field pointing parallel to the spectrometer axis is generated. Right in front of the electron detector there is a region without electric field called the drift zone. By using a pair of Helmholtz coils a homogenous magnetic field parallel to the electric field is created. The electric field forces the ions and electrons, which are initially located in the center of the spectrometer, towards the detectors at the ends of the spectrometer. The magnetic field forces the electrons on a spiral trajectory leaving the ion trajectories mostly unaffected because of their higher mass.

The complete vaccuum setup is shown in fig. 5.11. The target gas is released from a high-pressure gas reservoir trough a tiny nozzle of several tens of μm. After passing two skimmers the gas particles pass through four differential pumping stages (labeled with numbers 3, 4, 5 and 6) before they reach the main chamber. Here the vacuum reaches $\approx 10^{-11}$ mbar and the COLTRIMS spectrometer as presented in fig. 5.10 is mounted. To ensure optimal removal of residual gas particles, that were not ionized, the jet line ends with a dump stage.

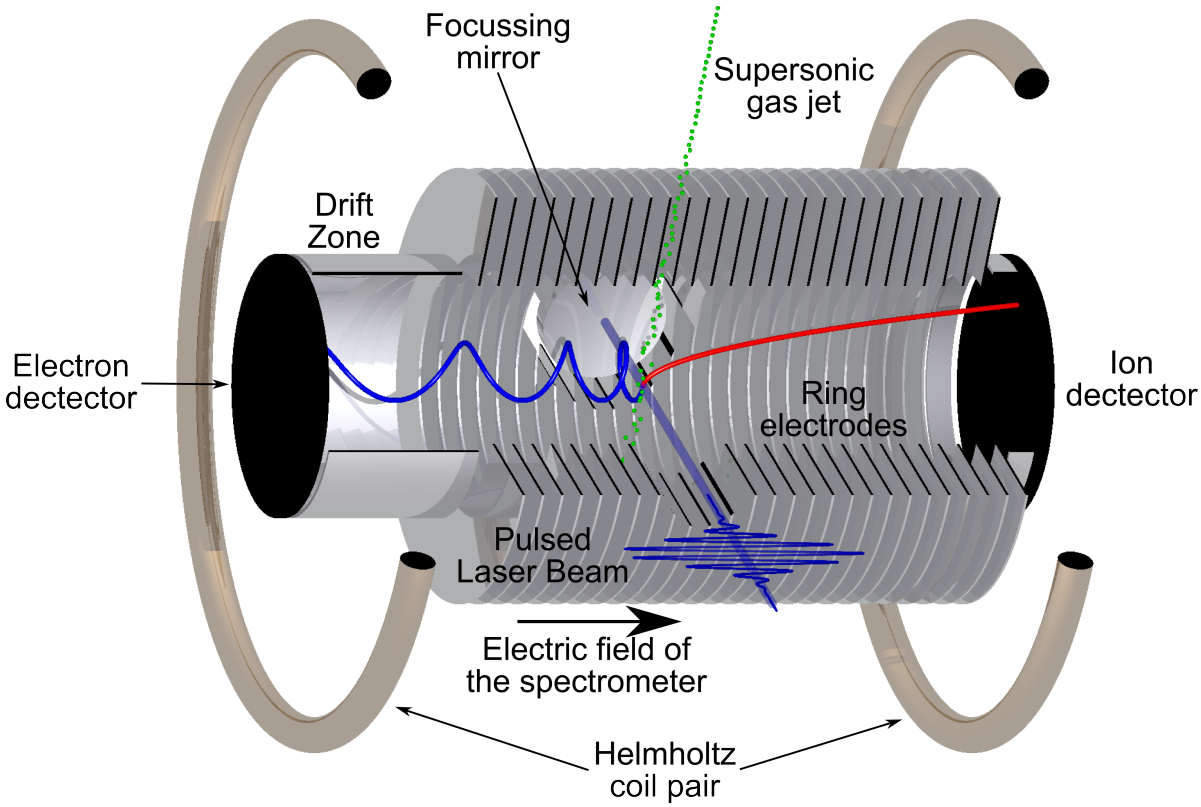

Figure 5.10.: Setup of a COLTRIMS apparatus. See text for explanation.

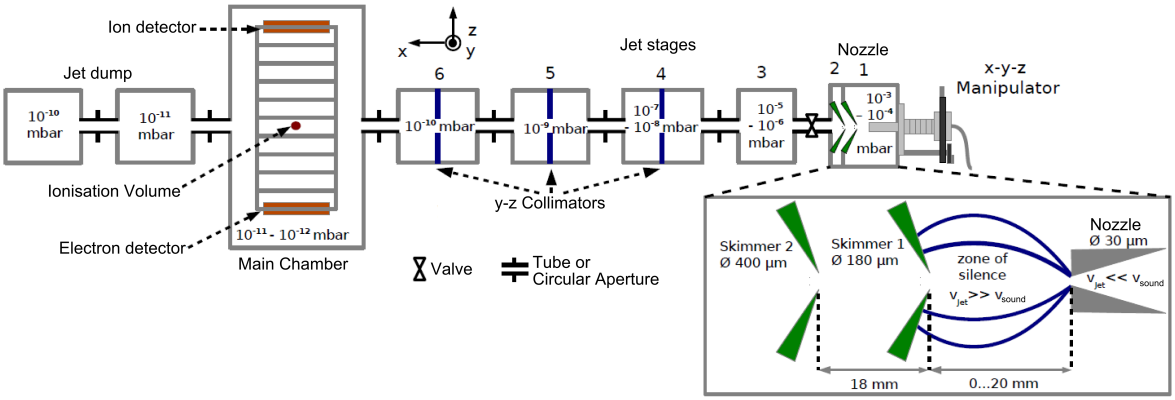

Figure 5.11.: Scheme of the complete vacuum chamber.[1] See text for explanation.

5.3.1. Supersonic jet expansion

Supersonic jet expansion is a method to create a cold, diffusive atomic/molecular beam. Due to its narrow velocity distribution with low mean value it is well suited for preparing

[1] Nicolas Camus. Komponenten eines Reaktionsmikorskops. Taken from an Open-House-Event Poster. Max-Planck-Institut für Kernphysik, Heidelberg.

gas atoms/molecules for spectroscopic experiments. As soon as the thermal velocity spread gets in the order of the momenta that are transferred during ionization processes ($\approx$ 1au), the results cannot give any insights in the underlying ionization mechanism anymore. For this reason a cold gas jet is essential. Fig. 5.12 shows a nozzle with a very small orifice that separates a high pressure reservoir from a low pressure vacuum chamber. If the pressure ratio is large enough the molecules will leave the orifice at velocities higher than the speed of sound. While the kinetic energy increases drastically its internal energy - or temperature - decreases at the same time. The cold expanding gas hits the hot background gas on the vacuum site and a shock wave forms. An easy

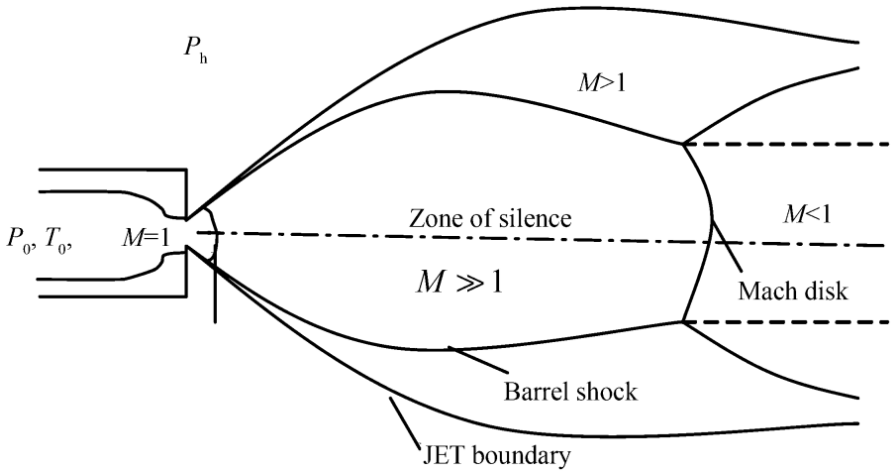

Figure 5.12.: Structure of a cold supersonic gas jet. Figure taken from [73].

thermodynamic analysis of the expansion process assumes an ideal gas and neglects viscous and heat conduction effects (Scoles *et al.* [74, pp. 16-18]). The first law of thermodynamics is the energy equation, which reads

$$h + V^2/2 = h_0 \,,$$

where h, V and h_0 are the enthalpy per unit mass, the flow velocity and the total enthalpy per unit mass, which is constant along any streamline. In the following the index 0 always indicates physical quantities of the gas reservoir whereas the symbols without index describe the situation in the low pressure region. Since for ideal gases $dh = c_p dT$ (c_p: molar heat capacity at constant pressure) the velocity relates to the jet

temperature as follows.

$$V^2 = 2(h_0 - h) = 2\int_T^{T_0} c_p dT\,.$$

Under the assumption that c_p is independent of the temperature we get $V = \sqrt{2c_p(T_0 - T)}$. An ideal gas has the heat capacity $c_p = \frac{\gamma}{\gamma-1}\frac{R}{W}$. Its speed of sound is $a = \sqrt{\gamma RT/W}$ and γ describes the adiabatic index. With the so-called Mach-Number $M = V/a$ one finds

$$T/T_0 = \left(1 + \frac{\gamma-1}{2}M^2\right)^{-1},$$
$$V = M\sqrt{\gamma RT_0/W}\left(1 + \frac{\gamma-1}{2}M^2\right)^{-1/2}.$$

If the expansion happens isentropically then

$$(p/p_0) = (T/T_0)^{\gamma/(\gamma-1)} = \left(1 + \frac{\gamma-1}{2}M^2\right)^{\gamma/(\gamma-1)},$$
$$(\rho/\rho_0) = (T/T_0)^{1/(\gamma-1)} = \left(1 + \frac{\gamma-1}{2}M^2\right)^{1/(\gamma-1)}.$$

It gets clear, that the temperature of the expanding gas decreases rapidly with decreasing Mach-number and thus increasing flow velocity. So in the zone of silence ($M >> 1$) the gas jet is extremely cold. For this reason a skimmer is placed right into this zone in order to extract the cold jet region. The Mach-number can only grow smaller than 1 if the pressure ratio p_0/p exceeds a critical value $((\gamma+1)/2)^{\gamma/(\gamma-1)}$, which is 2.1 for all gases.

The supersonic gas jet expansion creates a narrow velocity distribution with high mean value along the jet propagation direction. In the directions perpendicular to the propagation the velocity spreads with a mean value of 0 are even smaller due to the geometrical situation in the vacuum chamber. All the collimators in the 3m long jet line (see fig. 5.11) only allow gas molecules with very small perpendicular velocity components to pass through to the main chamber.

For a more detailed description of supersonic jets please see Morse [75] and Scoles *et al.* [74].

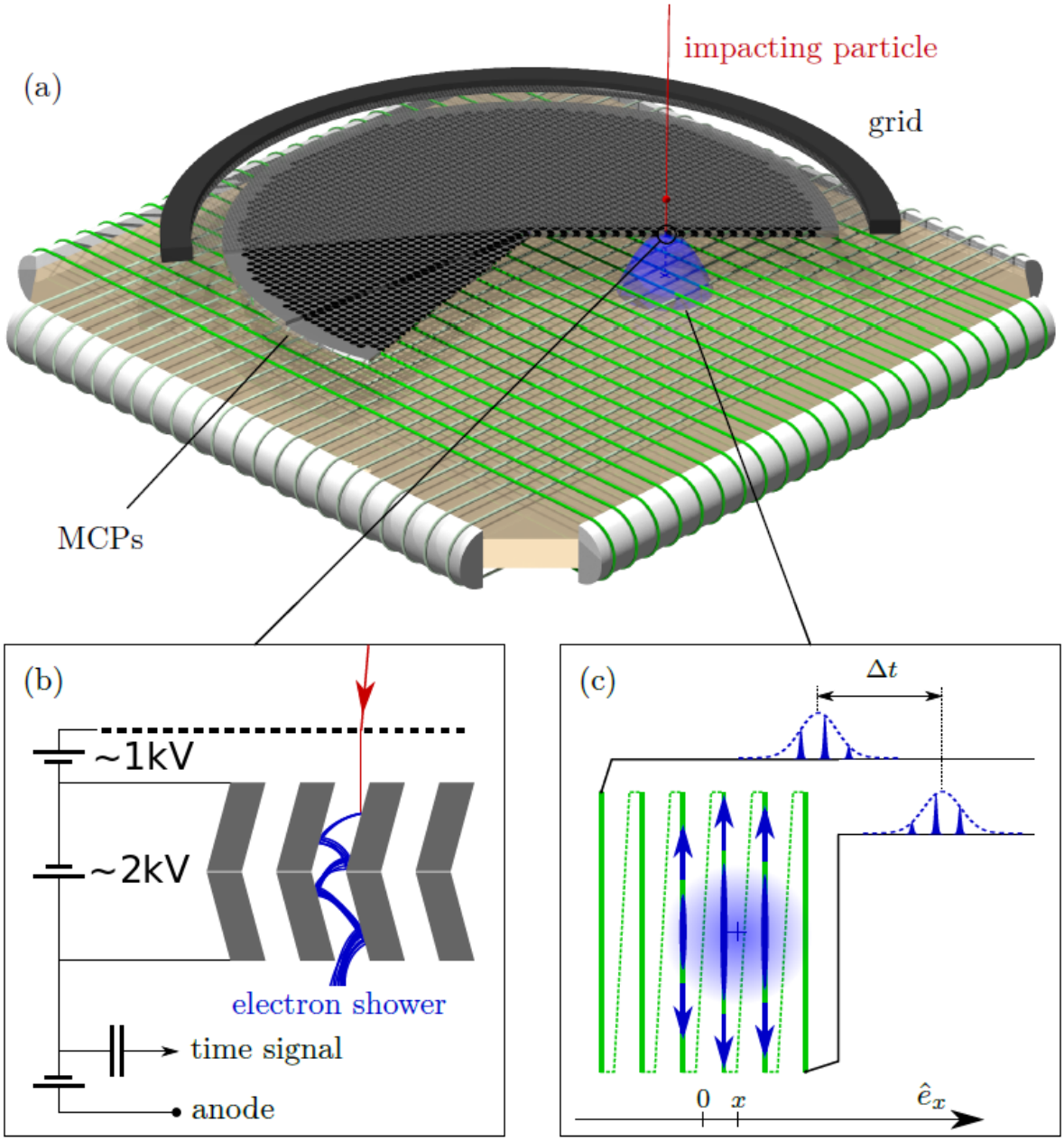

Figure 5.13.: Detector stack: Two MCPs in Chevron configuration and delay-line anode. (a) 3d scheme of the entire detector setup. (b) Overview over the electrical connections and voltages inside the detector. (c) Position detection principle of a delay-line. An electron impinges on an area of the wound delay-line which creates a voltage pulse that propagates from its point of origin towards the two ends of the cable. The difference of the two time signals is proportional to the wire position at which the electron cloud impinged. Figure taken and adapted from Fechner [76].

5.3.2. Time and position sensitive detectors

The detectors consist of a grid, two Micro-channel-plates (MCPs) and a delay-line-anode (5.13 (a)). At first the particle passes a grid, which shields the spectrometer's electric field from the high voltages applied to the detector. For the ion detector a voltage of 1kV is applied between the grid and the first MCP. Otherwise the ions would not gain sufficient kinetic energy for detection. In the following the ion/electron hits the first MCP. Between the front and the back MCP a voltage of ∼2kV is applied (5.13 (b)). Charged particles impinging on an MCP hit the tube wall due to its tilting angle. The tube walls are covered with a semiconductor material. Thus, if the energy of the impinging particle is sufficiently high, it will produce a cascade of electrons at the tube wall. It propagates to the opposite wall where the cascade is amplified and so on. After multiple amplification steps the produced electron cloud is released at the back of the MCP. Combining two MCPs like shown in figure (b) roughly squares the amplification compared to a single MCP. By rotating the MCPs around 180° with respect to each other backscattering of electrons is significantly reduced and thus the gain is increased. The time of flight is aquired by coupling out the short pulsed current signal via a capacitor.

Electrons that have been amplified by the MCP stack hit the delay line anode (5.13 (c)). This device is made of two wires that are each wound to form a wire carpet. Fig. (c) shows only one of these wires. An electron cloud arriving at a distinct position induces a current signal that propagates to both ends of the wire. From the difference of the measured times, that both signals need to get to the ends, it is possible to deduce the exact position of origin. The two delay-line-anodes are rotated by an angle of 90° with respect to each other for detection of every cartesian coordinate in the 2D detection plane. If two or more events take place at the same time how can you know which signal belongs to which event? Since the path of two opposite time signals always equals the wire length, also the time sum is a constant. The aquisition hardware tries out every possible combination of time signal doubles and calculates their sum until it finds the combination where the sums of all double events are approximately the same. Of course this analysis gets more complex the more events hit the detector per laser shot and there is only a limited time after the next shot has to be analyzed. This allows us to detect at maximum 3 events per shot.

5.3.3. Data acquisition and momentum reconstruction

Overall each detector delivers a ToF-signal and four delay-line timing signals (two for each of the spatial coordinates x,y). These signals as well as a trigger pulse from the femtosecond laser is acquired with a fADC-unit by Roentdek that contains two analog-to-digital converters (ADCs) to sample the timing signals [77].

For simplicity we choose a cylindrical coordinate system to describe the 3-d momentum vectors. The longitudinal and transversal components $p_{\parallel}, p_{\perp}$ describe the momenta along the spectrometer axis and perpendicular to it. ϕ is the angle between the laser propagation and the transversal momentum component of the emitted particle (fig. 5.14).

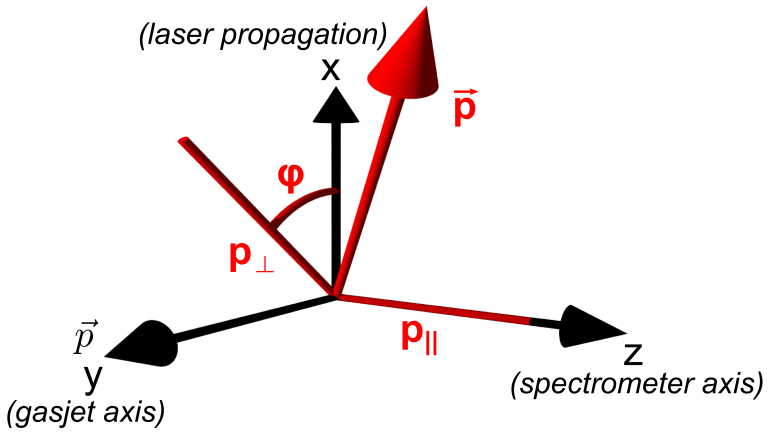

Figure 5.14.: Coordinate system used for momentum reconstruction

The trajectories of the charged particles are essentially given by the Lorentz force:

$$\dot{\mathbf{p}} = \mathbf{F}_L = \mathbf{F}_E + \mathbf{F}_B = q\mathbf{E} + q\mathbf{v} \times \mathbf{B}$$

The homogeneous electric field forces the charged particles on a parabola towards the detector and the homogeneous magnetic field causes a circular motion in the x-y-plane (fig. 5.10).

Longitundinal component

For the longitudinal component the magnetic field is irrelevant since the longitudinal velocity is always perpendicular to the magnetic field and thus $\mathbf{F}_{B,\perp} = \mathbf{v}_\perp \times \mathbf{B} = 0$.

Using Newton's second law of motion leads to:

$$\begin{aligned} x_{\parallel} &= \frac{1}{2}\frac{q}{m}Et^2 + \frac{p_{0,\parallel}}{m}t + x_{0,\parallel} \\ \Rightarrow p_{0,\parallel} &= m\frac{x_{\parallel} - x_{0,\parallel}}{t} - \frac{1}{2}qEt \end{aligned} \tag{5.4}$$

and

$$t = \begin{cases} \dfrac{m}{p_{0,\parallel}}\left(x_{\parallel} - x_{0,\parallel}\right) & \text{if} E = 0 \\ \sqrt{\left(\dfrac{p_{0,\parallel}}{qE}\right)^2 + \dfrac{2m}{qE}\left(x_{\parallel} - x_{0,\parallel}\right)} - \dfrac{p_{0,\parallel}}{qE} & \text{if } E \neq 0 \end{cases} \tag{5.5}$$

where t is the time of flight that the particle needs to cover a distance $x_{\parallel}$. As can be seen from the above equation, the time of flight of particles with zero initial longitudinal momentum depends exclusively on the charge to mass ratio. Therefore the time of flight peaks of different ion species with same charge to mass ratios will be superimposed.

In case of ions there is no drift region. Eq. (5.4) can be directly used to reconstruct the longitudinal momentum

$$p_{i,0,\parallel} = m_i\frac{a_i}{t_i} - \frac{1}{2}qEt_i\,,$$

with a_i and t_i describing the acceleration length and the time of flight of the ion.

In case of electrons there is a drift region that has to be taken into account in the reconstruction. The total time of flight is the sum of both times in the acceleration and drift region. Eq. (5.5) can be used to calculate each time of flight

$$\begin{aligned} t_e &= t_{e,d} + t_{e,a} \\ &= \frac{m_e}{eEt_{e,a} + p_{e,0,\parallel}}d + t_{e,a} \quad \text{with} \quad t_{e,a} = \sqrt{\left(\frac{p_{e,0,\parallel}}{eE}\right)^2 + \frac{2m_e}{eE}a} - \frac{p_{e,0,\parallel}}{eE}\,. \end{aligned} \tag{5.6}$$

It can be shown (see appendix sec. A.1) that the above equation is equivalent to

$$t_e = m\left(\frac{2a}{\sqrt{p_{e,0,\parallel}^2 + 2meU} + p_{e,0,\parallel}} + \frac{d}{\sqrt{p_{e,0,\parallel}^2 + 2meU}}\right)\,, \tag{5.7}$$

where U is the extraction voltage that is applied across the acceleration region. Since there is no analytic solution, the equation above is solved numerically using Newton's method.

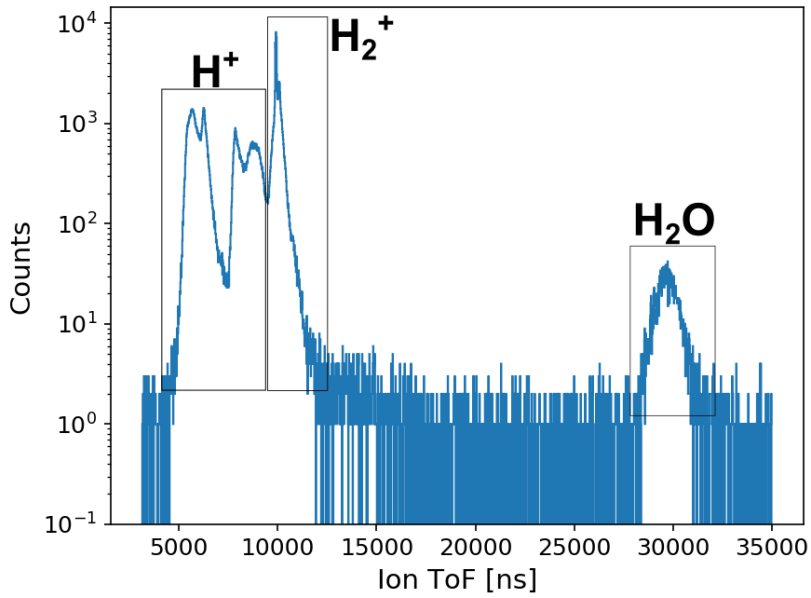

Figure 5.15.: Measured ion ToF t_i^{meas}. The H^+ signal is made up of four peaks. The two outer ones can be attributed to interprotonic repulsion (Coulomb explosion) in double ionization of H_2, which leads to high ion momenta.

Fig. 5.15 and 5.16 show how the data is calibrated to get the correct parameters for the reconstruction of the ion and electron longitudinal momenta. First the measured ion ToF is adjusted. Since the electronics of the acquisition hardware introduces a certain time delay $t_{0,i}$ the measured ToF relates to the real ToF like $t_i^{meas} = t_i + t_{0,i}$ where $t_i = a_i\sqrt{\frac{2}{U_i}}\sqrt{\frac{m_i}{q_i}}$ describes the real ion ToF. From the construction geometry of the spectrometer $a_i = 30$ cm is given. By fitting a function $t_i^{meas} = A\sqrt{\frac{m_i}{q_i}} + t_{0,i}$ to at least three well-known ToF-Peaks it is possible to determine a first guess for the acceleration voltage parameter U_i and the time delay offset $t_{0,i}$. In the case of H_2 the three ToF-Peaks are H^+, H_2^+ and H_20. The latter comes from ionization of water molecules from the background gas. Since the H^+-Peak is extremely broad with an expansive structure the lowest valley ToF-point was taken. The electron acceleration voltage is calculated via $U_e = \frac{a_e}{a_i}U_i$ where $a_e = 10$ cm is well-known.

In a next step the U_i-value and the time delay offset for the electron ToF is corrected slightly until the PePiCo-plot for H_2^+ and one electron satisfies the important momentum constraint $p_{i,0,\parallel}+p_{e,0,\parallel} = 0$ as good as possible. The Full-Width-Half-Maximum (FWHM) of the conservation line in fig. 5.16b gives a measure for the resolution of the coincidence precision.

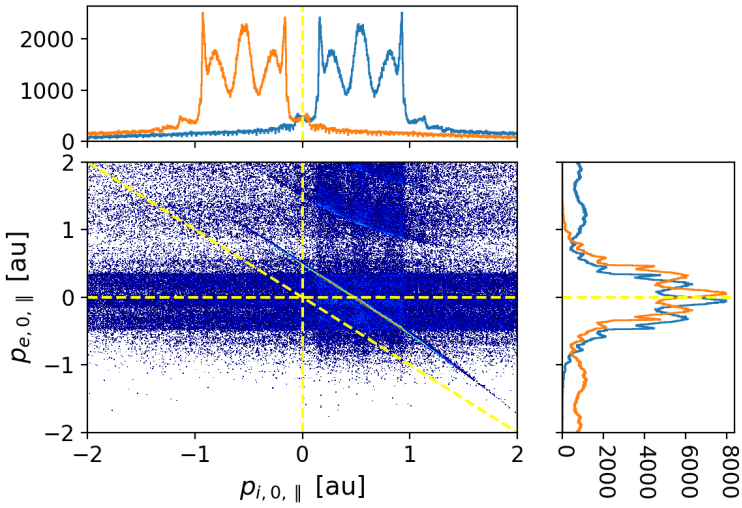

(a) PePiCo-plot using the parameters from the ion ToF fit like explained in the text.

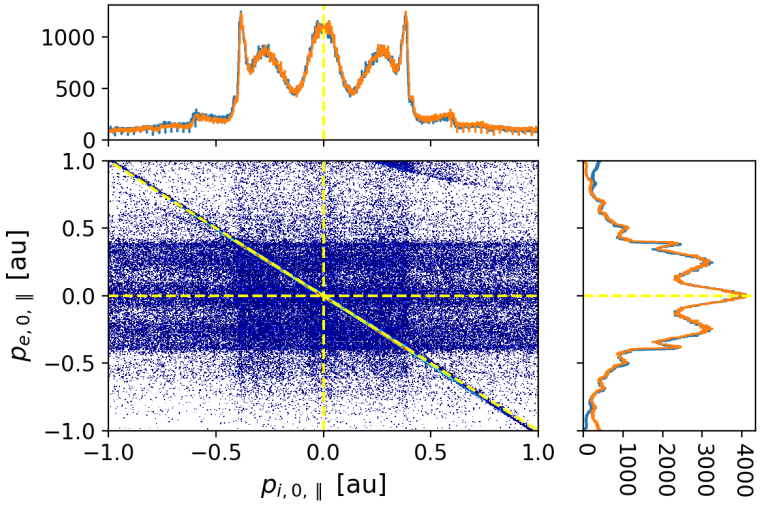

(b) PePiCo-plot after slight correction of the ion acceleration voltage and electron time delay offset parameters.

Figure 5.16.: Calibration procedure for the longitudinal momentum components. The goal is to find the right reconstruction parameters, such that the ion and electron momentum distributions are centered around zero and momentum conservation is fulfilled as good as possible. For reasons of better visualization the one dimensional projection plots show the original distribution in blue. The orange curve is blue one mirrored around zero.

Transversal component

In order to calculate the transversal momentum component the time of flight and the two position coordinates are necessary. Fig. 5.17 helps to understand the geometrical relations. $\omega = \frac{qB}{m}$ is the cyclotron frequency, r is the distance of the detection spot to the center of the detector and R is the radius of the cyclotron motion. R is proportional

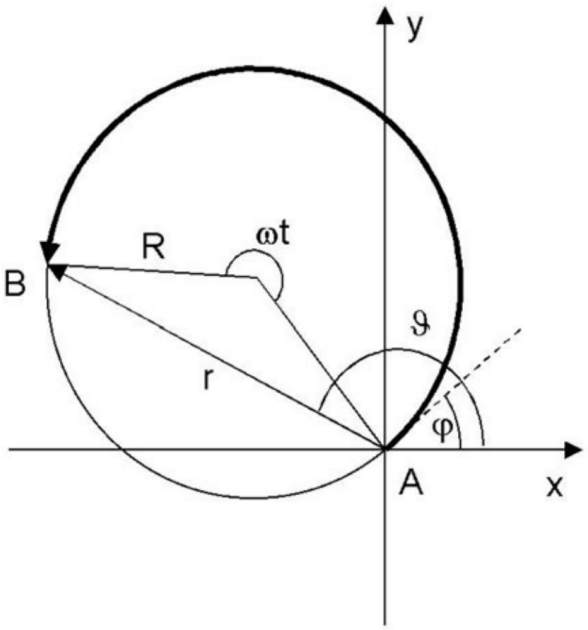

Figure 5.17.: Circular trajectory of a charged particle in the ReMi in the x-y-plane perpendicular to spectrometer axis [78, p. 1476]. The particle starts in point A and is emitted under the angle φ. It hits the detector at point B under the angle ϑ.

to the initial transversal momentum. From fig. 5.17 one can find

$$\begin{aligned} R &= \frac{v_{0,\perp}}{\omega} \\ &= \frac{p_{0,\perp}}{qB} \\ &= \frac{r}{2|\sin(\omega t/2)|} \end{aligned} \tag{5.8}$$

For the initial emission angle φ the following relation holds:

$$\varphi = \vartheta - (\frac{\omega t}{2} \mathrm{mod} \pi)$$

If the particle takes more than one full turn, then the angle of revolution has to be mapped back to the $(-\pi,\pi)$-interval.

Since the magnetic field is not perfectly homogeneous the electron positions are slightly corrected. Fig. 5.18 shows plots of the X-/Y-coordinates vs. the electron ToF. the redish blops are the nodes of the magnetic cyclotron motion and appear after the electron has completed one or multiple full cyclotron turns and returns to its origin. Ideally these nodes should come to rest exactly at x=0 and y=0. Since this is not the case a square function is added to each electron coordinate individually:

$$x_{corr} = x_{meas} + a_x t_{el}^2 + b_x t_{el} + c_x$$
$$y_{corr} = y_{meas} + a_y t_{el}^2 + b_y t_{el} + c_y$$

The function coefficients $a_{x,y}, b_{x,y}, c_{x,y}$ can be found by fitting the above square functions to the measured node points.

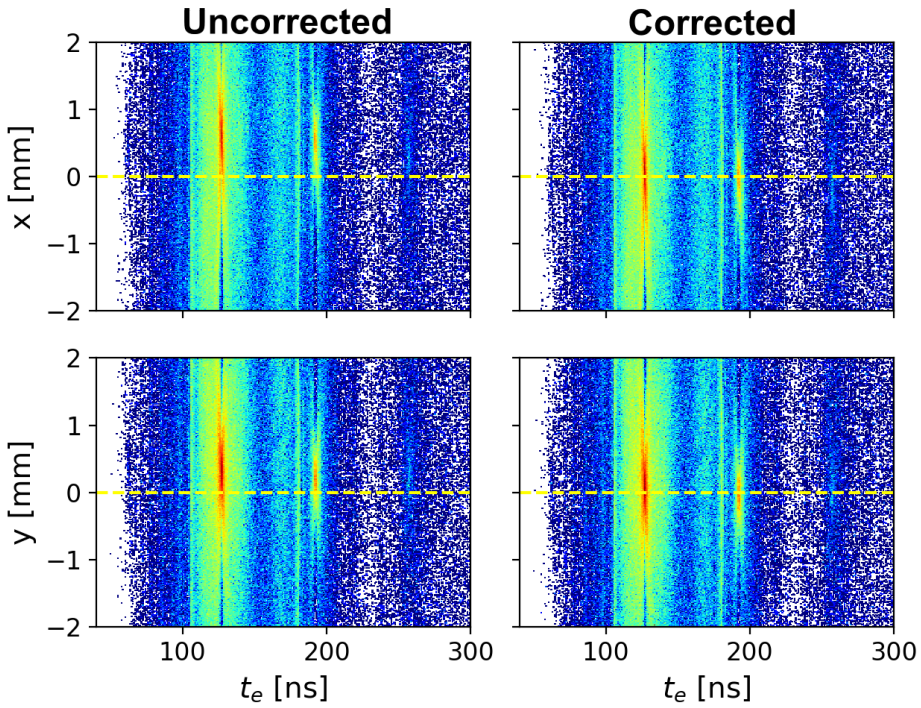

Figure 5.18.: In order to account for inhomogeneities in the magnetic field, the measured electron coordinates are corrected by adding a ToF-dependent square function as described in the text.

For a more detailed description of COLTRIMS please see [78, 79].

5.3.4. Momentum coincident events

The big advantage of the ReMi is the fact, that the information of the full 3d momentum vectors of all charged particles can be used to determine to which channel an event belongs.

Bound ionization

Bound Ionization means that the H_2 molecule breaks up in an H_2^+ cation and a free electron.

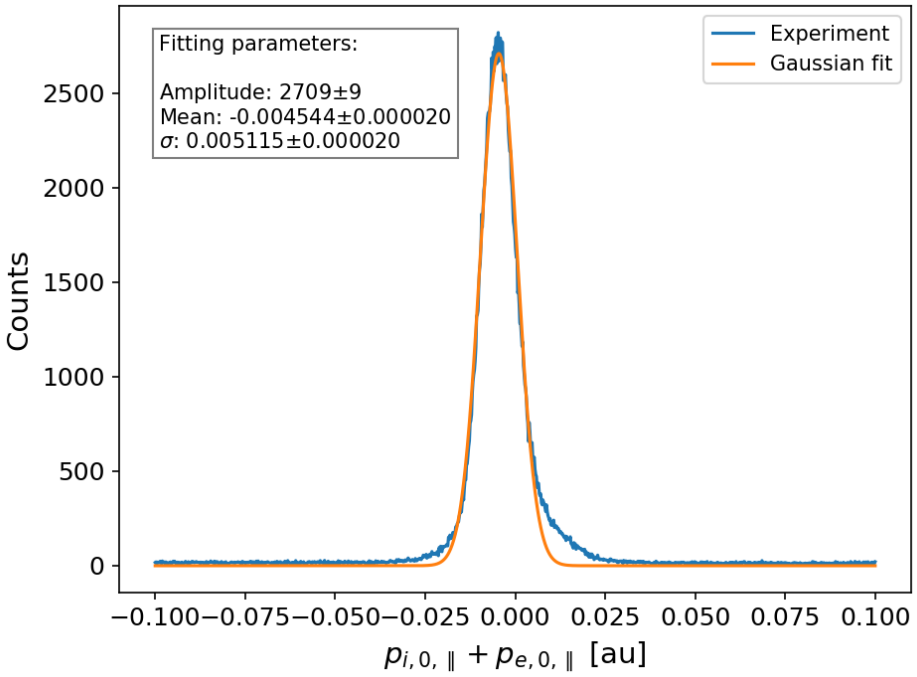

Figure 5.19.: Momentum sum for H_2^+ ion and electron from bound ionization. All events around zero (±0.025au tolerance) are believed to be bound ionization events.

The resolution of the longitudinal momentum component is given as the FWHM of the momentum sum distribution in fig. 5.19, which is $\Delta p_{\parallel} = 2\sqrt{\ln(2)}\sigma = 0.012$au for a Gaussian fit. This number quantifies the precision of the measured longitudinal momenta. Let's compare this number to the momentum of a photon with energy $E = pc$. Then it gets clear that the momenta of the absorbed photons are insignificant up until photon energies of 1.6au=43.5eV. This is beyond the photon energies that get absorbed in the experiments of this thesis. For this reason the photon momenta can be neglected

when checking for momentum conservation between the ionization fragments.

The same calculation for the x- and y-momentum-components delivers $\Delta p_x = 0.017$au and $\Delta p_y = 0.342$au. The y-component is far more unprecise because it's the direction of the gas jet and in this direction the gas target has a broader velocity distribution (see sec. 5.3.1 for explanation).

Double ionization

Double Ionization ($H_2 \rightarrow 2H^+ + 2e^-$) involves four charged particles. The coincidence involves all four particles and the resolution on the momentum sums are $\Delta p_{\parallel} = 0.03$au, $\Delta p_x = 0.68$au and $\Delta p_y = 0.71$au.

Dissociative ionization

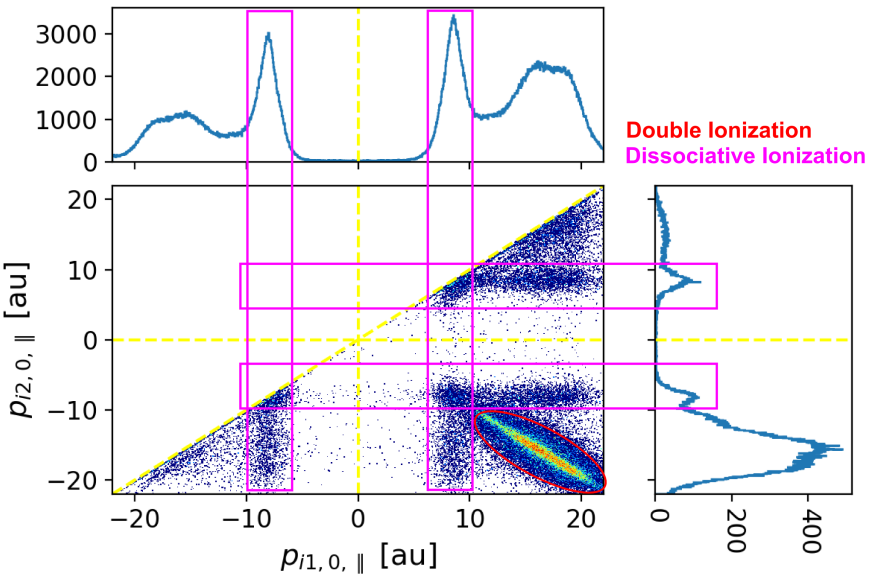

Figure 5.20.: Longitudinal momenta of first and second H^+ ion plotted as a 2d-histogram including the projections on each axis. The ion momenta of the red encircled events sum up to 0. These events are caused by two protons that repell each other after both electrons have been removed from the molecule. The electron momenta are rather small compared to the resulting ion momenta. That's why momentum conservation can be observed also without including the electrons.

Events that involve neutral fragments can not be assigned unequivocally to the correct ionization channel. In case of dissociative ionization ($H_2 \rightarrow H + H^+ + e^-$) additional information on the physical process have to be included to find out whether a molecule has undergone dissociation or not. The first necessary condition is, that only one proton and one electron are detected per laser shot. Furthermore only the two inner peaks of the H^+-ToF-signal hold the dissociation events (5.15 and 5.20). The two outer peaks are due to interprotonic repulsion that happens at comparatively small internuclear distances in double ionization, when both electrons are removed and only the two protons are left next to each other. This process is also known as Coulomb explosion.

5.4. Nuclear dynamics simulation

The task is to solve the nuclear Schrödinger equation as presented in eq. (2.12) by using the matrix representation in the basis of the stationary H_2^+ states (see eq. (2.13)). The time evolution of a quantum mechanical system is given by

$$|\Psi(x, t + t_0)\rangle = \exp(-iHt/\hbar)\,|\Psi(x, t_0)\rangle$$

The time evolution operator $\exp(-iHt/\hbar)$ can be defined via the power series of the exponential function. If X, Y are two steady linear operators, the Baker–Campbell–Hausdorff (BCH) formula states:

$$e^X e^Y = e^Z$$
$$\text{with } Z = X + Y + \frac{1}{2}[X, Y] + \frac{1}{12}([X, [X, Y]] + [Y, [Y, X]]) + \frac{1}{24}[Y, [X[X, Y]]] + \ldots$$

A recursive application of the above BCH relation leads to the so-called Zassenhaus formula:

$$e^{(X+Y)} = e^X e^Y e^{-1/2[X,Y]} e^{-1/6(2[y,[X,Y]]+[X,[X,Y]])} \ldots$$

Let's investigate the following expressions using this Zassenhaus formula. We introduce the abbreviations $X = -iV\Delta t/\hbar$ and $Y = -iT\Delta t/\hbar$ where the operators T and V

describe the kinetic energy and interaction potential of the system..

$$\begin{aligned} e^{Y/2+X+Y/2} =& e^{Y/2}e^{X+Y/2}e^{-\frac{1}{2}[Y/2,X]}e^{\mathrm{O}(\Delta t^3)} \\ \approx& e^{Y/2}e^{X}e^{Y/2}e^{-\frac{1}{2}[X,Y/2]}e^{\mathrm{O}(\Delta t^3)}e^{-\frac{1}{2}[Y/2,X]} \\ \approx& e^{Y/2}e^{X}e^{Y/2}e^{-\frac{1}{2}([X,Y/2]+[Y/2,X])+\mathrm{O}(\Delta t^4)} \end{aligned}$$

Using the BCH formula at last leads to

$$e^{Y/2+X+Y/2} \approx e^{Y/2}e^{X}e^{Y/2}$$

So the symmetric splitting $e^{Y/2}e^{X}e^{Y/2}$ is accurate to third order $O(t^3)$ in time. An analog calculation for $e^{X}e^{Y}$ shows, that it is only second order $O(t^2)$ accurate.

The above equations states, that applying first the operator $e^{-iT\Delta t/(2\hbar)}$, then $e^{-iV\Delta t/\hbar}$ and finally again $e^{-iT\Delta t/(2\hbar)}$ is a good approximation to the time evolution operator $\exp(-iHt/\hbar)$. This operator series however is only computationally efficient to perform if $e^{-iT\Delta t/(2\hbar)}$ and $e^{-iV\Delta t/\hbar}$ are always applied to a state whose matrix representation has a diagonal form. As a reminder eq. (2.13) reads

$$\mathrm{i}\hbar\frac{\partial}{\partial t}\begin{pmatrix}\Psi_1(\mathbf{R},t)\\ \Psi_2(\mathbf{R},t)\\ \vdots \\ \Psi_n(\mathbf{R},t)\end{pmatrix} = (T+V+H_{int})\begin{pmatrix}\Psi_1(\mathbf{R},t)\\ \Psi_2(\mathbf{R},t)\\ \vdots \\ \Psi_n(\mathbf{R},t)\end{pmatrix} \tag{5.9}$$

with

$$T = -\frac{p^2}{2\mu}1, \quad V = \mathrm{diag}(V_1, V_2, \cdots), \quad D = \begin{pmatrix} 0 & D_{12} & \cdots & D_{1n} \\ D_{21} & 0 & \cdots & D_{2n} \\ \vdots & \vdots & \ddots & \vdots \\ D_{n1} & D_{n2} & \cdots & 0 \end{pmatrix},$$

Since H_{int} is not diagonal a unitary transformation U has to be applied

$$T+V+H_{int} = T + U^\dagger \underbrace{U(V+H_{int})U^\dagger}_{V_{int}} U\,,$$

such that V_{int} is of the form $V_{int} = \mathrm{diag}(V_{int,1}, V_{int,2}, \cdots)$ in the basis of the position space states $|x\rangle$ and its vector representation is $\Psi(\mathbf{R},t) = (\Psi_1(\mathbf{R},t), \Psi_2(\mathbf{R},t), \cdots, \Psi_n(\mathbf{R},t))$. $\Psi(\mathbf{R},t)$ is not an eigenvector of T but the Fourier-transformed vector representation

$\tilde{\Psi}(\mathbf{p},t) = \mathcal{F}\left(\Psi(\mathbf{R},t)\right)$ in the basis of momentum space $|p\rangle$ is.

Here is an overview over the complete algorithm scheme to propagate the wavefunction over a timestep Δt as it is implemented:

1. Setup the initial wavefunction in position space $\Psi(\mathbf{R},t) = \Psi_0(\mathbf{R},t)$
2. Fourier transformation $\tilde{\Psi}(\mathbf{p},t) = \mathcal{F}\left(\Psi(\mathbf{R},t)\right)$
3. Propagate $\tilde{\Psi}(\mathbf{p},t) \to e^{-iT\Delta t/(2\hbar)}\tilde{\Psi}(\mathbf{p},t)$ in momentum space
4. Inverse Fourier transformation $\Psi(\mathbf{R},t) = \mathcal{F}^{-1}\left(\tilde{\Psi}(\mathbf{p},t)\right)$
5. Find the unitary transformation U and calculate V_{int}
6. Transform $\Psi(\mathbf{R},t) \to U\Psi(\mathbf{R},t)$
7. Propagate $\Psi(\mathbf{R},t) \to e^{-iV_{int}\Delta t/\hbar}\Psi(\mathbf{R},t)$ in position space
8. Transform back $\Psi(\mathbf{R},t) \to U^{\dagger}\Psi(\mathbf{R},t)$
9. Fourier transformation $\tilde{\Psi}(\mathbf{p},t) = \mathcal{F}\left(\Psi(\mathbf{R},t)\right)$
10. Propagate $\tilde{\Psi}(\mathbf{p},t) \to e^{-iT\Delta t/(2\hbar)}\tilde{\Psi}(\mathbf{p},t)$ in momentum space

The steps 2-3 and 9-10 can be combined for successive time steps by directly propagating a full time step $\tilde{\Psi}(\mathbf{p},t) \to e^{-iT\Delta t/\hbar}\tilde{\Psi}(\mathbf{p},t)$ in order to reduce computational effort. This is of course not possible for the very first and very last time step of the simulation.

6. Results and Discussion

6.1. 400 nm single-pulse ionization

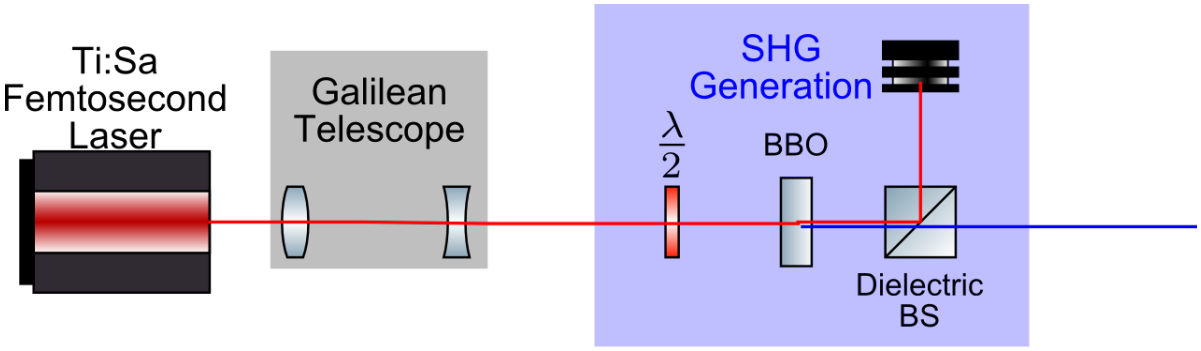

Figure 6.1.: Second Harmonic Generation (SHG) Setup

For these experiments the 800 nm laser pulses from the Femtolaser system (see sec. 5.1) were guided into a Second-Harmonic-Generation-Kit (see fig. 6.1). A Galilean Telescope reduces the original beam diameter of roughly 1 cm to 2 mm to fit and efficiently pump the nonlinear barium borate (BBO) crystal. After frequency doubling (sec. 2.1.1) a dielectric beam splitter reflects only the red light leaving through the 400 nm pulses, which are then focused into the ReMi (sec. 5.3). The $\lambda/2$-waveplate allows for adjustment of the right laser polarization in the ReMi. Several measurements with different laser intensities have been performed over a time period of several months.

6.1.1. Electron-nuclear correlation

Dissociation

Fig. 6.2 shows the Joint-Energy-Spectrum (JES) of the kinetic energy release (KER) vs. the electron energy for the dissociation channel. Here the kinetic energy release is approximated to be $2E_{H^+}$ since in the molecular center of mass system the nuclear kinetic energy is equally shared between proton and hydrogen atom. Isolated stripes

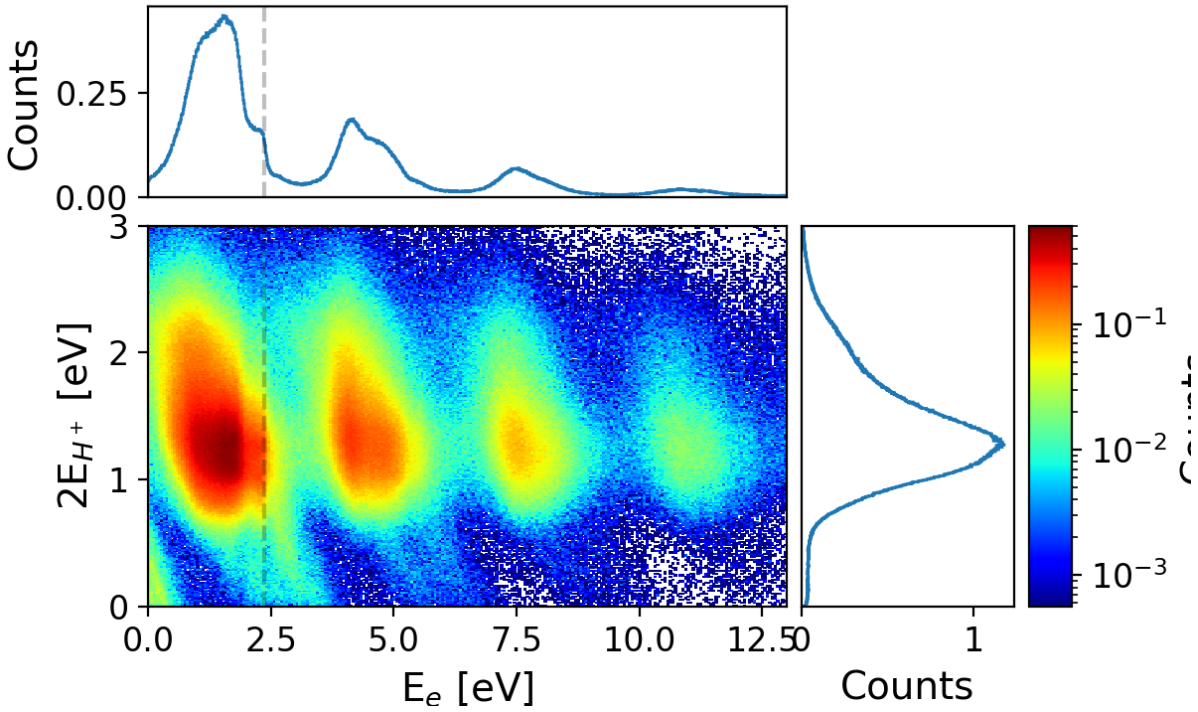

Figure 6.2.: JES of the dissociation pathway for a laser intensity of $8 \cdot 10^{13}$W/cm^2. The significance of the dashed black lines are explained in the course of this section on page 94.

show up. They are all spaced with the photon energy of roughly 3.1eV. The slope of the stripes is -1. This data reproduces well the findings by Wu *et al.* [66] that were already presented in fig. 4.5 for the case of linear polarization. The dissociation limit of molecular hydrogen is 18.08 eV according to Sharp [80, p. 125]. A photon with 400 nm central wavelength has an energy of 3.1 eV. So the minimum required photon number for dissociation is 6. Thus the first visible JES-signal at around 0 eV electron and nuclear kinetic energy corresponds to an absorption of 6 photons in total. Every further conservation line corresponds to one additional photon.

Double ionization

Also in Double Ionization the conservation lines are visible in the JES (fig. 6.3) as previously found by [68] in fig. 4.6. Since the double ionization energy of molecular hydrogen is 31.67 eV [80, p. 125] the first stripe with a total sum energy of $\Sigma E_e + \Sigma E_i \approx 3$ eV corresponds to an absorption of 11 photons in total.

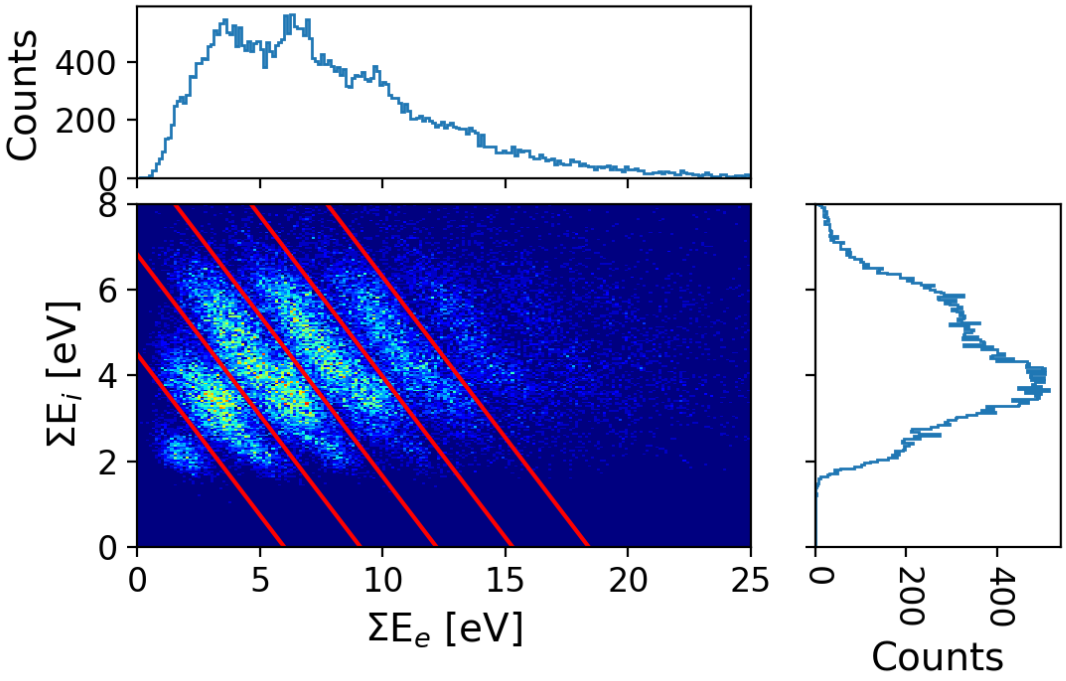

Figure 6.3.: JES of the double ionization events. Clear conservation lines with slope -1 show up. For better visibility the separation between those lines is marked in red. The one-dimensional projections show the distributions of sum kinetic energies of electrons and ions separately.

Fig. 6.4 shows the electron momentum distribution for each of the different conservation lines from fig. 6.3. These plots describe the photoelectron angular distribution (PAD) because the angle between an arbitrary point in the 2d-plot and the x-axis is precisely the angle between the ejected electron with respect to the laser polarization.

It gets clear that with every further absorbed photon an additional ring appears in the momentum distribution because it gets possible to reach the next ATI-peak. For each of these rings the number of angular peaks in the respective ring increases by one. This means that the maximum angular momentum of the ejected electrons increases by one (see sec. 3.5). Unfortunately the statistics of double ionization events is too low to retrieve highly resolved photon-number-selective momentum distributions from fig. 6.4.

In the case of dissociative ionization the number of electrons can be directly retrieved from the electron momentum distribution because every conservation line in fig. 6.2 can be clearly assigned to exactly one ATI-peak in the electron energy spectrum. This is not possible anymore for the double ionization channel in fig. 6.4. Therefore the JES

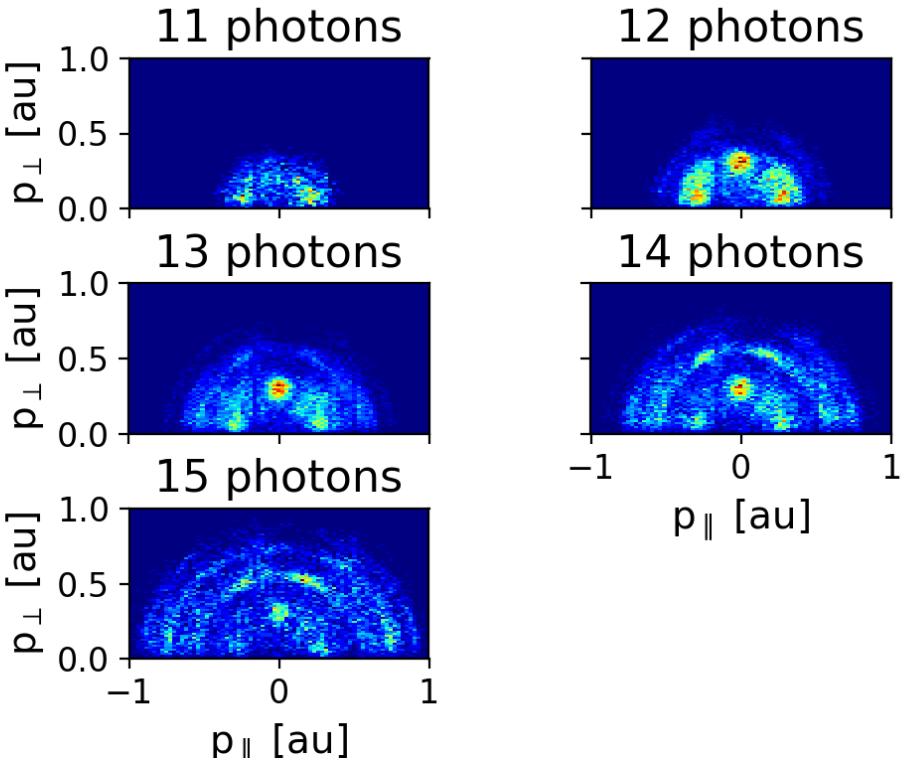

Figure 6.4.: Photon-number-selective electron momentum distributions for H_2 double ionization. The momentum components parallel and perpendicular to the laser polarization are shown.

is essential for recovering the number of absorbed photons. Moreover the COLTRIMS technique is the only method that allows photon-number-selective analysis of the ion and electron momentum distributions in double ionization because the coincident detection is crucial for the observation of conservation lines.

6.1.2. Singly-excited Rydberg states in bound and dissociative ionization

Fig. 6.5 shows the energy electron spectra for bound and dissociative ionization at 200Hz ion count rate. As described in sec. 4.1 the Two Step Mechanism implies that the quantum mechanical observables from the emitted electron in bound and dissociative ionization should be exactly the same, which is obviously not the case.

In order to understand where the difference comes from, we first try to explain the spectrum for bound ionization. Three clear peaks around 2 eV appear. These can also be seen at the next ATI peak at around 5.5 eV. The same observation was previously made

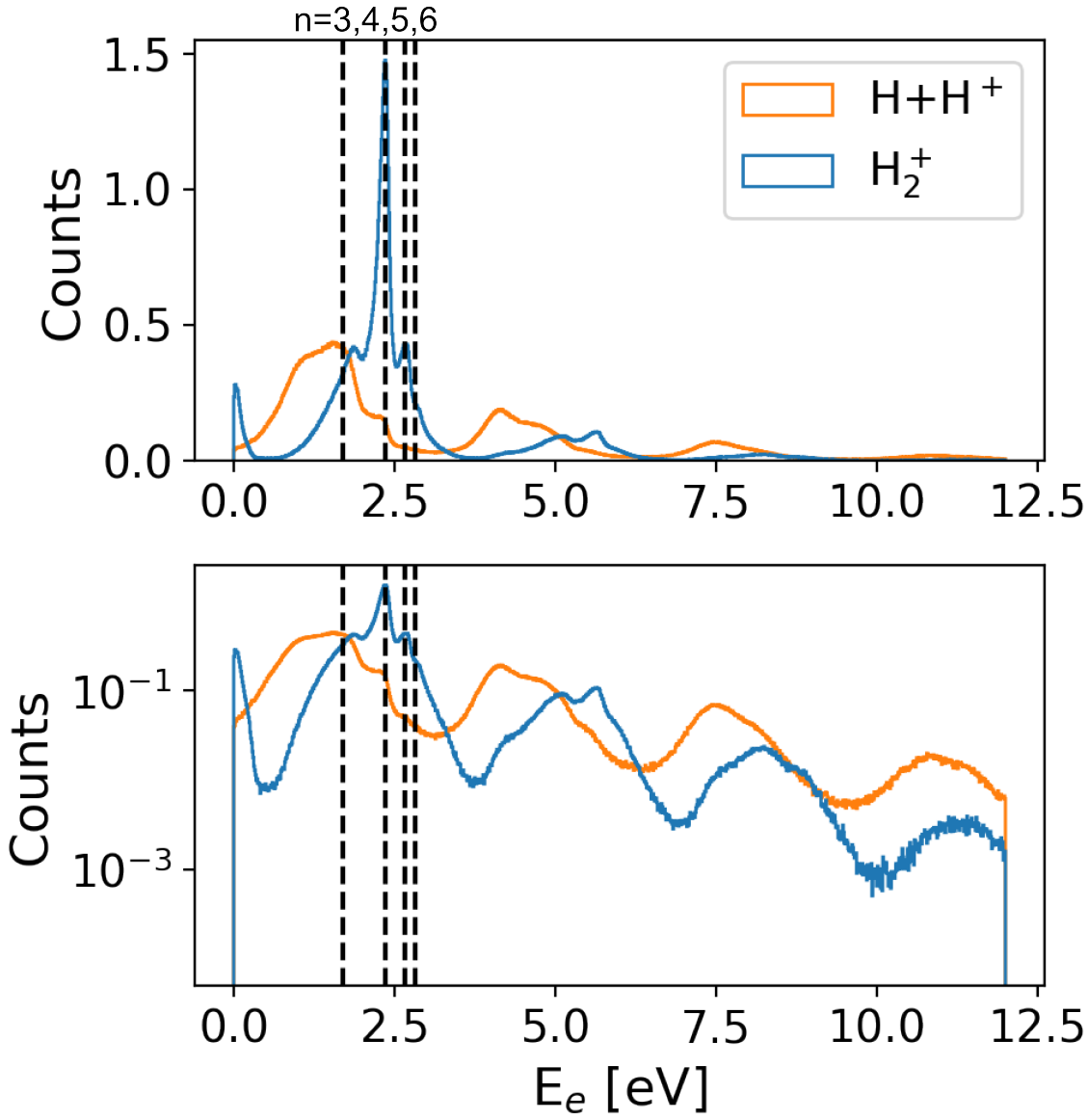

Figure 6.5.: Electron energy spectra of the bound and dissociative channels. The black dashed vertical lines indicate the hydrogenic Rydberg series for n=3,4,5,6. The bottom plot has a logarithmically scaled y-axis.

and explained by Schellhammer [12] (fig 6.6). At the intensity of $4.5 - 12 \times 10^{13}$ W/cm^2 there is a dominant resonance peak at 2.3 eV surrounded by two smaller ones at 2 and 2.5eV. According to Schellhammer the peaks at 2.3 and 2.5 eV fit exactly to the Rydberg series $\frac{R_y}{n^2}$ with $n = 4, 5$. Schellhammer [12] also gives a comprehensive explanation on the bound ionization mechanism that creates the above Rydberg peaks. The process starts from the neutral H_2 ground state. Via resonant absorption of 5 photons Rydberg

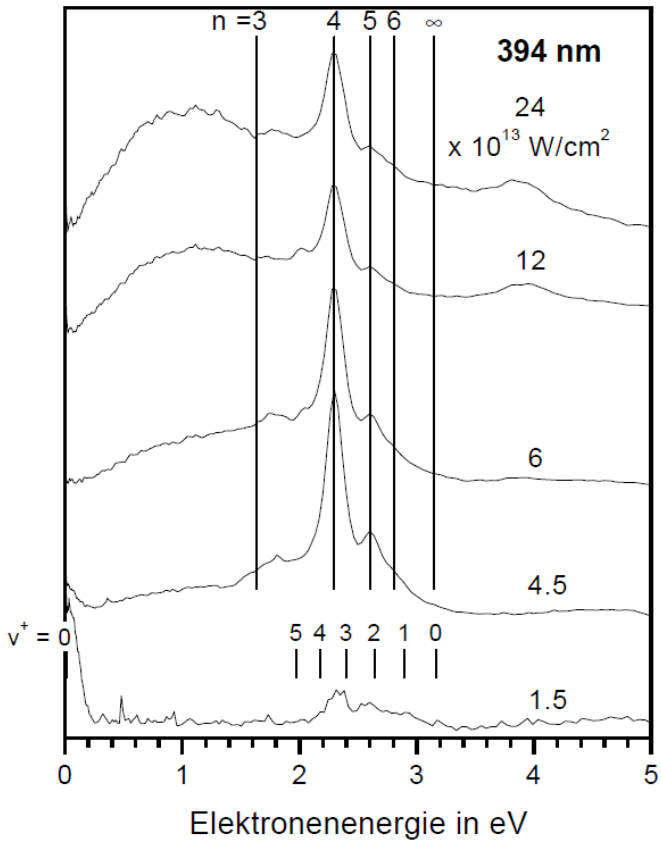

Figure 6.6.: Experiment, results and figure by Schellhammer [12]. Electron energy spectra of Bound Ionization of H_2 using 100fs linearly polarized pulses with 394nm central wavelength and different laser intensities. Electrons were imaged via Velocity Map Imaging. The Rydberg resonance peaks are identified as indicated by the vertical lines. At $1.5{\cdot}10^{13}$ W/cm^2 a contribution from vibrational states of the $H_2^+ 1s\sigma_g$ state ($v^+ = 0$) is visible.

states can be accessed. As fig. 6.7 shows, the potential energy curves of singly excited H_2 Rydberg states run almost parallel to the H_2^+ ground state curve. Thus the vibrational eigenenergies and eigenstates of the singly excited H_2 Rydberg states are almost identical to the ones of the $1s\sigma_g$ H_2^+ state. Let us consider an electronic transition from a Rydberg state to the $1s\sigma_g$ H_2^+ state. Due to the great similarity between the potential energy curves the Franck-Condon factors, that describe the overlap integral between vibrational wavefunctions of the initial and final electronic states, are biggest for transitions that do not change the vibrational quantum number. So the most probable transitions will leave the vibrational state and quantum number unchanged. Consequently the kinetic energy E_e of the emitted electron will essentially depend only on the principal quantum

number n of the singly excited Rydberg state and the photon energy E_γ:

$$E_e = E_\gamma - \frac{R_y}{n^2}$$

The entire process, as explained above, is known as resonant-enhanced multiphoton

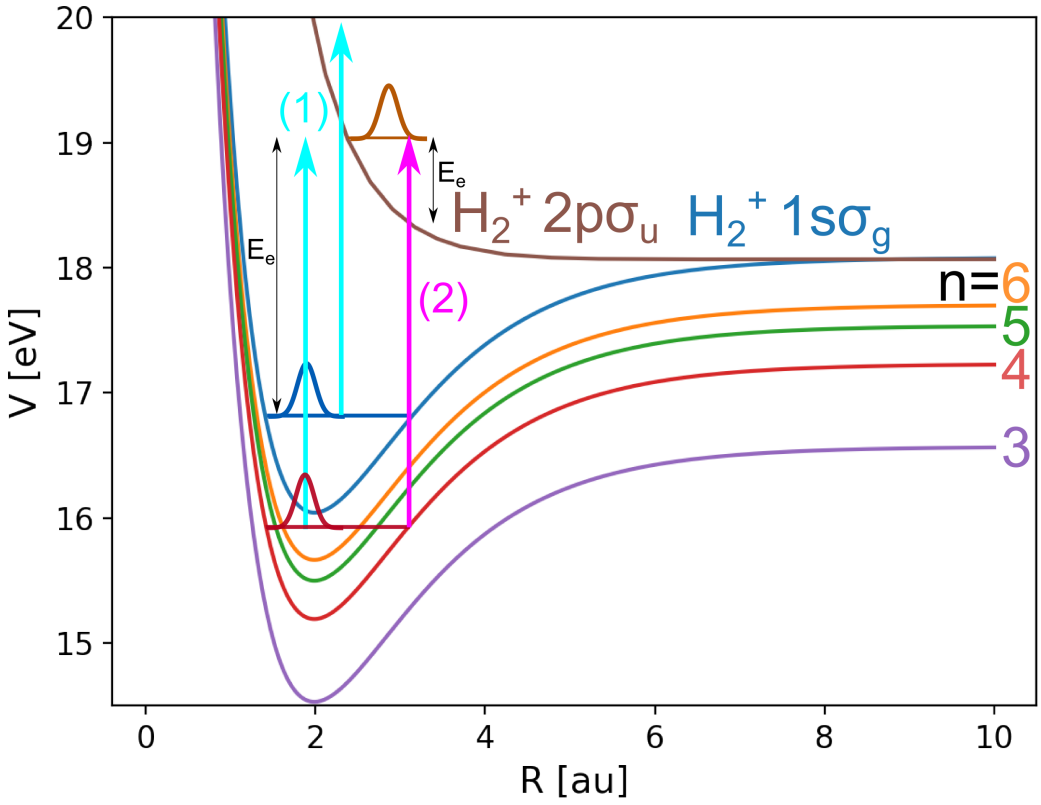

Figure 6.7.: Potential energy curves for the H_2^+ $1s\sigma_g$ ground state, the $2p\sigma_u$ curve and singly excited H_2 Rydberg states (n=3,4,5,6). The photon transitions are shown via arrows (light blue or pink) with an energy of 3.1 eV (400nm). There are two possible ionization pathways how to get from a Rydberg state (here n=4 for example) to the $2p\sigma_u$ curve. Path (1) uses the $1s\sigma_g$ state as an intermediate step, whereas path (2) does not involve an intermediate state. The first transition of path (1) happens most likely if the vibrational quantum number does not change $\Delta\nu = 0$ (see text for explanation).

ionization (REMPI) (see 3.3). First a resonant transition to a singly-excited Rydberg state takes place, followed by an ionization to the continuum. In fig. 6.5 the indicated Rydberg series fits good for the quantum numbers n=3,4,5,6. As a conclusion, also the singly excited H_2 Rydberg states have to be included when modeling bound ionization.

Fig. 6.8 shows the electron energy spectra of bound ionization events for different laser intensities. The data are in agreement with the experiments by Schellhammer [12] shown in fig. 6.6. The entire spectra shift for increasing laser intensity because the ponderomotive electron energy increases, which shifts the measured kinetic electron energy towards smaller values. The relative dominance of the n=4 peak compared to the overall spectrum is biggest for the orange spectrum ($I \approx 8 \cdot 10^3$ W/cm^2). At roughly this intensity resonance between the H_2 ground state and the n=4 Rydberg state is fulfilled best among all the measurements. Schellhammer [12, p. 58] plots the ponderomotive shift of the n=4 Rydberg state as a function of the laser intensity according to the relation $U_p = \frac{2e^2}{4c\varepsilon_0 m_e (hc)^2} I\lambda^2$. For a wavelength of 394 nm the 5-photon resonance between the H_2 vibrational ground state and the n=4 singly excited Rydberg state is fulfilled at approximately $8 \cdot 10^{13}$W/cm^2. This is the estimated intensity for the orange spectrum. The intensity of the blue curve is believed to be slightly below this value. This estimation fits to the experimental conditions as reported in the measurements by Wu *et al.* [66] and Lu *et al.* [68]. For all the other curves from fig. 6.8 the intensity values cannot be estimated accurately. However, the intensity order of the different measurements is inferred from the average ionization count rates during the performance of the measurements.

Schellhammer [12, sec. 5.3] discusses possible intermediate states in the process of bound ionization. His electron energy spectra for ionization with femtosecond pulses with a duration of 100 fs and central wavelengths of 389-405 nm clearly show evidence that bound ionization happens via a resonant 5-photon transition to the H_2^+ $1s\sigma_g$. Dominating contributions from this state are seen for laser intensities up to $1.5 \cdot 10^{13}$W/cm^2 at 394nm [12, pp. 59-60]. For higher intensities this channel closes due to the influence of the ponderomotive shift. The energy of five photons is no longer enough for exciting the H_2^+ ground state. Also the Rydberg peaks get weaker as the intensity increases because they are shifted out of resonance. Due to the fact that in this thesis the laser pulses are shorter than the ones used by Schellhammer [12], the vibrational states at low electron energies can not be resolved accurately. But clearly in this region there is a significant increase in electron counts that grows weaker for higher laser intensities.

Only the most prominant resonance for n=4 can also be seen in the dissociation channel (fig. 6.5). If we repeat the plot from fig 6.2 for different KER regions, it is possible to see the same Rydberg resonances as observed for bound ionization (see fig. 6.9). Due to the shape of the dissociative potential energy curve the electron energy resolution significantly increases for bigger internuclear distances or lower KER, respectively. This is why it should in principal be possible to observe the Rydberg

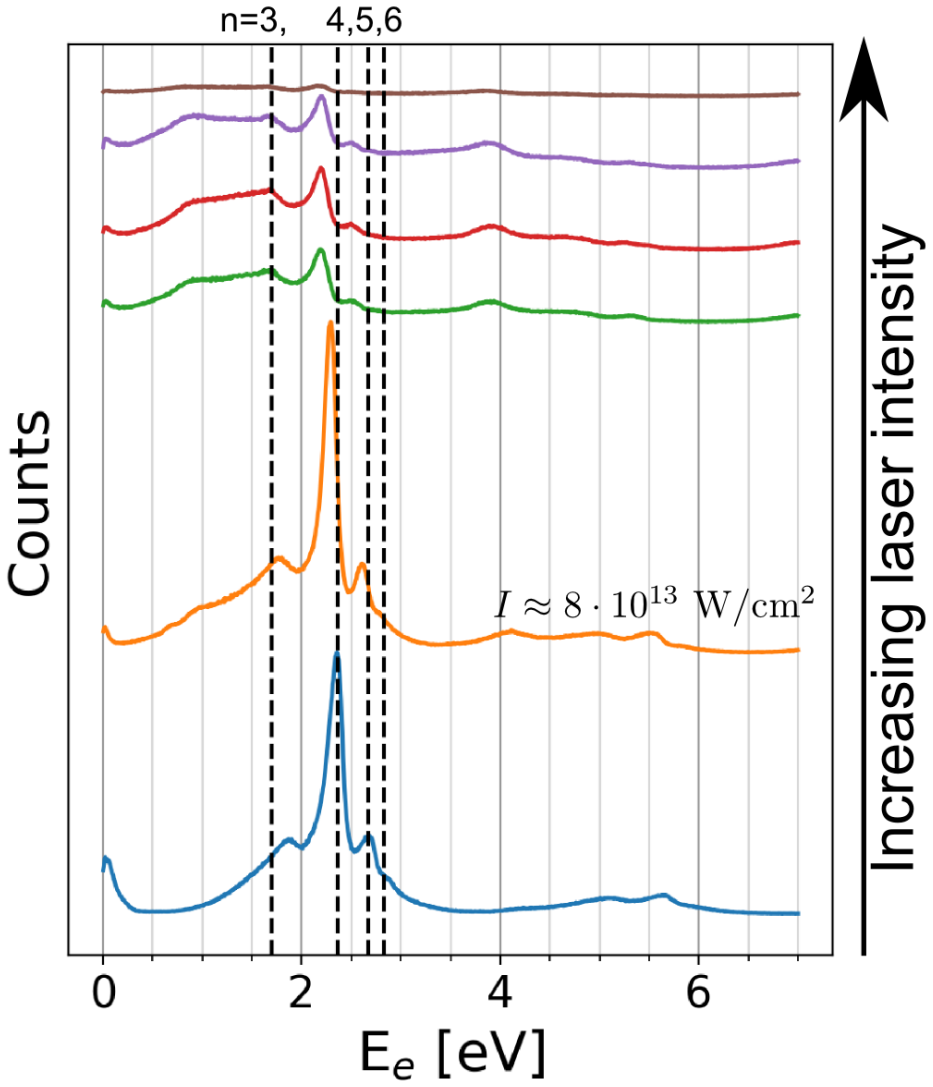

Figure 6.8.: Electron energy spectra of bound ionization for different intensities. The dashed vertical lines locates the positions of the resonance peaks from singly excited Rydberg states at the lowest intensity (blue curve). All the presented measurement results in this sec. 6.1.2 are associated to the orange measurement at an intensity of $8 \cdot 10^{13}$W/cm^2.

resonances for the KER regions ranging between 0.2 to 0.8 eV. Unfortunately, we cannot assure that the electrons, that cause the Rydberg peaks, really originate from dissociative ionization since we cannot detect this ionization channel in coincidence (as explained in sec. 5.3.4).

It can be seen that the resonance peak for n=6 is shifting to lower energy values when

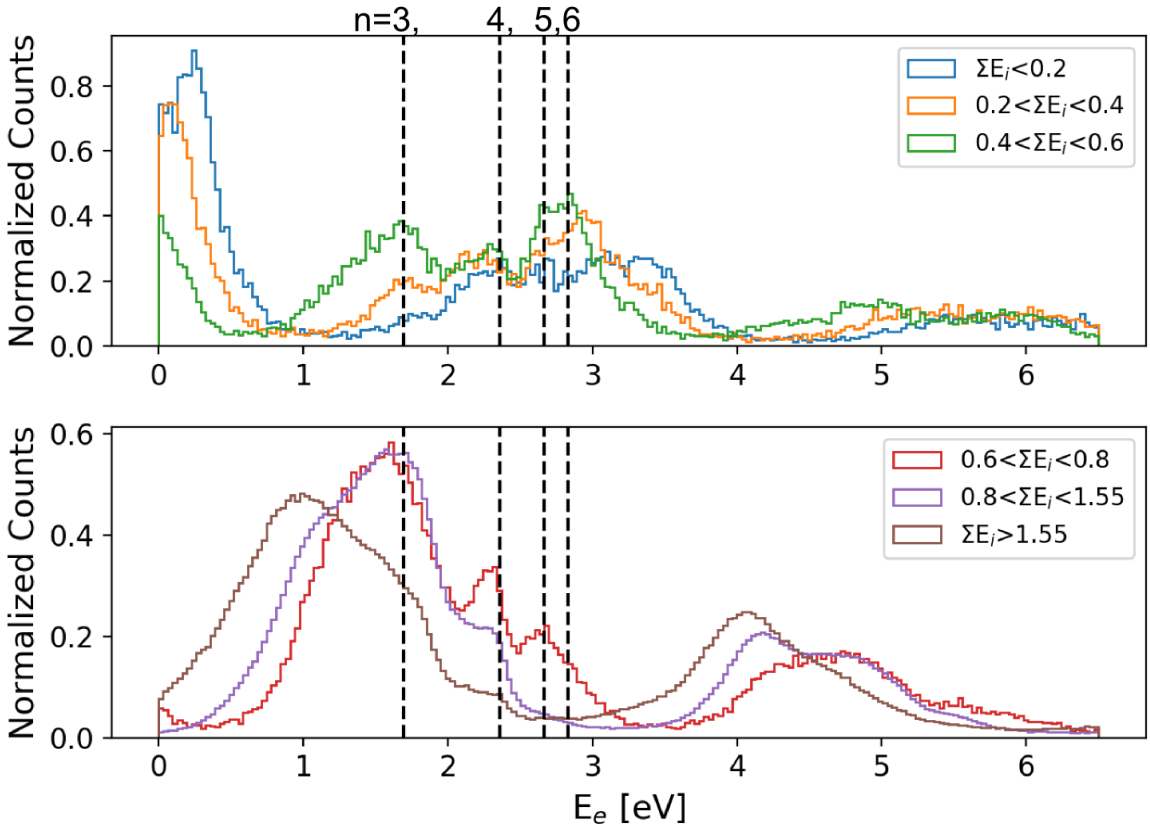

Figure 6.9.: Electron energy spectra from dissociation for different KER regions. These plots are equivalent to different KER slices from fig. 6.2 projected onto the x axis. The black dashed lines are located at exactly the same positions like in fig. 6.5 indicating the Rydberg resonances that are observed in bound ionization.

the KER increases, which is due to energy conservation between the emitted electron, the proton and the neutral hydrogen atom.

In fig. 6.2 there is a distinctive vertical line (marked as a black dashed line) between 0.8 and 1.55 eV KER at the n=4 Rydberg resonance which shows no dependence on the KER. Nevertheless the signal is still within the broad conservation line width. Since it is not possible to measure dissociation processes in complete coincidence due to the neutral hydrogen atom, this vertical line might also well be produced by non-coincident electrons that originate from bound ionization events.

The electron energy spectrum (fig. 6.5) and the JES (fig. 6.2) are by far not able to reveal a full picture of all the quantum mechanical pathways and their relative importance towards dissociation because of different reasons:

- The laser pulses are several tenths of fs long. Thus the photons have a certain energy uncertainty ΔE. In order to overcome the ionization threshold of H_2 (15eV) at least 5 photons à 3.14 eV (400nm) are required. So the energy uncertainty of n photons adds up to $\sqrt{n}\Delta E$. This prohibits to perform high-resolution spectroscopy. For this totally different experimental methods are required that do not rely on ultrashort laser pulses.

- Since the energy differences between the H_2^+ $1s\sigma_g$ and the singly-excited Rydberg states are of comparable size as the energy uncertainty due the laser photon bandwidth, dissociation via the H_2^+ $1s\sigma_g$ and the singly-excited Rydberg states happens at the same KER- and electron energy regions, which makes comparison difficult.

- Focal averaging is an effect, which cannot be prevented. Since the laser focus is not a singular point with well-defined intensity but a spatial intensity distribution, one can never perform measurements at exactly one intensity value. The AC-Stark effect leads to shifts in the energy levels of the molecular target, which makes the interpretation of the electron kinetic energy distributions more difficult.

In order to get an idea which quantum mechanical pathways dominate in the dissociation of H_2, molecular dynamics simulations were performed, as explained in the next section.

6.1.3. Nuclear dynamics TDSE-simulation for dissociation

Ideally, a simulation of the H_2 system should include nuclear and electronic motions both alike in order to take into account electron-nuclear correlations. Baier, p. 36 makes very clear that numerically solving the full Schrödinger equation of a H_2^+ molecule in three dimensions without approximation is computationally impossible. The full wavefunction involves 9 degrees of freedom. Assuming 100 grid points for each of these degrees results in 10^{18} numbers for storing the wavefunction. Choosing the low-storage-cost half-precision standard each number takes 16 Bytes, so in total a storage with $16 \cdot 10^{18}$ Bytes would be required.

It's clear that the problem has to be simplified appropriately. The Born-Oppenheimer approximation manages to separate the nuclear and electronic motion in such a way, that the internuclear distance becomes a parameter that determines the shape of the potential seen by the nuclei (see sec. 2.4.1). Nevertheless solving the electronic Schrödinger equation adequately is still a tough challenge because the electronic Hamiltonian exhibits singularities which are computationally not manageable without softening and thereby

changing the true potential. However, the nuclear motion can be modeled much easier using the analytically solvable Morse Oscillator model.

A time-dependent nuclear Schrödinger equation solver, as described in sec. 5.4, was implemented. The potential energy curves for the essential states were gathered from the Morse Oscillator model (see sec. 2.4.1). The corresponding parameters can be found in Sharp [80].

Testing the simulation software

In order to ensure that the simulation software works flawlessly a few quantum mechanical problems with well known temporal evolutions where solved.

The easiest nuclear dynamics problem is a vibrational eigenstate in a Morse potential. For the following test simulations we have chosen the Morse potential of the H_2^+ $1s\sigma_g$ state as shown in fig. 6.10. If there is no electric field applied and the initial wavefunction

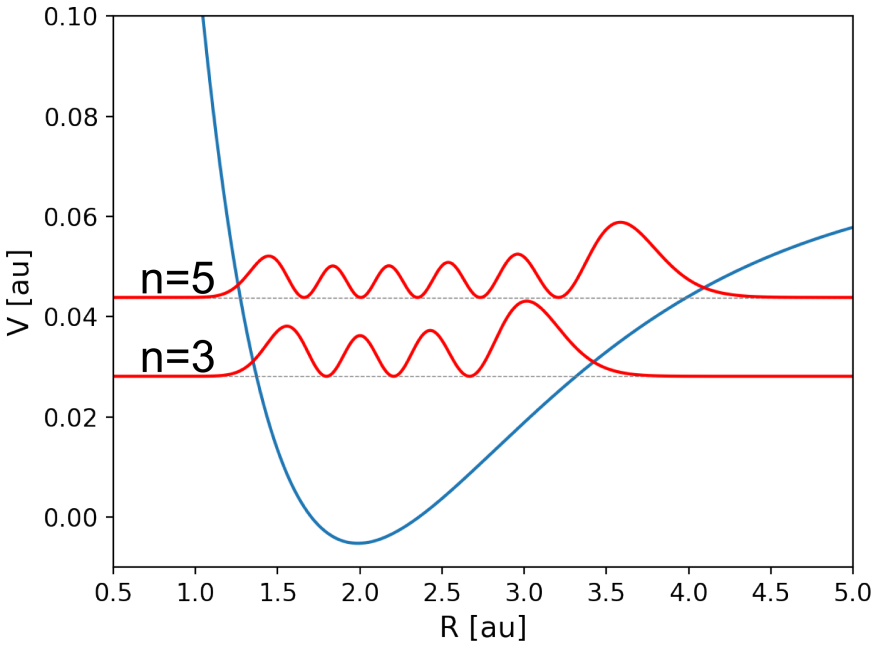

Figure 6.10.: Morse potential (blue), vibrational energy levels (grey dashed) and absolute values squared of the eigenstate wavefunctions (red) for $\nu = 3, 5$ of the H_2^+ $1s\sigma_g$ state.

is an eigenfunction of the Morse potential, then the simulation should not produce any temporal evolution since it is a stationary state. In fig. 6.11 we show the temporal evolution of the simulated nuclear dynamics starting from the vibrational state with

$\nu = 5$ and no electric field. The simulation runs over a time period of 1000 au≈25 fs

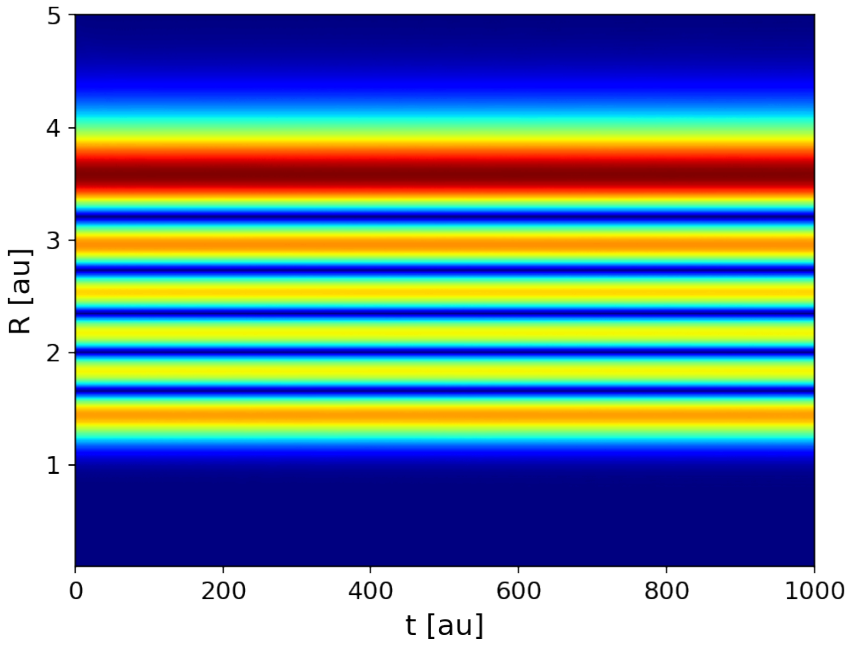

Figure 6.11.: The color plot shows the absolute value squared of the wave function $|\Psi(R)|^2$. The simulation started with the wavefunction of the vibrational state $\nu = 5$ in the Morse potential of the H_2^+ $1s\sigma_g$ state like shown in fig. 6.10 without electric field.

and shows no temporal evolution, as expected.

Instead of choosing a pure stationary eigenstate of the Morse potential we can also choose a superposition of eigenstates $\Psi_1(x, t_0)$ and $\Psi_2(x, t_0)$, which itself is not stationary anymore. But since it's a linear superposition of the eigenstates each of them will aquire a trivial phase shift $e^{-iE_{1,2}t/\hbar}$, where $E_{1,2}$ are the corresponding eigenenergies.

$$\begin{aligned} &\Psi(x, t_0) = \Psi_1(x, t_0) + \Psi_2(x, t_0) \\ \longrightarrow\ &\Psi(x, t) = \Psi_1(x, t_0)e^{-iE_1 t/\hbar} + \Psi_2(x, t_0)e^{-iE_2 t/\hbar}. \end{aligned}$$

Eliminating an overall phase of $e^{-iE_1 t/\hbar}$ yields

$$\Psi(x, t_0) = \Psi_1(x, t_0) + \Psi_2(x, t_0)e^{-i(E_2 - E_1)t/\hbar}.$$

At time T, where $(E_2 - E_1)t/\hbar = 2\pi$, the wavefunction returns back to the initial situation at t_0. This is called the revival time. Fig. 6.12 shows a simulation that

starts with a symmetric superposition of the $\nu = 3, 5$ eigenstates. The corresponding eigenenergies are $E_1 = 0.02812$ au and $E_2 = 0.04384$ au. Thus, the calculated revival time T is 400 au, which agrees with the simulation.

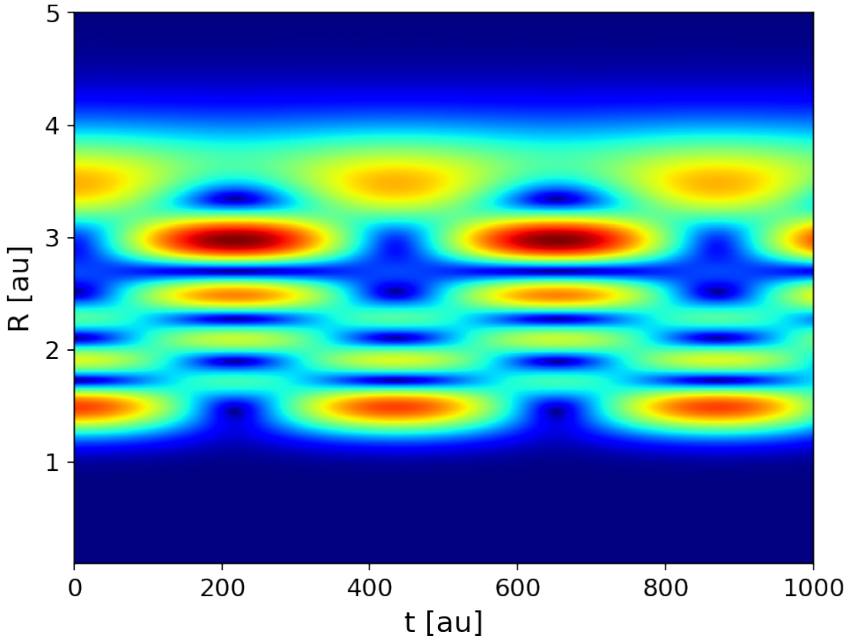

Figure 6.12.: The color plot shows the absolute value squared of the wave function $|\Psi(R)|^2$. See text for further explanation. The expected revival time T of 400 au can be reproduced accurately.

Singly-excited Rydberg states in dissociative ionization

In order to model the ionization and dissociation from singly-excited Rydberg states according to the previously described numerical methods (sec. 5.4) several difficulties appear.

Although the H_2 is still one of the smallest and easiest molecules known to mankind, it is already impossible to analytically solve its stationary Schrödinger equation. Approximation methods like molecular orbital theory are necessary to get an idea of the H_2 wavefunctions. If the desire is to model electron correlations, there is no way but taking both electrons into account. In our case, however, we are interested in the nuclear motion that is mediated by the electronic dipole transition element without caring about electron correlations in particular.

The dipole transition element between the initial excited Rydberg and finally dissociated H^++H state has to be calculated. For taking the emitted electron into account continuum states have to be considered. In the easiest case free electron wavefunctions in one dimension of the form $\Psi_e(r,t) \propto {}^{i(pr-Et)/\hbar}$ are usually considered with the dispersion relation of a free particle $E = \frac{p^2}{2m}$. This however requires to simulate another grid for the free electron momentum p. This computational extra effort is undesired here. In addition we do not care about the simulated quantum mechanical observables from the emitted electron since we have entirely excluded the electronic motion in our model. For this reason we simply neglect the Rydberg electron. Thus, the electronic wavefunction of the ground state electron in the singly excited Rydberg state is the wavefunction of the H_2^+ $1s\sigma_g$ state.

Initial conditions In the experiment the H_2 molecule is in its electronic and vibrational ground state before the laser pulse arrives. When the laser strikes, the molecule undergoes a transition to a higher electronic state. This transition is not simulated here. We assume that this process takes place at such a speed that the nuclear wavefunction barely changes and is simply left unchanged in the Rydberg state. So the initial wavefunction is taken to be the nuclear wavefunction of a ground state H_2 Morse potential with vibrational quantum number $\nu = 0$.The actual transition, that we want to simulate, is the one from the excited Rydberg (or bound H_2^+) state to the dissociation curve. It is assumed that this transition starts from the maximum field strength of the laser pulse. This is the reason why in the following simulation the laser pulse starts at its intensity maximum.

Basis states As already mentioned, the numeric simulation only focuses on the coupling between a bound Rydberg (or the H_2^+ $1s\sigma_g$) and the H_2^+ $2p\sigma_u$ state. Thus, the vector $\Psi(\mathbf{R},t)$ in eq. (5.9) has two components $\Psi(\mathbf{R},t) = (\Psi_1(\mathbf{R},t), \Psi_2(\mathbf{R},t))$ that correspond to the bound Rydberg (or the $H_2^+ 1s\sigma_g$) and the $H_2^+ 2p\sigma_u$ state, respectively. The dipole transition element $D_{12}(\mathbf{R}) = D_{21}(\mathbf{R}) = E \langle 2p\sigma_u | z | 1s\sigma_g \rangle$ is given by the coupling between the H_2^+ $1s\sigma_g$ and $2p\sigma_u$ states, also for the Rydberg states, since the Rydberg electron is neglected for the dipole transition. For the calculation of the R-dependent coupling the LCAO-orbitals were used, which is in very good agreement with calculations that include ab initio molecular orbitals [44, p. 100].

Simulated KER spectra Fig. 6.13 shows the KER distributions that result from the one-photon-dissociation starting from singly excited H_2 Rydberg states without involving

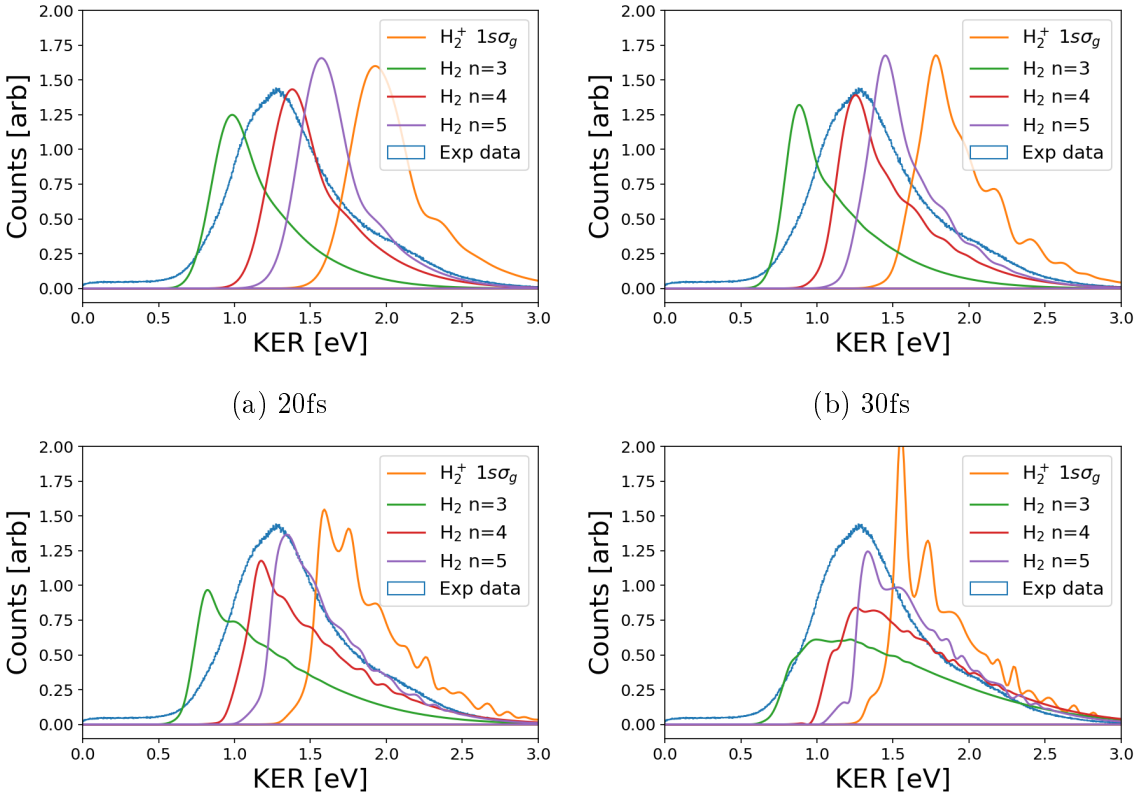

(a) 20fs (b) 30fs

(c) 50fs (d) 70fs

Figure 6.13.: Simulated KER spectra of the dissociation starting from different singly excited H_2 Rydberg states or the H_2^+ $1s\sigma_g$ curve for different pulse durations. A gaussian laser pulse with 400 nm central wavelength and peak intensity of 10^{14} W/cm^2 was used. Please note that the simulated spectra are all normalized and do not give any information on the relative transition rates.

any intermediate transition (see path (2) in fig. 6.7). All KER spectra have a similar shape which is due to the similarity of the potential energy curves. The peak positions however vary. The nearer the bound state is to the unbound curve, the less photon energy is necessary for dissociation. For a one-photon transition from the n=5 Rydberg state it is thus possible to dissociate already at small internuclear distances, whereas this is not possible for lower energy levels.

At small pulse durations the distributions are smooth, whereas for increasing durations distinctive peaks start to appear that decrease in distance with increasing KER. By reducing the pulse duration the frequency bandwidth is increased according to the uncertainty principle of the Fourier transformation. The photon energy is less precise and so are the KER spectra because the energy uncertainty is bigger than the spacing

between adjacent vibrational states. For bigger pulse durations and thus smaller photon energy uncertainty the individual vibrational resonances start to become visible.

Also, the peak positions are shifted to the right for lower pulse durations. If the pulse duration is shorter than the typical vibrational period of the respective state, then it will not be able to expand towards high internuclear distances before the laser pulse has ended. Dissociation is only possible at lower R values, which consequently results in a higher KER.

When comparing with the experiment, the KER distribution for $n = 4$ at 30 fs and for $n = 5$ at 50 fs are most similar to the experimental data. However, the peak position for the $n = 5$ KER is always larger than the experimental peak for all durations. For 30 fs the KER maximum of the $n = 4$ state coincides exactly with the experimental data.

Wu *et al.* [66] also simulated the KER distribution by means of a nuclear wave packet TDSE solver. Unlike in this thesis they used only the H_2^+ $1s\sigma_g$ and $2p\sigma_u$ curves for simulation. The theoretical and experimental data only agree with each other if the Franck-Condon factors are shifted up by 0.8 eV. From the present calculation it can be concluded that this shift could correspond to the dissociation threshold difference between the most prominent n=4 resonance in bound ionization and the H_2^+ electronic ground state, which is $(4\pi\varepsilon_0 \cdot 4^2)^{-1} = 0.85$ eV.

As a conclusion the simulation results match best to the experiment for the $n = 4$ H_2 Rydberg state. Although the photoelectron spectrum was not simulated, it is still possible to delimit the most important dissociation channel by comparing the ionic KER distribution to a simple nuclear dynamics model. In addition this finding agrees well with the fact, that in Single Ionization the majority of the recorded electrons are also coming from the $n = 4$ H_2 Rydberg state. It shows, that it is not in general valid to assume that dissociation happens only from the H_2^+ $1s\sigma_g$ state as described by the Two-Step Mechanism. In fact, the direct transition from singly excited Rydberg states to the H_2^+ $2p\sigma_u$ state plays the dominant role according to the results of this nuclear dynamics TDSE simulation.

6.1.4. Electron emission asymmetry in multiphoton-dissociation

Since Dissociation is an ionization channel, that can not be detected in coincidence with the ReMi, extreme caution has to be taken in deciding which detected events belong to dissociation and which do not (see sec. 5.3.4). When analysing the asymmetry parameter (fig. 2.12 on page 35) of electron emission in the molecular frame it is important to exclude possible asymmetry sources from the detection scheme. Since the laser pulses

are not CEP-stabilized and the pulse is long enough to cover several dozens of cycles, no preferred ejection direction of the proton and electron is expected in the laboratory frame.

In order to achieve a good momentum resolution in longitudinal direction a small electric field should be chosen. On the other hand this consequently means that ions with high enough transversal momentum can hit the spectrometer more easily because they have enough time to move far away from the spectrometer axis before they arrive at the ion detector. This limits the detection of protons as seen in fig. 6.14. The left plots show all events that are associated to dissociative ionization according to sec. 5.3.4. As can be seen from the projection on the $p_{\parallel,H^+}$-axis, there are more protons flying in positive than negative longitudinal momentum direction. In other words: Protons that initially fly towards the ion detector are more likely detected than those that fly away in opposite direction. This is because events with high transversal momentum in x- or y-direction are more likely to hit the spectrometer if they propagate away from the detector. It takes them more time to arrive at the detector compared to the other case. In this additional time of flight the ions move further away from the spectrometer axis and can clip at the spectrometer more easily before being detected. After removing the events with high transversal momenta ($|p_x| < 3$ au, $|p_y| < 3$ au) the asymmetry between protons flying in direction of and away from the ion detector can be removed successfully, as can be seen from the right plots.

Fig. 6.15 shows the asymmetry parameter of the proton with respect to the spectrometer/polarization axis. It shows that for KER$<$1.625 eV no significant asymmetry of the proton emission in the laboratory frame can be reported, as expected. Bins in which the count number is low are more noisy than bins on the conservation lines (see fig. 6.2).

In the same way the asymmetry parameter of the electron with respect to the spectrometer/polarization axis was plotted (fig. 6.16). There is a clear asymmetry in the electrons that is negative for the ATI-peaks and positive in the regions of low count numbers. In order to study the origin of this asymmetry, bound ionization events were investigated in the following.

Since Bound Ionization ($H_2 \rightarrow H_2^+ + e^-$) can be detected in full momentum-coincidence with the ReMi we can investigate more clearly whether the underlying electron asymmetry, that was observed in fig. 6.16, can be attributed to an experimental error or to a real physical effect. Fig. 6.17 shows the electron momentum distribution for bound ionization. Obviously, the electron asymmetry from 6.16 shows up as well in fig. 6.17 a) and c). This asymmetry characteristic depends crucially on the selected momentum

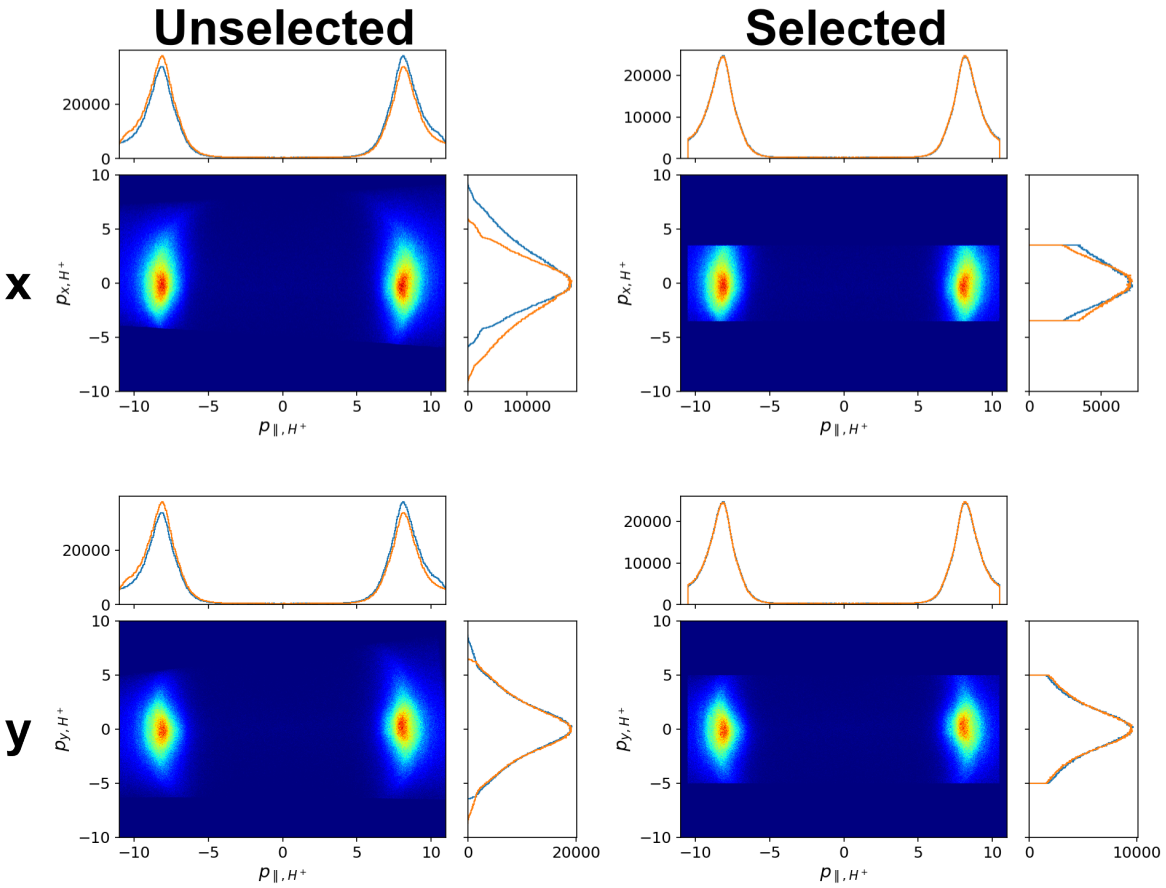

Figure 6.14.: Detection limits for protons from dissociative ionization with high momentum in x- or y-direction. In order to remove the significant asymmetry along $p_{\parallel}$ in the laboratory frame the asymmetric regions for high p_x- and p_y-momenta ($|p_x| < 3$ au, $|p_y| < 5$ au) had to be filtered out for the analysis of the asymmetry parameter. In the one-dimensional projection plots the orange curve is the blue curve mirrored around 0 in order to visualize the longitudinal asymmetry.

area. For low longitudinal momenta the oscillations in the asymmetry parameter are still visible, whereas for low transversal momenta these oscillations clearly disappear. This behavior strongly indicates that the electron asymmetry in the lab frame is mostly caused by the reconstruction nodes at $p_{\parallel} = -0.15$au and $p_{\parallel} = 0.5$au. Whenever an electron fulfills an entire cyclotron period the denominator of eq. (5.8) runs into a singularity that leads to large computational errors around them. That's why especially low-count-regions in the top right plot of fig. 6.17 can display large nonzero asymmetry parameter values.

Could the emerging electron emission asymmetry be caused by residual 800 nm pho-

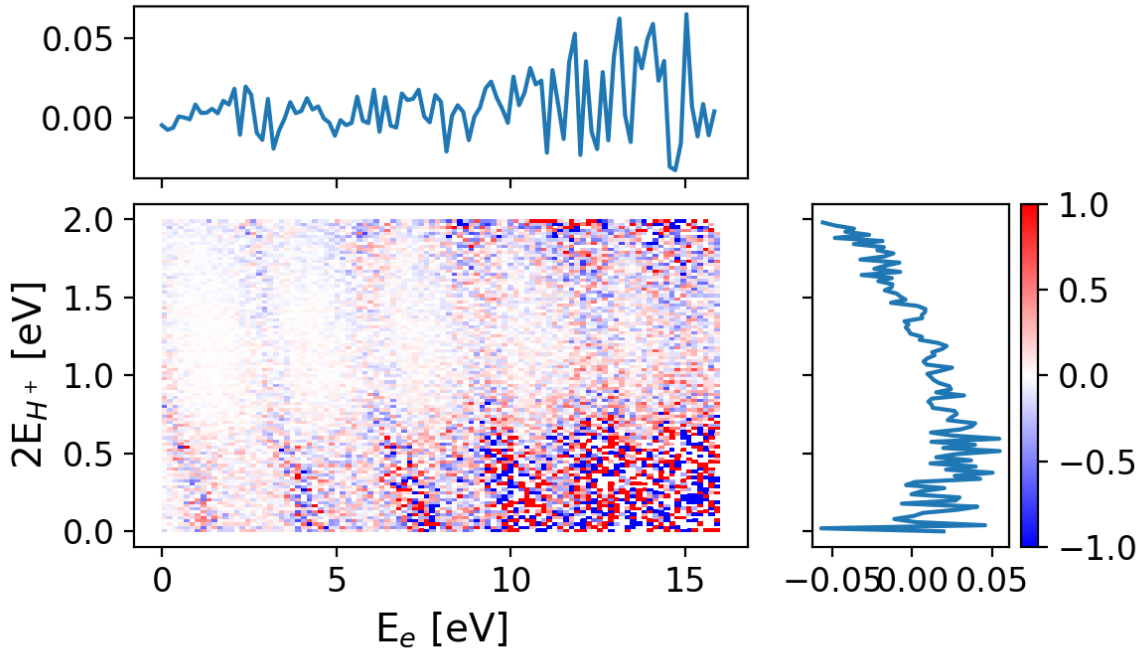

Figure 6.15.: Asymmetry parameter of the proton emission from dissociative ionization with respect to the spectrometer/polarization axis. All momenta are given in atomic units. The one-dimensional plots show the weighted-averaged projection of the asymmetry parameter. The weights were taken from the count numbers of the corresponding JES (analogous to fig. 6.2 but taking into account the events selection from fig. 6.14.)

tons that were not filtered out properly by the dielectric beam splitter? Often so-called Two-Color-experiments are performed to generate asymmetric electric fields [4, 82, 83] that influence the emission directions of the proton and electron. Since fig. 6.17 shows an asymmetry behavior that depends on the selection of the electron momenta a possible influence of residual 800 nm photons can be excluded. If this was the case, sideband structures should form in the middle of each ATI-peak, which can not be observed.

The discussion of experimental lab frame asymmetries is essential because they also influence asymmetries with respect to emission angles in the molecular system. Fig. 6.18 shows the experimental asymmetry parameter A (eq. (2.18) on page 35) as a function of the electron kinetic energy and the KER. The greyish contour lines indicate the conservation lines from the JES in fig. 6.2. The blue curve is the weighted average of the asymmetry parameter projected on the KER-axis and the red area describes

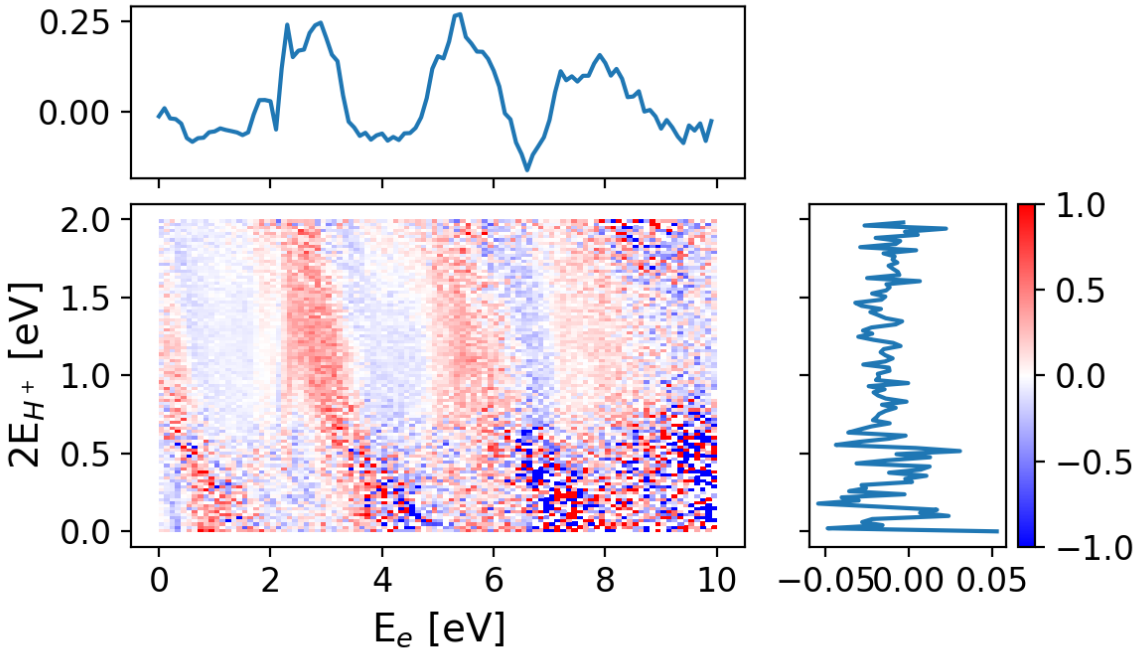

Figure 6.16.: Asymmetry parameter of the electron emission from dissociative ionization with respect to the spectrometer/polarization axis.

the weighted standard deviation. As a weight the counts from fig. 6.2 in each two-dimensional bin were chosen. The areas, which are off the conservation lines, will hardly contribute because their counts are negligible. Fig. 6.18 shows a clear pattern on the conservation lines. This pattern has a zero crossing at 1.16eV ($+0.22/-0.1eV$).

In sec. 2.4.2 the origin of such an asymmetry is explained in detail. It arises from the interference of two different ionization pathways. In order to perform simulations on the asymmetry it is necessary to identify these pathways. Since the KER- and total-energy-spectra (KER+E_e, see fig. 6.2) show distributions at very low energies, the pathways of interest must be restricted to direct- and one-photon-dissociation. However, from the recorded data it is not possible to identify which exact electronic states contribute in the one-photon-dissociation. It could be the $1s\sigma_g$ state as well as singly excited Rydberg states, as they were observed in the process of bound ionization previously (fig. 6.5) and simulated in dissociation in sec. 6.1.3. In order to determine the correct pathways asymmetry simulations were performed for the different possible electronic states of H_2 and H_2^+. Fig. 6.19 shows the asymmetry parameter simulation using the direct and one-

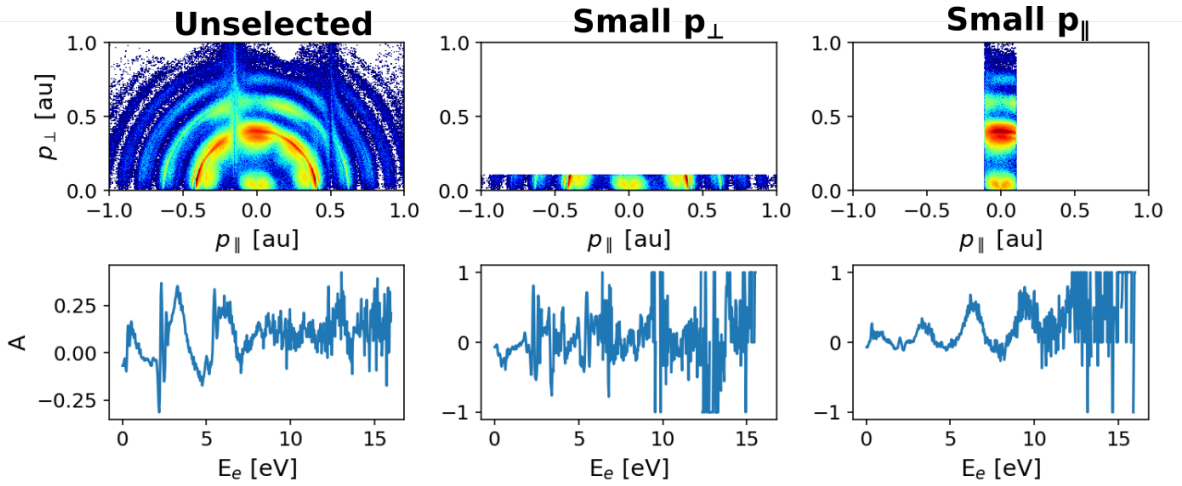

Figure 6.17.: Asymmetry parameter of the electron emission with respect to the spectrometer/polarization axis as a function of the electron energy for Bound Ionization at different momentum selections. The upper graph always shows the selected electron momenta. In the lower part the electron energy spectra of the respective excerpt are presented.

photon-dissociation paths via different electronic molecular states (see fig. 2.13 on page 36). In detail the direct dissociation always happens via the H_2^+ $1s\sigma_g$ curve, whereas for the one-photon-absorption different initial states were chosen (H_2^+ $1s\sigma_g$ and bound singly excited Rydberg states). The used photon energy is 3.14 eV according to the ATI-peak distance from fig. 6.5 and the conservation line distance in fig. 6.2. The laser spectrum was asummed to be the frequency-doubled spectrum of the measured Ti:Sa-laser spectrum in fig 5.3 on page 58. In addition the Franck-Condon factors, as shown in fig. 2.11 on page 29, are included in the simulation. They are used for the H_2^+ $1s\sigma_g$ as well as for the Rydberg states since the potential shape and its offset along the axis of the internuclear distance basically do not change. In total the molecule always absorbs 7 photons in the simulation, which corresponds to the first fully visible line in fig. 6.2. The simulation error due to the finite laser bandwidth is negligible compared to the 1σ-error of the experimental data. For easier readability the simulative error is not shown here. Only in case of a well-defined number of absorbed photons the semiclassical WKB-theory from section 2.4.2 can be used. Otherwise, symmetry considerations for the emitted electron wave functions do not hold any longer.

The simulations for the singly-excited Rydberg states n=4-6 are in good qualitative agreement with the experimental trend within the 1σ-error. The asymmetry is negative for KERs below 1.25eV and rises for higher KER, where it stays positive. Within the

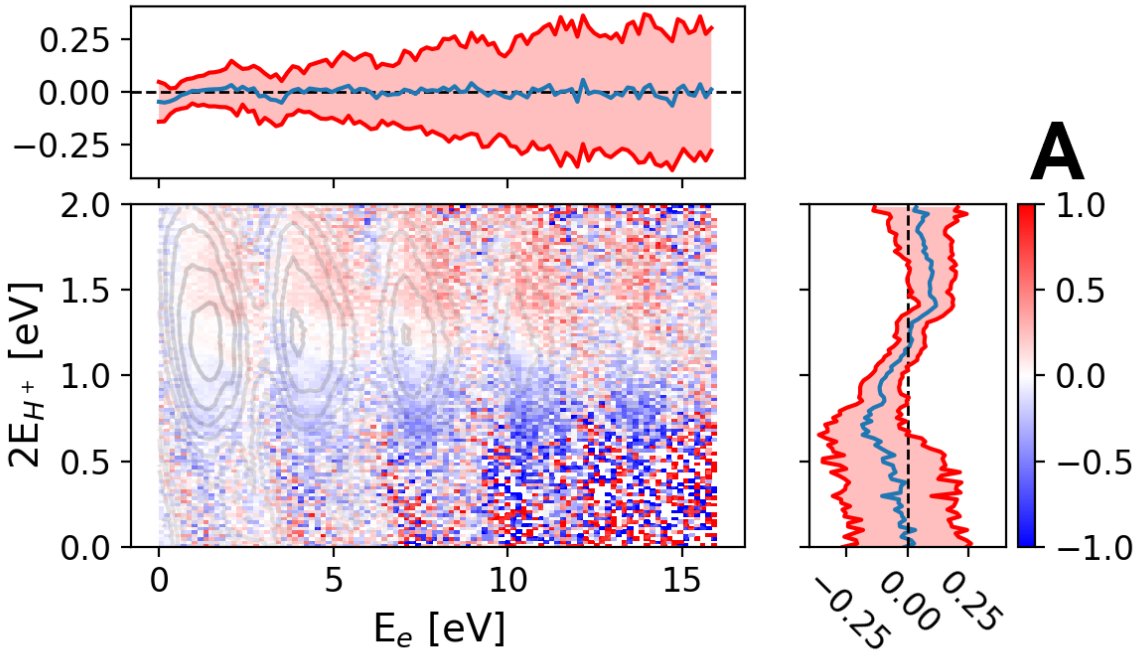

Figure 6.18.: Here the assymetry parameter A in the molecular frame of the dissociative ionization of H_2 as defined in eq. (2.18) is plotted as a function of the electron kinetic energy E_e and twice the proton kinetic energy (which approximates the kinetic energy release of proton and neutral hydrogen atom). On the right the projection of the experimental asymmetry parameter onto the y-axis is shown (see text for detailed explanation).

KER region of 0.6-1.5eV the trend and slope of the experimental and theoretical data are in very good agreement. $\Delta\xi$ is the free parameter that describes the electron phase difference (see sec. 2.4.2 on page 38) and was chosen such, that the simulated curves fit best to the experimental asymmetry parameter.

The asymmetry distribution extends towards higher KER-values if the principal quantum number n rises and vice versa. The positive peak position fits best for the cases n= $4, 5$. However, the differences between the different Rydberg states is only very small.

For n= 3 the simulation agrees very well in the KER-range from 0.5-1.25eV. The n=3 Rydberg state is significantly further away from the $2p\sigma_u$ curve then n= 4. Thus, the KER distribution contributes at smaller KER values, as can also be seen from the KER-simulations in fig. 6.13. However, the fast oscillating signature below 0.5eV can neither be verified nor falsified in the experiment due to a lack of statistics in this area.

All in all, the n= 4 simulation curve fits best to the experimental data in the range between 0.6 and 1.5 eV where the experimental statistics is best. Therefore it is believed that this state plays an important - if not the most important - part in the electron localization asymmetry of the dissociation process. This also agrees well with the findings from the KER simulations in sec. 6.1.3 because the simulated KER distributions fit best to the n=4 and n=5 Rydberg states.

The simulation is not able to reproduce the experimental asymmetry amplitude correctly because it assumes a symmetric superposition of the two ionization pathways with equal weightings. In order to improve this aspect a fully quantum mechanical simulation would be necessary [44, p. 67].

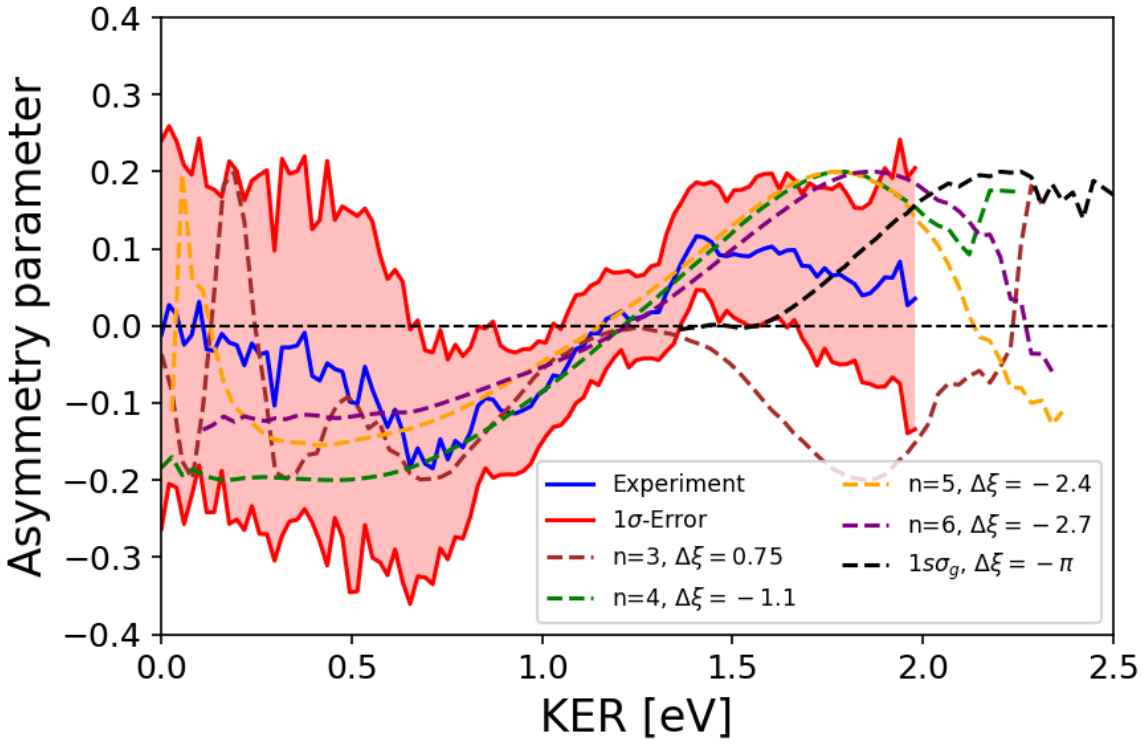

Figure 6.19.: WKB-Simulations of the asymmetry parameter for interference between direct dissociation via the $1s\sigma_g$-state and one-photon-dissociation via a singly-excited Rydberg or the $1s\sigma_g$-state (see labels). For comparison the experimental KER behavior from 6.18 was plotted again. $\Delta\xi$ is the electronic phase (see sec. 2.4.2 on page 38) that serves as a free parameter. It was chosen such that every curve fits best to the experimental data. All simulated curves are scaled with the factor 0.2 for better comparison with the experiment.

Direct dissociation to the $1s\sigma_g$ state is known to happen at low KER for XUV-single-photon experiments because of small Franck-Condon overlapping in the high KER region. To our knowledge direct dissociation with KER>1 eV was not reported yet for single- and multi-photon dissociation experiments[84]. In case of multiphoton ionization, intermediate excited states are known to play important roles [12, sec. 5.3]. For these reasons it is advisable to look for other pathways beside direct dissociation that might contribute to the observed asymmetry behavior.

The net-two-photon-absorption as shown in fig. 6.20 plays a crucial role in the double ionization of H_2 using 400 nm photons with a pulse duration of 60 fs according to Lu *et al.* [68]. Fig. 6.20 visualizes the process in detail. Three photons are absorbed to go from the $1s\sigma_g$ to the $2p\sigma_u$ state of the singly ionized H_2^+ cation. After some time when the vibrational wave packet has rolled down the potential curve a 400 nm photon is emitted and the system falls back to the $1s\sigma_g$ state. The aquired kinetic energy is sufficient to overcome the remaining potential barrier and the molecule dissociates. A straightforward calculation assuming resonant coupling between the two potential curves yields a KER value of at least 3.6 eV (photon energy: 3.14 eV) for the net-two-photon dissociation, which is beyond our observations.

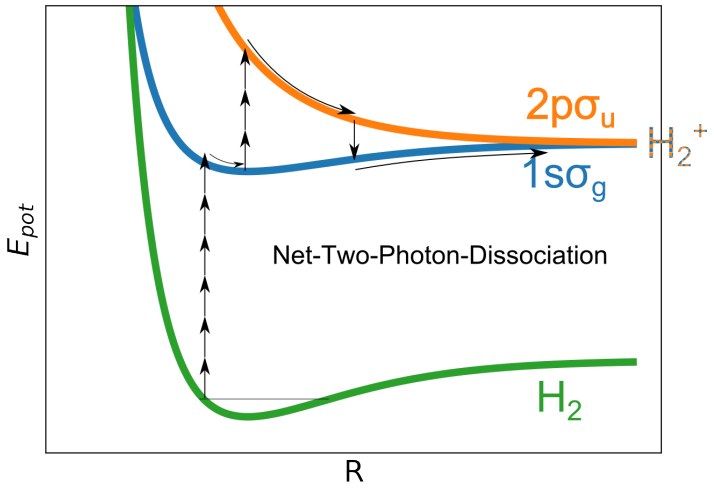

Figure 6.20.: Dissociation pathway of the net-two-photon process. Due to the different parity of the $1s\sigma_g$ and the $2p\sigma_u$ states coupling between them is only dipole-allowed for an odd number of absorbed photons. If however another photon is released via stimulated emission after that, the net-photon-absorption sums up to two photons in the end.

Fischer *et al.* [10] reports about an electron localization asymmetry that is caused by an interference between the $2p\sigma_u$ and a doubly excited Q_1 state when using an

XUV photon for ionization. Fig. 6.21 shows the asymmetry parameter values of this simulation. It becomes clear that this asymmetry pattern is not the one we see in the

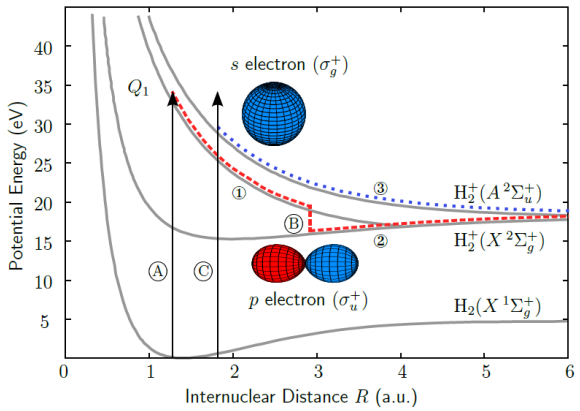

(a) Pathways that were used to simulate the asymmetry in Fischer *et al.* [10]. Figure taken from [44].

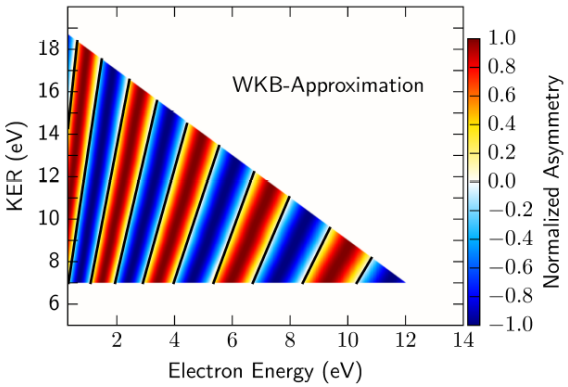

(b) Simulated asymmetry parameter. Figure taken from [44].

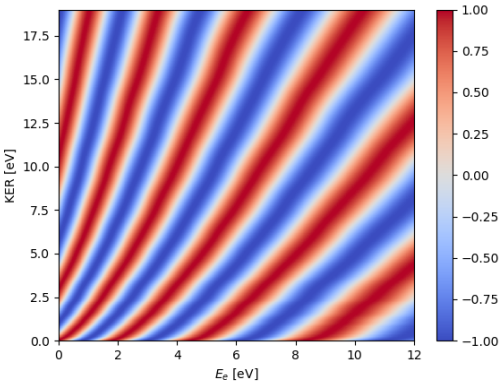

(c) Same simulation as (b) but extended to lower KERs.

Figure 6.21.: Asymmetry parameter for the interference of $2p\sigma_u$ and the lowest Q_1 state.

experimental data of this work. Moreover doubly excited states lead to much higher KER values up to 10eV and more. Thus, this ionization dynamics does not play any role for the case of multiphoton ionization experiments with 400 nm central wavelength.

As a conclusion, the comparison between the simulation and the experimental data of the asymmetry parameter, as shown in fig. 6.18 and 6.19, strongly indicates that the observed asymmetry behaviour as a function of the KER in dissociation is exclusively caused by the interference of the direct and one-photon-dissociation pathways via the H_2^+ $1s\sigma_g$ and the underlying H_2 singly excited Rydberg states. Contributions from the net-two-photon path and the unbound Q_1 curve could be excluded. This finding is in

agreement with the observation of Rydberg resonance peaks in bound ionization (fig. 6.5) and the nuclear dynamics simulations from sec. 6.1.3.

6.2. First pump-probe experiment with the pulse shaper

After we have discussed the role of singly-excited Rydberg states in the previous section it is plausible to ask how ionization processes via different pathways can be controlled with the help of laser pulses. Strong-field coherent control of photodissociation dynamics was already reported in calculations and experiments with e.g. IBr molecules [85–87]. Nowadays VMI spectrometers are most often used in connection with pulse shapers because they allow fast measurements of electron and ion momentum distributions. Kerbstadt *et al.* [88] and Pengel *et al.* [89] imaged electron vortices from femtosecond multiphoton ionization with a VMI and demonstrate coherent control of quantum processes. However this imaging technique does not allow coincident measurements. Therefore the following section reports about a first successful try to combine a pulse shaper with a ReMi.

Fig. 6.22 describes the experimental setup. At first the laser beam diameter from the Ti:Sa laser is roughly halved from 10 to 5 mm. The polarization axis of the 30 fs pulses is turned via a $\lambda/2$-waveplate until the polarization is perpendicular to the laser table. This ensures equal intensity of the pump- and probe-pulse because the SLM-module of the pulse-shaper consists of two phase-retarding displays that address polarization-components, which are each $\pm 45°$ off the table normal (see fig. 2.10 on page 18). Before the pulse-shaper is used for generating a pump-probe scheme the incoming pulse is compressed as described in sec. 5.2.4. After the phase-shaping is completed the resulting electric field consists of two identical laser pulses that are separated by a time-delay τ. The polarization of these two linearly polarized pulses is $\pm 45°$ compared to the table normal. For tuning the relative orientation of the two orthogonal pulses in the ReMi a second $\lambda/2$-waveplate was used to match the polarization directions of both pulses with the y- and z-axes in the ReMi (see fig, 5.14). In order to perform a pump-probe experiment with our pulse shaper device it is necessary to find out the proper frequency-dependent phase shift function $\Delta\phi(\omega)$, that has to be applied to get an exact but delayed copy of the original pulse (see sec. 2.3). The two orthogonal polarization components can be shaped independently. Display A does not introduce any phase shifts at all: $\Delta\phi_A(\omega) = 0$. Display B delays its polarization component in time. The temporal delay of a pulse is given by the group velocity (see (2.3) on 14). Consequently display

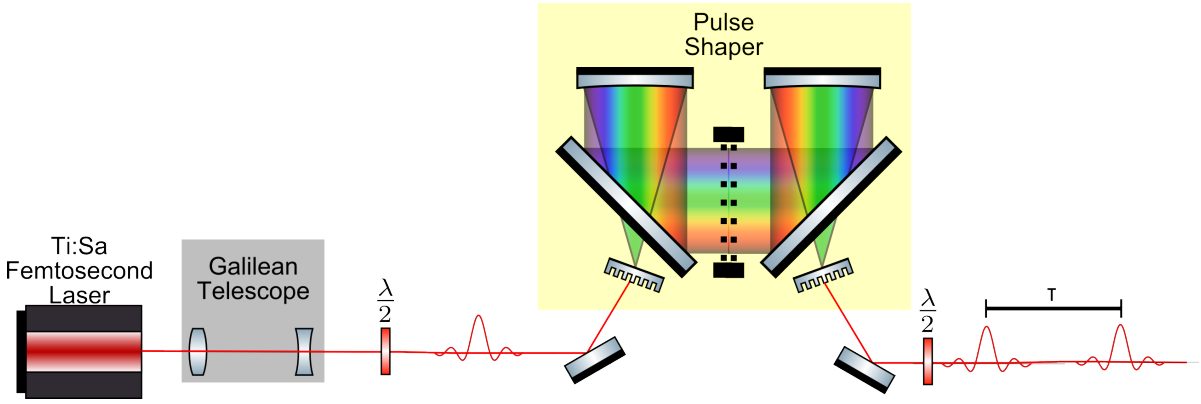

Figure 6.22.: Pump-Probe experiment using the phase shaper setup as described in sec. 5.2. Since the spectral width of the femtosecond laser pulses from the Ti:Sa-laser is not very broad gratings with a line spacing of a= $6.\overline{6}\cdot 10^{-4}$mm were chosen. Please note that this is merely a sketch that does not describe the polarization states of the two pulses adequately. The initial linear polarization vector of the incoming pulse is perpendicular to the laser table. The polarization vectors of the outgoing pulses are orthogonal to each other, each ±45° off the table normal.

B has to provide a linear phase function $\Delta\phi_B(\omega) = \tau(\omega - \omega_0)$, where $\tau = \frac{\partial\phi}{\partial\omega}$ is the time delay and ω_0 is the central angular frequency of the laser spectrum. This phase function is changed every 500 ms in steps of $\Delta\tau = 0.5$ fs. It has to be mentioned that this phase shift is not equivalent to the phase shift $\Delta\phi_{MZ} = \tau\omega$, that is introduced in a Mach-Zehnder interferometer. The difference is, that the Mach-Zehnder interferometer shifts the carrier fields of both pulses with respect to each other leading to constructive and destructive interference, whereas the pulse-shaper phase function $\Delta\phi_B(\omega) = \tau(\omega - \omega_0)$ shifts the envelopes with respect to each other leaving the carrier-phase relation between the both pulses unchanged. For this reason the latter case always leads to constructive interference at any time-delay.

In order to investigate the state of polarization of the electric field it is advisable to look at the ion momentum distribution from dissociative ionization and the electron momentum distributions of bound ionization. In both cases the preferred particle emission direction is along the laser polarization [65, 90]. Fig. 6.23 shows the two charged particle momenta distributions in form of 2-dimensional color plots along every possible combination of cartesian momentum components. As a reminder (see fig. 5.14 on page 73): The laser propagates along the x-ayis, the gas-jet along the y-axis and $p_{\|}$ is the direction of the spectrometer axis (z-axis). The fact, that the above momentum distributions show a cross in the y-z-plane, proofs that pump- and probe-pulses are oriented

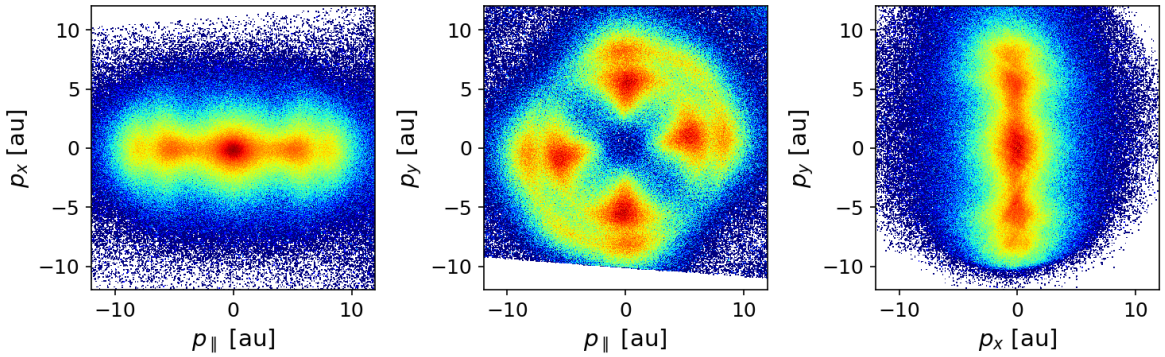

(a) H^+ ion momentum distribution from dissociative ionization.

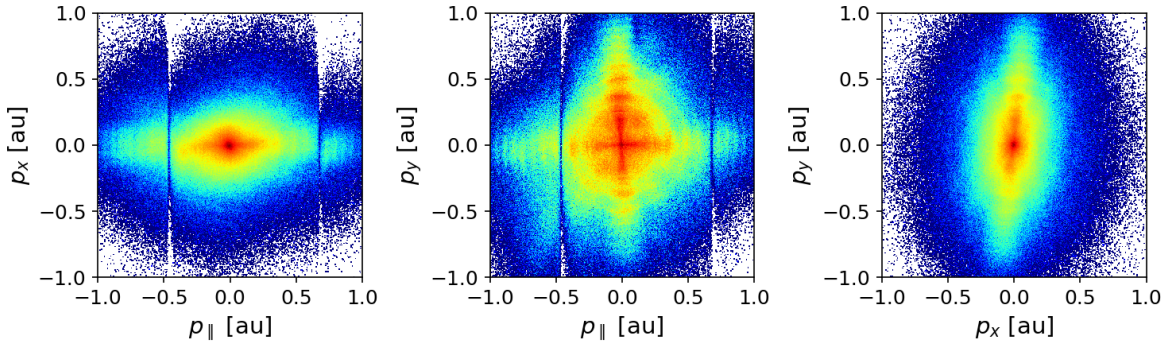

(b) Electron momentum distribution from bound ionization.

Figure 6.23.: Ion and momentum distributions that indicate the polarization directions of pump and probe pulse. All presented momentum distributions are integrated over all time-delays from -600 to 600 fs.

perpendicularly to each other along the y- and z-axes in the non-overlapping time-delay region.

Characterization of femtosecond laser pulses is usually performed with a second-order autocorrelation measurement. However, the multiphoton-ionisation process in the ReMi can also serve as a rough estimation of the pulse duration. Fig. 6.24 shows the count number of detected bound ionization events as a function of the time delay. There is a clear region around 0 fs at which the two pulses overlap and interfere with each other. This leads to the typical autocorrelation envelope. The FWHM is around 60 fs and serves as a good indicator for the magnitude of the pulse duration. In addition

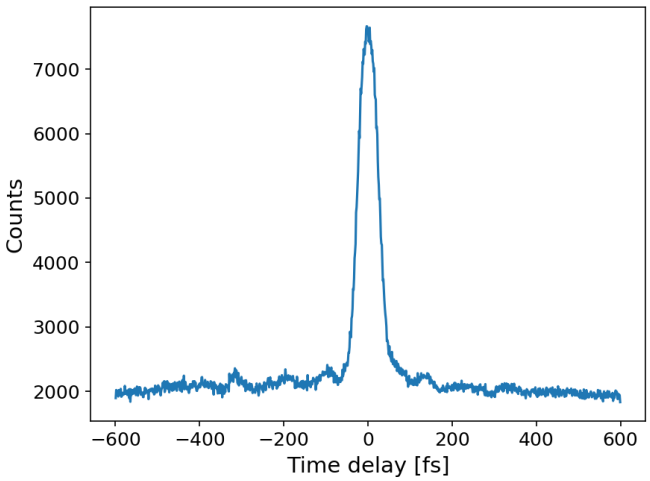

Figure 6.24.: Histogram of the counts as a function of the time delay for bound ionization.

the autocorrelation trace shows that the carrier phase relation between both pulses is independent of the time-delay. If it was not, then the polarization of the laser field in the overlapping region would turn from linear over elliptical to circular and back again since the two pulses are oriented perpendicular to each other (see fig. 6.25). This would lead to a decrease in counts as soon as the polarization becomes elliptical or circular because of a decrease in electric field strength amplitude compared to the case of linear polarization. In order to proof the constant carrier-phase relation fig. 6.26 shows the measured state of polarization of the electric field in the overlapping time-delay region from -20 to 27 fs. Here the protons from dissociative ionization and electrons from bound ionization are not emitted like a cross but along the 45° diagonal, which shows that the laser polarization is linear in the overlap region, as expected from two orthogonal, delayed pulses with a relative carrier-phase offset of 0 (see fig. 6.25).

As a proof, that the setup from fig. 6.22 is working properly, the goal was to reproduce former Mach-Zehnder pump-probe measurements by Mi *et al.* [91]. In this experiment the same Ti:Sa-laser was used but instead of a pulse-shaper a Mach-Zehnder interferometer delays one pulse with respect to the other. In addition a $\lambda/2$-waveplate is implemented in one of the interferometer arms to achieve orthogonal polarizations between the two pulses. The results are shown in fig. 6.27. Here positive time-delay means that the more intense probe pulse ($I = 4{\cdot}10^{14}\mathrm{W/cm^2}$) comes first. The less intense pump pulse ($I = 1 \cdot 10^{14}\mathrm{W/cm^2}$) follows afterwards. Two prominent ionization channels are visible - the net-two-photon-absorption, called Above-Threshold-Dissociation (ATD)

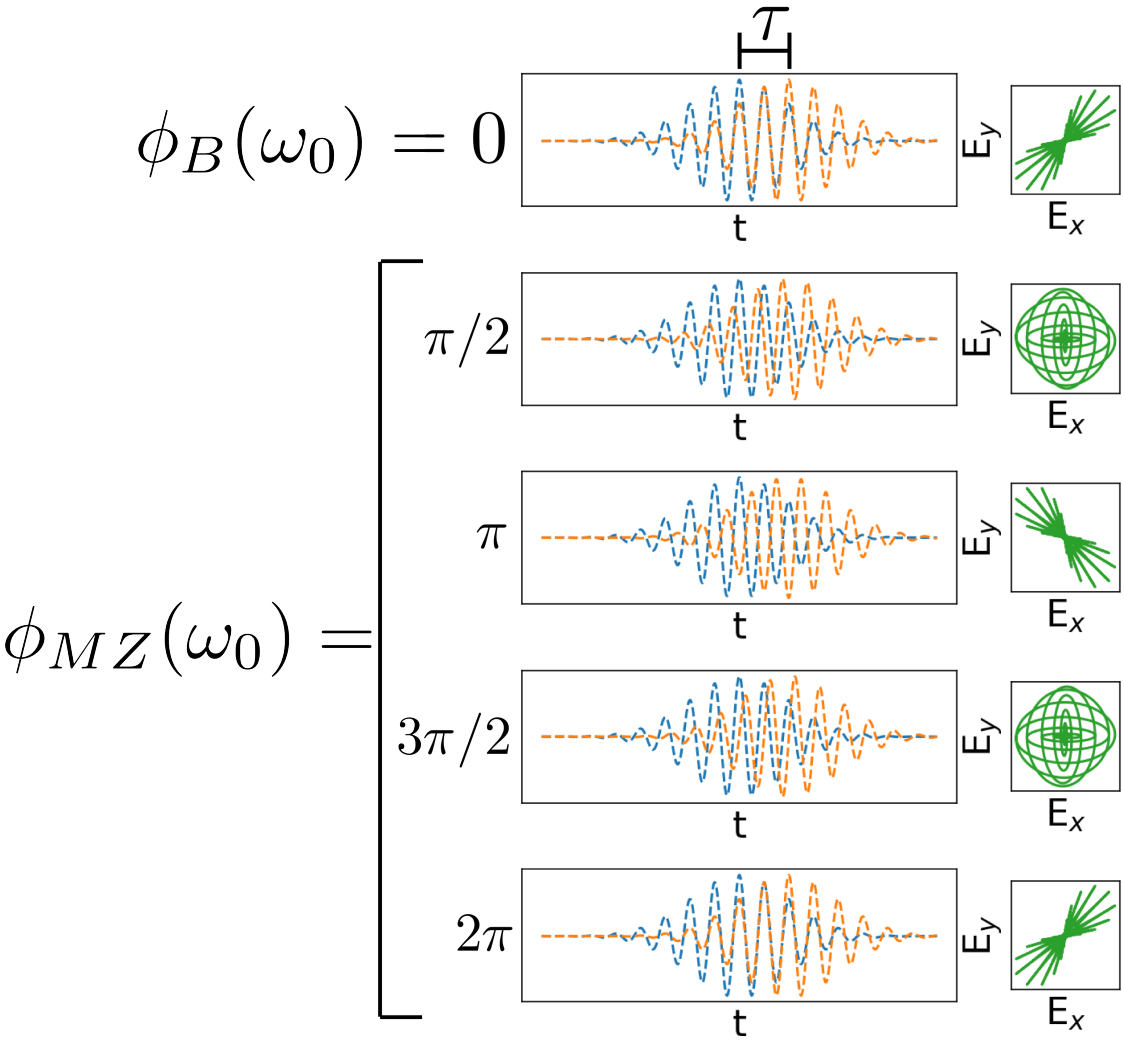

Figure 6.25.: State of polarization for the different phase shaping functions $\Delta\phi_B(\omega) = \tau(\omega - \omega_0)$ and $\Delta\phi_{MZ} = \tau\omega$. The left plots show the temporal pulse profile of the pump along the x-axis in blue and the probe along the y-axis in orange. The laser propagates along the z-axis. The right plots show the projection of the total electric field in the x-y-plane integrated over time.

in the figure, and the charge-resonance enhanced ionization, called enhanced ionization (EI) in the figure. Mi *et al.* [91] was able to observe two oscillation frequencies at 10.6 and 17.6 THz (fig. 6.27 (b)). These agree well with the rotational transitions $J : 0 \rightarrow 2$ and $J : 1 \rightarrow 3$ in the electronic ground state of H_2.

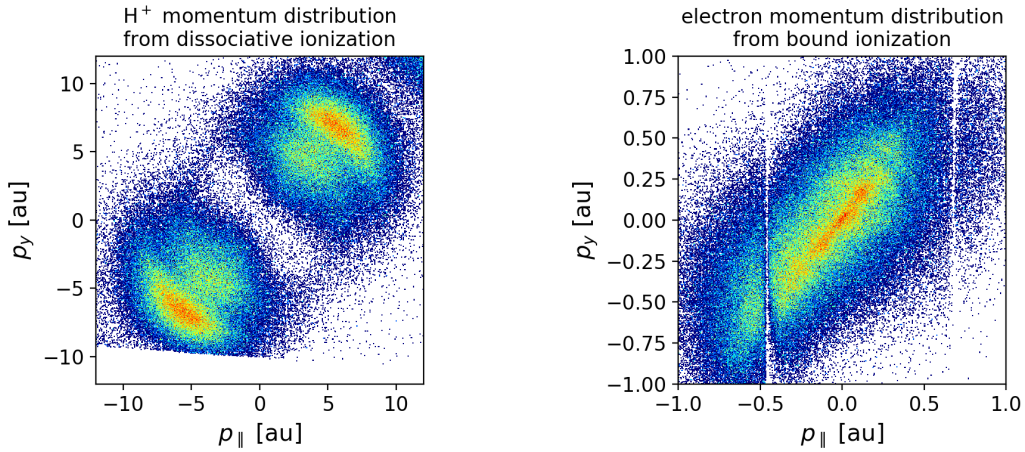

Figure 6.26.: Momentum distributions in the time-delay overlap region from -20 to 27 fs. The emission direction and thus the linear polarization is roughly 45° off the y- and z-axes, as expected.

For negative time-delays a clear oscillation with a period of roughly 100 fs is visible in fig 6.24. Further investigation of the dissociative and double ionization channels from the pulse shaper experiment show the same oscillatory behavior (fig. 6.28). It gets clear that we are able to observe the same ionization channels as Mi *et al.* [91]. The Fourier analysis of a properly chosen excerpt from the time-dependent oscillating signals shows that the inherent frequencies range between 10-15 THz (see fig. 6.29). This finding fits to the observation by Mi *et al.* [91]. Unfortunately the oscillation is by far not as clear as in the Mach-Zehnder experiment. This can be due to several reasons. The intensity ratios between the pulse-shaper- and Mach-Zehnder-experiment differ significantly. Here the laser polarization of the pulses going into the pulse-shaper was aligned perpendicular to the laser table such that a symmetric vectorial decomposition into the ±45°-components is achieved leading to an estimated intensity ratio of ≈ 1. The fact, that it is not possible to block only one of the pulses in the shaper-setup, is a clear drawback compared to experiments with a Mach-Zehnder-interferometer. For this reason no intensity value can be given. Mi *et al.* [91] used an intensity ratio of 4 between pump and probe pulse. In principal it is possible to tune the intensity ratio by turning the waveplate in front of the SLM module through the angle $\alpha = \arctan\left(\sqrt{I_{probe}/I_{pump}}\right) - \pi/4$. However, it is hard to properly reproduce desired intensities because there is no reliable method to measure them accurately, since it is not possible to block only one of the pulses.

The KER distributions from fig. 6.28 differ from those in fig. 6.27 in one aspect. The EI- or CREI-channel at high KER values (3-8 eV) is much weaker in the pulse-

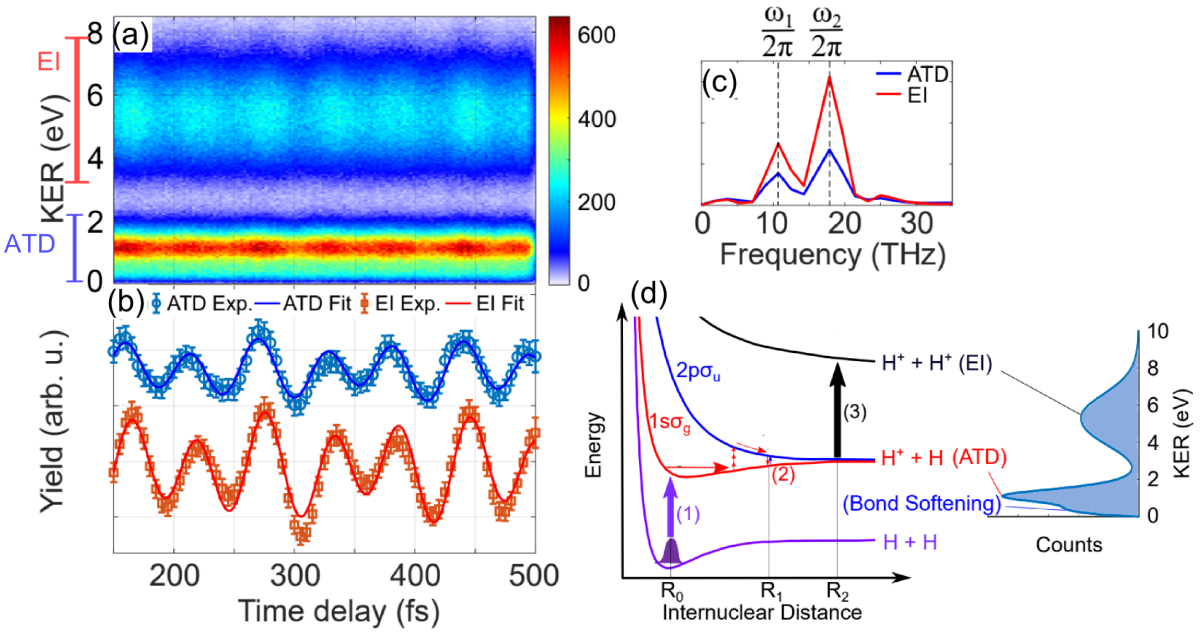

Figure 6.27.: Rotational wavepackets in dissociation and double ionization of H_2. (a): Counts of H^+-ions as a function of the time-delay and the KER. At KERs from 0-2 eV Above-Threshold-Dissociation (ATD) takes place while charge-resonance enhanced ionization (CREI or EI) results in a KER between 3-8.5 eV. (b): shows the KER-integrated oscillation signal of the two aforementioned channels as a function of the time-delay. (c): Fourier transform of the measured signals from fig. (b) in order to determine the underlying frequencies of the visible oscillation. The two frequencies found are used to fit a superposition of two cosine-functions to the data in (b). (d): Explanation of the measured KER spectrum and the underlying ionization channels.

shaper measurement relative to the ATD-channel in comparison with the Mach-Zehnder measurement. This is due to the high intensity of the probe pulse in the Mach-Zehnder experiment. Its intensity is sufficiently high to efficiently doubly-ionize the H_2 target without the need of the following pump pulse. Consequently the pulse duration limits the time that the singly ionized H_2^+ ion has to expand its internuclear distance before it finally undergoes Coulomb-explosion at the moment of second ionization. This leads to a high KER value. In contrast to this, the effect of the weaker pump pulse on the last ionization towards Coulomb-explosion (see step (3) in fig. 6.27 (d)) is rather small. Thus the chance, that this step happens at huge internuclear distances leading to practically no gain in KER, is much smaller as compared to the pulse-shaper measurement, where the intensity of both pulses is smaller than the probe pulse used by Mi *et al.* [91]. This is

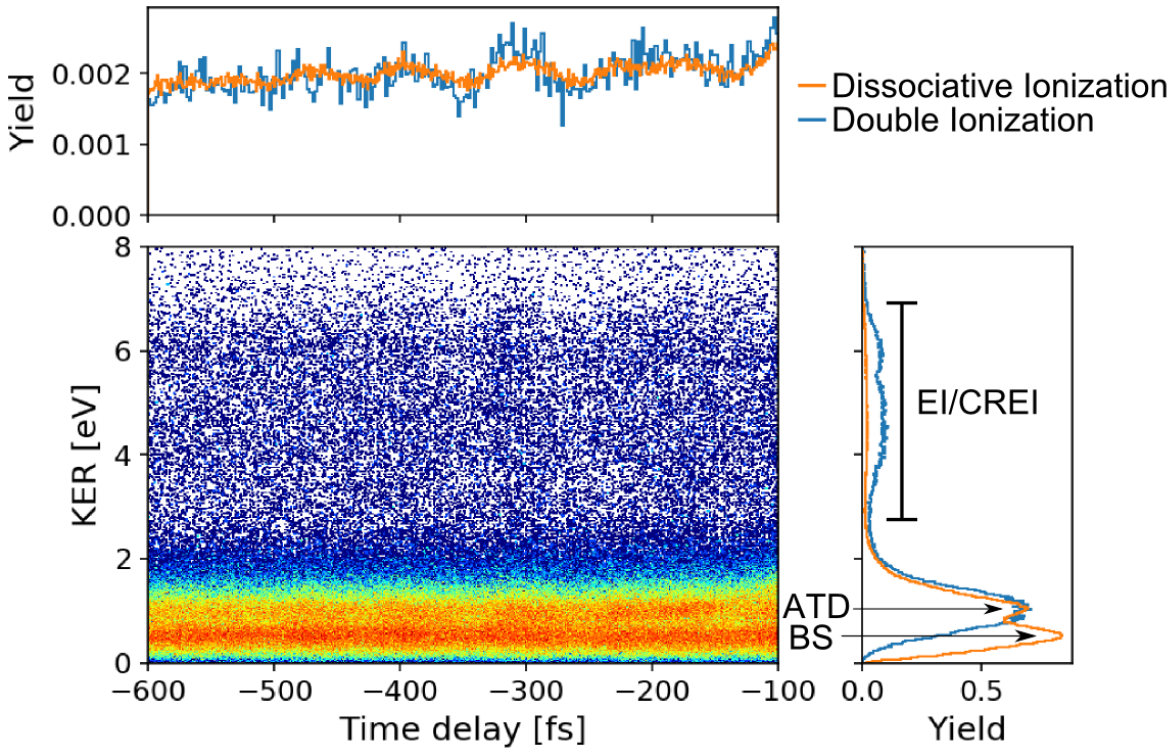

Figure 6.28.: Number of detected H^+ fragments from Dissociative and Double Ionization as a function of the the time-delay and KER. In addition the projection of the 2d-image on the x- and y-axis are plotted for the two channels individually. All projection plots were normalized to 1 for better visualization and do not represent the relative yields. BS stands for Bond-Softening.

exactly what can be seen in fig. 6.28. Here most of the double ionization events happen at large internuclear distances when the second pulse arrives, which leads to KER values that are comparable to those of the ATD because the ions do not gain a lot of additional kinetic energy during the second ionization step.

Mi *et al.* [91] reports 25 fs long laser pulses. The duration is retrieved from the FWHM of the autocorrelation trace that was recorded with the ReMi. In our pulse-shaper experiment the FWHM is roughly 60 fs and thus significantly bigger, which worsens the temporal resolution, as can be clearly seen from fig. 6.29 compared to fig. 6.27 (b) and (c). Obviously the compressed pulses after the phase shaper are longer than the pulses that leave the compressor module of the Ti:Sa laser (see 5.3 on page 58), although it is expected to obtain at least the same pulse duration as measured after the compressor unit.

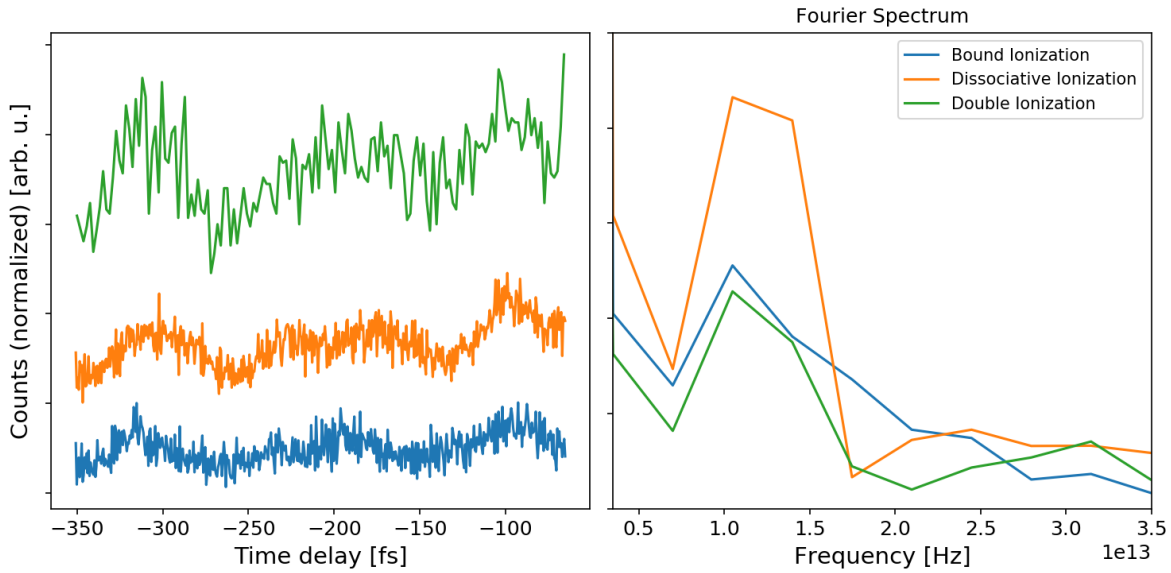

Figure 6.29.: Left: Excerpt from the autocorrelation trace for all ionization channels separately at negative time delays. At first glance the evident oscillation has a period of around 100 fs. Right: The Fourier Transform of the signals in the left plot makes clear that the observed oscillation frequencies range between 10-15 THz.

As a conclusion it is possible to generate a pump-probe scheme with the phase-shaper setup. First results show that previous Mach-Zehnder experiments with the same Ti:Sa laser setup can be reproduced in general. Nevertheless the pulse compression using the GDD-TOD scanning software (see sec. 5.2.4) does not yet deliver short enough pulses as would be expected. The reason for this is still under investigation. In the following a couple of possible reasons are given and solutions are proposed:

1. The power efficiency of the pulse shaper, meaning the ratio between ingoing and outgoing average power, depends mainly on the correct alignment of the two holographic gratings with respect to the incident laser beam. Only the first diffraction order is the most powerful one, that spectrally decomposes the beam. The power efficiency as a function of the wavelength is governed by the incidence angle. Even slight changes in this angle can favor the power efficiency of slightly different wavelengths. The holographic gratings that are used here are manufactured such, that the central wavelength is most effectively diffracted at a given angle of 10.8°. In order to optimize this angle in the setup a power meter can be used to measure the power of the first diffraction order.

2. It is of crucial importance that all the frequency components, that are split up with the first holographic grating, are perfectly recombined with the second holographic grating to form an outoing collimated laser beam. The outgoing divergence was properly checked by measuring the beam diameter directly after the pulse shaper and before the ReMi, which amounts to a distance of roughly 5 m. The beam diameter was measured using a ruler with mm-scale. It was found that the diameter stays constant over the distance of 5 m within a measurement error of 1mm. The spatial overlap of all the frequency components is more difficult to achieve. Using an IR-viewing card allows to make all wavelengths above 780 nm visible. We call this the red part of the spectrum while spectral components smaller than 780 nm are called the blue part. By changing from a normal white paper to the IR-viewing card it is possible to distinguish the spatial positions of the red and blue parts of the spectrum right after the pulse shaper and in front of the ReMi. In addition a paper can be slided through the Fourier plane. If the spectral components are recombined perfectly than only the power of the outgoing laser beam changes but not the spatial profile.

3. If the focal plane of the splitted beam does not coincide with the location of the SLM-displays, then this can worsen the wavelength resolution of the applied phase shift. Therefore special care has been taken to obey the 4f setup by measuring the according distances with a mm-scale ruler. As Kerbstadt [19, p. 137] points out, it is hard to determine the focus of the cylindrical mirrors because their long focal length produces a long rayleigh length of the focused beam.

4. Despite the careful setup and alignment of the pulse shaper it happens, that the outgoing pulses are not short/intense enough to ionize air when focused. In this case the distances of the 4f geometry are slightly adjusted until an increase in ionization can be detected. This of course can lead to the fact that the distances between the different optical components do not exactly fit to the 4f geometry anymore. A better method is to first align the 4f setup without the SLM in the beampath. Then the compressor module of the Ti:Sa laser is adjusted to produce a laser pulse after the pulse shaper, that is as short as possible. The laser beam is then coupled into the ReMi. Finally the additional dispersion due to the laser propagation in air from the pulse shaper to the ReMi and through the laser window of the ReMi is compensated using the GDD-TOD-Scanning software of the phase shaper.

7. Summary and Outlook

Electron-nuclear energy sharing

We observed the energy sharing between ions and electrons for dissociative and double ionization in form of energy conservation lines in the Joint-Energy-Spectrum. This allows to distinguish between ionization processes with different numbers of absorbed photons. In the case of dissociative ionization the number of absorbed photons can directly be deduced from the electron momentum distribution. For the double ionization channel however the observation of distinct conservation lines in the Joint-Energy-Spectrum is essential for knowing how many photons were absorbed. The ReMi is the only measurement technique that allows photon-number-selective investigation of ion and electron momentum distributions since currently it is the only available coincident and kinematically complete detection ion imaging method.

Singly excited Rydberg states and electron localization asymmetry

The main part of this thesis focuses on the role of singly excited Rydberg states in bound and dissociative ionization. Clear resonance peaks are observed in the electron energy spectrum of bound ionization and unequivocally attributed to singly excited Rydberg states (n=3,4,5,6). Thus, similar previous results by Schellhammer [12] are confirmed. By scanning the laser intensity from low to high values we are able to shift the n=4 peak in resonance and out again. This allows to give a good estimation of the laser intensity which hits the resonance best. For very low KER values (0.2-0.8 eV) the Rydberg resonances can also be observed experimentally for dissociative ionization. To confirm this observation nuclear dynamics TDSE simulations were performed. The algorithm approximates the singly-excited Rydberg potential energy curves as H_2^+ $1s\sigma_g$ states, which are slightly down-shifted in energy. The dipole coupling between the

Rydberg electron and the H_2^+ $2p\sigma_u$ continuum was completely neglected. The simulated dissociation KER distributions for the different Rydberg states showed, that the n=4 case fits best to the experimental data, whereas the H_2^+ $1s\sigma_g$ state only plays a minor role. Moreover, the findings explain why the simulations performed by Wu *et al.* [66] agree well with the experimental data only if the Franck-Condon factor distribution is upshifted by 0.8 eV. Furthermore, a KER-dependent change in the asymmetry parameter could be observed in the experiment for dissociative ionization. Using a semiclassical WKB model by Palacios *et al.* [9] and Fischer *et al.* [10] to simulate the electron localization asymmetry shows, that the observed asymmetry is caused by the singly-excited Rydberg states and not the H_2^+ $1s\sigma_g$ state.

All in all, the performed measurements and simulations reveal that Rydberg states play the dominant role in bound and dissociative ionization. Until now theoretical models have mostly excluded additional states besides the H_2^+ $1s\sigma_g$ and $2p\sigma_u$. The present findings shed new light on the ionization of H_2 and possibly also other diatomic molecules. It shows that attention has to be paid to singly excited Rydberg states for accurately modeling multiphoton ionization. When comparing with the findings by Mi *et al.* [7], it seems as if the relative importance of the Rydberg states depends on the photon energy. Therefore measurements at different wavelengths are desirable. Fechner [76, sec. 7.4] performed single-pulse ReMi measurements on H_2 using an optical parametric amplifier (OPA) to tune the central wavelength from 470-1300 nm. The findings clearly show very similar resonance peak structures in bound and dissociative ionization as presented in this thesis. However, the data are not analyzed any further in terms of nuclear-electron energy sharing and electron localization asymmetry. A review of the data by Fechner [76, sec. 7.4] is strongly suggested and planned for the near future. In order to extend the research towards laser wavelengths smaller than 400 nm, a Third-Harmonic-Generation setup is planned.

Pump-probe pulse shaper experiments

In order to achieve optimal control over the laser field and enable kinematically complete and coincident ion and electron imaging at the same time, a pulse shaper in 4f geometry was put into operation for the first time. A pump-probe experiment was carried out. The observed time-delay dependent dynamics shows the same behaviour as a previously performed Mach-Zehnder pump-probe measurement by Mi *et al.* [91]. As a conclusion the pulse-shaper setup is working correctly.

In the future measurements with even shorter pulse durations will be carried out in order to improve the temporal resolution of pump-probe-like experiments. For this a hollow core fiber filled with Argon will be implemented in front of the pulse shaper in order to spectrally broaden the Ti:Sa pulse, so the pulse duration can be reduced below 10 fs. Besides pump-probe experiments the pulse-shaper can be used to investigate quantum dynamics in polarization-tailored intense fields. This opens up new ways to look into coherent control of quantum processes by using a ReMi. It allows for example to investigate the electron localization asymmetry for different electric field configurations, such as pump-probe schemes or tailored single pulse fields. Since the asymmetry parameter can serve as a probe for determining the electronic states that contribute to dissociative ionization processes, these kind of experiments might enable new insights into the population control of different states.

A. Appendix

A.1. Derivation of electron time of flight for momentum reconstruction

Here we present how to derive eq. (5.7) from eq. (5.6).

$$
\begin{aligned}
t_e &= t_{e,d} + t_{e,a} \\
&= \frac{m_e}{eE\left(\sqrt{\left(\frac{p_{e,0,\parallel}}{eE}\right)^2 + \frac{2m_e}{eE}a} - \frac{p_{e,0,\parallel}}{eE}\right) + p_{e,0,\parallel}} d + \sqrt{\left(\frac{p_{e,0,\parallel}}{eE}\right)^2 + \frac{2m_e}{eE}a} - \frac{p_{e,0,\parallel}}{eE}
\end{aligned}
$$

With $E = U/a$:

$$
\begin{aligned}
t_e &= \frac{am_e}{eU\sqrt{\left(\frac{p_{e,0,\parallel}}{eU}\right)^2 a^2 + \frac{2m_e}{eU}a^2}} d + \sqrt{\left(\frac{p_{e,0,\parallel}}{eU}\right)^2 a^2 + \frac{2m_e}{eU}a^2} - \frac{p_{e,0,\parallel}}{eU}a \\
&= \frac{\cancel{a}m_e}{\cancel{a}eU\sqrt{\left(\frac{p_{e,0,\parallel}}{eU}\right)^2 + \frac{2m_e}{eU}}} d + a\left(\sqrt{\left(\frac{p_{e,0,\parallel}}{eU}\right)^2 + \frac{2m_e}{eU}} - \frac{p_{e,0,\parallel}}{eU}\right) \\
&= \frac{m_e}{\sqrt{p_{e,0,\parallel}^2 + 2m_e eU}} d + 2am_e \left(\underbrace{\sqrt{\left(\frac{p_{e,0,\parallel}}{2m_e eU}\right)^2 + \frac{1}{2m_e eU}} - \frac{p_{e,0,\parallel}}{2m_e eU}}_{I}\right)
\end{aligned}
\tag{A.1}
$$

Writing I as a single fraction yields

$$
I = \frac{\sqrt{p_{e,0,\parallel}^2 + 2m_e eU} - p_{e,0,\parallel}}{2m_e eU}
$$

I is of the form $I = \frac{\sqrt{a^2+b}-a}{b}$ with $a = p_{e,0,\parallel}$ and $b = 2m_e eU$. Expanding the fraction with $\sqrt{a^2+b}+a$ results in

$$\begin{aligned} I &= \frac{\left(\sqrt{a^2+b}-a\right)\left(\sqrt{a^2+b}+a\right)}{b\left(\sqrt{a^2+b}+a\right)} \\ &= \frac{\cancel{a}+\cancel{b}-\cancel{a}}{\cancel{b}\left(\sqrt{a^2+b}+a\right)} \\ &= \frac{1}{\left(\sqrt{a^2+b}+a\right)} \end{aligned} \tag{A.2}$$

Inserting eq. (A.2) into eq. (A.1) leads to eq. (5.7).

A.2. Derivation of the asymmetry parameter

By exploiting all the equations on page x and substituting them in each other we can simplify every of the two terms in eq. (2.20):

$$
\begin{aligned}
\langle\Psi_f| P_{\alpha<90^\circ} |\Psi_f\rangle =&(c_1^* \langle\Sigma_u| \langle\sigma_g| + c_2^* \langle\Sigma_g| \langle\sigma_u|) \\
&((|\Sigma_g\rangle + |\Sigma_u\rangle)(|\sigma_g\rangle + |\sigma_u\rangle)(\langle\Sigma_g| + \langle\Sigma_u|)(\langle\sigma_g| + \langle\sigma_u|) \\
&+ (|\Sigma_g\rangle - |\Sigma_u\rangle)(|\sigma_g\rangle - |\sigma_u\rangle)(\langle\Sigma_g| - \langle\Sigma_u|)(\langle\sigma_g| - \langle\sigma_u|)) \\
&(c_1 |\Sigma_u\rangle |\sigma_g\rangle + c_2 |\Sigma_g\rangle |\sigma_u\rangle) \\
=&(c_1^* \langle\Sigma_u| \langle\sigma_g| + c_2^* \langle\Sigma_g| \langle\sigma_u|) \\
&((|\Sigma_g\rangle + |\Sigma_u\rangle)(|\sigma_g\rangle + |\sigma_u\rangle)(\langle\Sigma_g| + \langle\Sigma_u|)(c_1 |\Sigma_u\rangle + c_2 |\Sigma_g\rangle) \\
&+ (|\Sigma_g\rangle - |\Sigma_u\rangle)(|\sigma_g\rangle - |\sigma_u\rangle)(\langle\Sigma_g| - \langle\Sigma_u|)(c_1 |\Sigma_u\rangle - c_2 |\Sigma_g\rangle)) \\
=&(c_1^* \langle\Sigma_u| \langle\sigma_g| + c_2^* \langle\Sigma_g| \langle\sigma_u|) \\
&((|\Sigma_g\rangle + |\Sigma_u\rangle)(|\sigma_g\rangle + |\sigma_u\rangle)(c_1 + c_2) \\
&- (|\Sigma_g\rangle - |\Sigma_u\rangle)(|\sigma_g\rangle - |\sigma_u\rangle)(c_1 + c_2)) \\
=&(c_1 + c_2)(c_1^* \langle\Sigma_u| \langle\sigma_g| + c_2^* \langle\Sigma_g| \langle\sigma_u|) \\
&((|\Sigma_g\rangle + |\Sigma_u\rangle)(|\sigma_g\rangle + |\sigma_u\rangle) \\
&- (|\Sigma_g\rangle - |\Sigma_u\rangle)(|\sigma_g\rangle - |\sigma_u\rangle)) \\
=&(c_1 + c_2) \\
&((c_1^* \langle\sigma_g| + c_2^* \langle\sigma_u|)(|\sigma_g\rangle + |\sigma_u\rangle) \\
&- (c_2^* \langle\sigma_u| - c_1^* \langle\sigma_g|)(|\sigma_g\rangle - |\sigma_u\rangle)) \\
=&2(c_1 + c_2)(c_1^* + c_2^*)
\end{aligned}
$$

$$
\begin{aligned}
\langle\Psi_f| P_{\alpha>90^\circ} |\Psi_f\rangle =&(c_1^* \langle\Sigma_u| \langle\sigma_g| + c_2^* \langle\Sigma_g| \langle\sigma_u|) \\
&((|\Sigma_g\rangle + |\Sigma_u\rangle)(|\sigma_g\rangle - |\sigma_u\rangle)(\langle\Sigma_g| + \langle\Sigma_u|)(\langle\sigma_g| - \langle\sigma_u|) \\
&+ (|\Sigma_g\rangle - |\Sigma_u\rangle)(|\sigma_g\rangle + |\sigma_u\rangle)(\langle\Sigma_g| - \langle\Sigma_u|)(\langle\sigma_g| + \langle\sigma_u|)) \\
&(c_1 |\Sigma_u\rangle |\sigma_g\rangle + c_2 |\Sigma_g\rangle |\sigma_u\rangle) \\
=&(c_1^* \langle\Sigma_u| \langle\sigma_g| + c_2^* \langle\Sigma_g| \langle\sigma_u|) \\
&((|\Sigma_g\rangle + |\Sigma_u\rangle)(|\sigma_g\rangle - |\sigma_u\rangle)(\langle\Sigma_g| + \langle\Sigma_u|)(c_1 |\Sigma_u\rangle - c_2 |\Sigma_g\rangle) \\
&+ (|\Sigma_g\rangle - |\Sigma_u\rangle)(|\sigma_g\rangle + |\sigma_u\rangle)(\langle\Sigma_g| - \langle\Sigma_u|)(c_1 |\Sigma_u\rangle + c_2 |\Sigma_g\rangle)) \\
=&(c_1^* \langle\Sigma_u| \langle\sigma_g| + c_2^* \langle\Sigma_g| \langle\sigma_u|) \\
&((|\Sigma_g\rangle + |\Sigma_u\rangle)(|\sigma_g\rangle - |\sigma_u\rangle)(c_1 - c_2) \\
&- (|\Sigma_g\rangle - |\Sigma_u\rangle)(|\sigma_g\rangle + |\sigma_u\rangle)(c_1 - c_2)) \\
=&(c_1 - c_2)(c_1^* \langle\Sigma_u| \langle\sigma_g| + c_2^* \langle\Sigma_g| \langle\sigma_u|) \\
&((|\Sigma_g\rangle + |\Sigma_u\rangle)(|\sigma_g\rangle - |\sigma_u\rangle) \\
&- (|\Sigma_g\rangle - |\Sigma_u\rangle)(|\sigma_g\rangle + |\sigma_u\rangle)) \\
=&(c_1 - c_2) \\
&((c_1^* \langle\sigma_g| + c_2^* \langle\sigma_u|)(|\sigma_g\rangle - |\sigma_u\rangle) \\
&- (c_2^* \langle\sigma_u| - c_1^* \langle\sigma_g|)(|\sigma_g\rangle + |\sigma_u\rangle)) \\
=&2(c_1 - c_2)(c_1^* - c_2^*)
\end{aligned}
$$

Finally we can calculate the asymmetry parameter:

$$
\begin{aligned}
A =& \frac{N_{\alpha>90^\circ} - N_{\alpha<90^\circ}}{N_{\alpha>90^\circ} + N_{\alpha<90^\circ}} \\
=& -\frac{(c_1 + c_2)(c_1^* + c_2^*) - (c_1 - c_2)(c_1^* - c_2^*)}{(c_1 + c_2)(c_1^* + c_2^*) + (c_1 - c_2)(c_1^* - c_2^*)} \\
=& -\frac{c_1 c_2^* + c_2 c_1^*}{c_1 c_1^* + c_2 c_2^*} \\
=& -\frac{2\mathrm{Re}[c_1 c_2^*]}{|c_1|^2 + |c_2|^2}
\end{aligned}
$$

Bibliography

1. Maiman, T. H. Stimulated Optical Radiation in Ruby. *Nature* **187,** 493–494. ISSN: 1476-4687. https://doi.org/10.1038/187493a0 (1960).

2. Spence, D. E., Kean, P. N. & Sibbett, W. 60-fsec pulse generation from a self-mode-locked Ti:sapphire laser. *Opt. Lett.* **16,** 42–44. http://ol.osa.org/abstract.cfm?URI=ol-16-1-42 (Jan. 1991).

3. Kling, M. F., Siedschlag, C., Verhoef, A. J., Khan, J. I., Schultze, M., Uphues, T., Ni, Y., Uiberacker, M., Drescher, M., Krausz, F. & Vrakking, M. J. J. Control of Electron Localization in Molecular Dissociation. *Science* **312,** 246–248. ISSN: 0036-8075. eprint: https://science.sciencemag.org/content/312/5771/246.full.pdf. https://science.sciencemag.org/content/312/5771/246 (2006).

4. Ray, D., He, F., De, S., Cao, W., Mashiko, H., Ranitovic, P., Singh, K. P., Znakovskaya, I., Thumm, U., Paulus, G. G., Kling, M. F., Litvinyuk, I. V. & Cocke, C. L. Ion-Energy Dependence of Asymmetric Dissociation of $\mathbf{D}_2$ by a Two-Color Laser Field. *Phys. Rev. Lett.* **103,** 223201. https://link.aps.org/doi/10.1103/PhysRevLett.103.223201 (22 Nov. 2009).

5. Znakovskaya, I., von den Hoff, P., Marcus, G., Zherebtsov, S., Bergues, B., Gu, X., Deng, Y., Vrakking, M. J. J., Kienberger, R., Krausz, F., de Vivie-Riedle, R. & Kling, M. F. Subcycle Controlled Charge-Directed Reactivity with Few-Cycle Midinfrared Pulses. *Phys. Rev. Lett.* **108,** 063002. https://link.aps.org/doi/10.1103/PhysRevLett.108.063002 (6 Feb. 2012).

6. Wanie, V., Ibrahim, H., Beaulieu, S., Thiré, N., Schmidt, B. E., Deng, Y., Al-naser, A. S., Litvinyuk, I. V., Tong, X.-M. & Légaré, F. Coherent control of D2/H2dissociative ionization by a mid-infrared two-color laser field. *Journal of Physics B: Atomic, Molecular and Optical Physics* **49,** 025601. https://doi.org/10.1088%2F0953-4075%2F49%2F2%2F025601 (Dec. 2015).

7. Mi, Y., Camus, N., Fechner, L., Laux, M., Moshammer, R. & Pfeifer, T. Electron-Nuclear Coupling through Autoionizing States after Strong-Field Excitation of H_2 Molecules. *Phys. Rev. Lett.* **118,** 183201. https://link.aps.org/doi/10.1103/PhysRevLett.118.183201 (18 May 2017).

8. Zhang, W., Li, H., Lin, K., Lu, P., Gong, X., Song, Q., Ji, Q., Ma, J., Li, H., Zeng, H., He, F. & Wu, J. Photon-number-resolved asymmetric dissociative single ionization of H_2. *Phys. Rev. A* **96,** 033405. https://link.aps.org/doi/10.1103/PhysRevA.96.033405 (3 Sept. 2017).

9. Palacios, A., Feist, J., González-Castrillo, A., Sanz-Vicario, J. L. & Martín, F. Autoionization of Molecular Hydrogen: Where do the Fano Lineshapes Go? *ChemPhysChem* **14,** 1456–1463. eprint: https://onlinelibrary.wiley.com/doi/pdf/10.1002/cphc.201200974. https://onlinelibrary.wiley.com/doi/abs/10.1002/cphc.201200974 (2013).

10. Fischer, A., Sperl, A., Cörlin, P., Schönwald, M., Rietz, H., Palacios, A., González-Castrillo, A., Martín, F., Pfeifer, T., Ullrich, J., Senftleben, A. & Moshammer, R. Electron Localization Involving Doubly Excited States in Broadband Extreme Ultraviolet Ionization of $\mathbf{H}_2$. *Phys. Rev. Lett.* **110,** 213002. https://link.aps.org/doi/10.1103/PhysRevLett.110.213002 (21 May 2013).

11. Ramaker, D. E. & Peek, J. M. Dipole strengths involving the lowest twenty electronic states of H+2. *Atomic Data and Nuclear Data Tables* **5,** 167–184. ISSN: 0092-640X. http://www.sciencedirect.com/science/article/pii/S0092640X73800026 (1973).

12. Schellhammer, C. *Photoionisation und Photodissoziation von Wasserstoff* PhD thesis (Physikalisches Institut Universität Freiburg, 1999). https://freidok.uni-freiburg.de/data/33.

13. Chandler, D. W. & Houston, P. L. Two-dimensional imaging of state-selected photodissociation products detected by multiphoton ionization. *The Journal of Chemical Physics* **87,** 1445–1447. eprint: https://doi.org/10.1063/1.453276. https://doi.org/10.1063/1.453276 (1987).

14. Eppink, A. T. J. B. & Parker, D. H. Velocity map imaging of ions and electrons using electrostatic lenses: Application in photoelectron and photofragment ion imaging of molecular oxygen. *Review of Scientific Instruments* **68,** 3477–3484. eprint: https://doi.org/10.1063/1.1148310. https://doi.org/10.1063/1.1148310 (1997).

15. Bayer, T., Gräfing, D., Kerbstadt, S., Pengel, D., Eickhoff, K., Englert, L. & Wollenhaupt, M. Time-resolved 3D imaging of ultrafast spin–orbit wave packet dynamics. *New Journal of Physics* **21,** 033001. https://doi.org/10.1088%2F1367-2630%2Faafb87 (Mar. 2019).

16. Tannor, D. J. & Rice, S. A. Control of selectivity of chemical reaction via control of wave packet evolution. *The Journal of Chemical Physics* **83,** 5013–5018. eprint: https://doi.org/10.1063/1.449767. https://doi.org/10.1063/1.449767 (1985).

17. Tannor, D. J., Kosloff, R. & Rice, S. A. Coherent pulse sequence induced control of selectivity of reactions: Exact quantum mechanical calculations. *The Journal of Chemical Physics* **85,** 5805–5820. eprint: https://doi.org/10.1063/1.451542. https://doi.org/10.1063/1.451542 (1986).

18. Brumer, P. & Shapiro, M. Control of unimolecular reactions using coherent light. *Chemical Physics Letters* **126,** 541–546. ISSN: 0009-2614. http://www.sciencedirect.com/science/article/pii/S0009261486801713 (1986).

19. Kerbstadt, S. *Aufbau und Charakterisierung eines hochauflösenden Polarisationspulsformers für Femtosekunden-Superkontinua* MA thesis (Carl von Ossietzky Universität Oldenburg, May 2016).

20. Zheltikov, A., L'Huillier, A. & Krausz, F. in *Springer Handbook of Lasers and Optics* (ed Träger, F.) 161–251 (Springer Berlin Heidelberg, Berlin, Heidelberg, 2012). ISBN: 978-3-642-19409-2. https://doi.org/10.1007/978-3-642-19409-2_4.

21. Boyd, R. W. in *Nonlinear Optics (Third Edition)* (ed Boyd, R. W.) Third Edition, 1–67 (Academic Press, Burlington, 2008). ISBN: 978-0-12-369470-6. http://www.sciencedirect.com/science/article/pii/B9780123694706000010.

22. New, G. *Introduction to Nonlinear Optics* (Cambridge University Press, 2011).

23. Keller, U. in *Laser Physics and Applications* (eds Herziger, G., Weber, H. & Poprawe, R.) 33–167 (Springer Berlin Heidelberg, Berlin, Heidelberg, 2007). ISBN: 978-3-540-44821-1. https://doi.org/10.1007/978-3-540-44821-1_2.

24. Koechner, W. in *Solid-State Laser Engineering* 38–101 (Springer New York, New York, NY, 2006). ISBN: 978-0-387-29338-7. https://doi.org/10.1007/0-387-29338-8_3.

25. Wollenhaupt, M., Assion, A. & Baumert, T. in *Springer Handbook of Lasers and Optics* (ed Träger, F.) 1047–1094 (Springer Berlin Heidelberg, Berlin, Heidelberg, 2012). ISBN: 978-3-642-19409-2. https://doi.org/10.1007/978-3-642-19409-2_12.

26. Grossmann, F. *Theoretical Femtosecond Physics: Atoms and Molecules in Strong Laser Fields* ISBN: 9783319006062. https://link.springer.com/book/10.1007/978-3-540-77897-4 (Springer International Publishing, 2013).

27. Hertel, I. V. & Schulz, C.-P. in *Atoms, Molecules and Optical Physics 2: Molecules and Photons - Spectroscopy and Collisions* 135–229 (Springer Berlin Heidelberg, Berlin, Heidelberg, 2015). ISBN: 978-3-642-54313-5. https://doi.org/10.1007/978-3-642-54313-5_3.

28. Mantz, A. W., Watson, J. K. G., Rao, K. N., Albritton, D. L., Schmeltekopf, A. L. & Zare, R. N. Rydberg-Klein-Rees potential for the $X^1\Sigma^+$ state of the CO molecule. *Journal of Molecular Spectroscopy* **39,** 180–184 (July 1971).

29. Fleming, H. E. & Narahari Rao, K. A simple numerical evaluation of the Rydberg-Klein-Rees integrals: Application to X $^1\Sigma^+$ state of ^{12}C ^{16}O. *Journal of Molecular Spectroscopy* **44,** 189–193 (Oct. 1972).

30. Rydberg, R. Graphical representation of some results of band spectroscopy. *Z. Phys* **73,** 376–385 (1931).

31. Klein, O. Zur Berechnung von Potentialkurven für zweiatomige Moleküle mit Hilfe von Spektraltermen. *Zeitschrift für Physik* **76,** 226–235. ISSN: 0044-3328. https://doi.org/10.1007/BF01341814 (Mar. 1932).

32. Rees, A. L. G. The calculation of potential-energy curves from band-spectroscopic data. *Proceedings of the Physical Society* **59,** 998. http://stacks.iop.org/0959-5309/59/i=6/a=310 (1947).

33. Dahl, J. P. & Springborg, M. The Morse oscillator in position space, momentum space, and phase space. *The Journal of Chemical Physics* **88,** 4535–4547. eprint: https://doi.org/10.1063/1.453761. https://doi.org/10.1063/1.453761 (1988).

34. Hertel, I. V. & Schulz, C.-P. in *Atoms, Molecules and Optical Physics 2: Molecules and Photons - Spectroscopy and Collisions* 289–381 (Springer Berlin Heidelberg, Berlin, Heidelberg, 2015). ISBN: 978-3-642-54313-5. https://doi.org/10.1007/978-3-642-54313-5_5.

35. Engelke, F. in *Aufbau der Moleküle: Eine einführung* 10–57 (Vieweg+Teubner Verlag, Wiesbaden, 1985). ISBN: 978-3-663-09932-1. https://doi.org/10.1007/978-3-663-09932-1_2.

36. Engelke, F. in *Aufbau der Moleküle: Eine einführung* 286–322 (Vieweg+Teubner Verlag, Wiesbaden, 1985). ISBN: 978-3-663-09932-1. https://doi.org/10.1007/978-3-663-09932-1_7.

37. Condon, E. U. Nuclear Motions Associated with Electron Transitions in Diatomic Molecules. *Phys. Rev.* **32,** 858–872. https://link.aps.org/doi/10.1103/PhysRev.32.858 (6 Dec. 1928).

38. Wacks, M. E. Franck-Condon Factors for the Ionization of H(2), HD, and D(2). eng. *Journal of research of the National Bureau of Standards. Section A, Physics and chemistry* **68A,** 631–633 (6 Nov. 1964).

39. Shirley, J. H. Solution of the Schrödinger Equation with a Hamiltonian Periodic in Time. *Phys. Rev.* **138,** B979–B987. https://link.aps.org/doi/10.1103/PhysRev.138.B979 (4B May 1965).

40. Kramers, H. A. Wellenmechanik und halbzahlige Quantisierung. *Zeitschrift für Physik* **39,** 828–840. ISSN: 0044-3328. https://doi.org/10.1007/BF01451751 (Oct. 1926).

41. Wentzel, G. Eine Verallgemeinerung der Quantenbedingungen für die Zwecke der Wellenmechanik. *Zeitschrift für Physik* **38,** 518–529. ISSN: 0044-3328. https://doi.org/10.1007/BF01397171 (June 1926).

42. Brillouin, L. La mécanique ondulatoire de Schrödinger; une méthode générale de resolution par approximations successives. *Compt. Rend. Hebd. Seances Acad. Sci.* **183,** 24–26 (1926).

43. Nolting, W. in *Grundkurs Theoretische Physik 5/2: Quantenmechanik - Methoden und Anwendungen* 153–235 (Springer Berlin Heidelberg, Berlin, Heidelberg, 2015). ISBN: 978-3-662-44230-2. https://doi.org/10.1007/978-3-662-44230-2_3.

44. Fischer, A. *Dissociative Photoionization of Molecular Hydrogen : A Joint Experimental and Theoretical Study of the Electron-Electron Correlations induced by XUV Photoionization and Nuclear Dynamics on IR-Laser Dressed Transition States* eng. PhD thesis (Ruprecht-Karls-Universität, Heidelberg, 2015).

45. Paulus, G. G., Nicklich, W., Xu, H., Lambropoulos, P. & Walther, H. Plateau in above threshold ionization spectra. *Phys. Rev. Lett.* **72,** 2851–2854. https://link.aps.org/doi/10.1103/PhysRevLett.72.2851 (18 May 1994).

46. Krause, J. L., Schafer, K. J. & Kulander, K. C. High-order harmonic generation from atoms and ions in the high intensity regime. *Phys. Rev. Lett.* **68,** 3535–3538. https://link.aps.org/doi/10.1103/PhysRevLett.68.3535 (24 June 1992).

47. Corkum, P. B. Plasma perspective on strong field multiphoton ionization. *Phys. Rev. Lett.* **71,** 1994–1997. https://link.aps.org/doi/10.1103/PhysRevLett.71.1994 (13 Sept. 1993).

48. Corkum, P. B., Burnett, N. H. & Brunel, F. Above-threshold ionization in the long-wavelength limit. *Phys. Rev. Lett.* **62,** 1259–1262. https://link.aps.org/doi/10.1103/PhysRevLett.62.1259 (11 Mar. 1989).

49. Kern, C., Zürch, M. & Spielmann, C. Limitations of Extreme Nonlinear Ultrafast Nanophotonics. *Nanophotonics* **4,** 303–323. https://www.degruyter.com/view/journals/nanoph/4/3/article-p303.xml (2015).

50. Brabec, T. & Krausz, F. Intense few-cycle laser fields: Frontiers of nonlinear optics. *Rev. Mod. Phys.* **72,** 545–591. https://link.aps.org/doi/10.1103/RevModPhys.72.545 (2 Apr. 2000).

51. DeWitt, M. J. & Levis, R. J. Calculating the Keldysh adiabaticity parameter for atomic, diatomic, and polyatomic molecules. *The Journal of Chemical Physics* **108,** 7739–7742. eprint: https://doi.org/10.1063/1.476208. https://doi.org/10.1063/1.476208 (1998).

52. Reiss, H. R. in *Lectures on Ultrafast Intense Laser Science 1: Volume 1* (ed Yamanouchi, K.) 41–84 (Springer Berlin Heidelberg, Berlin, Heidelberg, 2011). ISBN: 978-3-540-95944-1. https://doi.org/10.1007/978-3-540-95944-1_2.

53. Faisal, F. H. M. in *Theory of Multiphoton Processes* 29–51 (Springer US, Boston, MA, 1987). ISBN: 978-1-4899-1977-9. https://doi.org/10.1007/978-1-4899-1977-9_2.

54. Protopapas, M., Keitel, C. H. & Knight, P. L. Atomic physics with super-high intensity lasers. *Reports on Progress in Physics* **60,** 389–486. https://doi.org/10.1088%2F0034-4885%2F60%2F4%2F001 (Apr. 1997).

55. Freeman, R. R., McIlrath, T. J., Bucksbaum, P. H. & Bashkansky, M. Pondermotive effects on angular distributions of photoelectrons. *Phys. Rev. Lett.* **57,** 3156–3159. https://link.aps.org/doi/10.1103/PhysRevLett.57.3156 (25 Dec. 1986).

56. Reid, K. L. Photoelectron Angular Distributions. *Annual Review of Physical Chemistry* **54.** PMID: 12574491, 397–424. eprint: https://doi.org/10.1146/annurev.physchem.54.011002.103814. https://doi.org/10.1146/annurev.physchem.54.011002.103814 (2003).

57. Cooper, J. & Zare, R. N. Angular Distribution of Photoelectrons. *The Journal of Chemical Physics* **48,** 942–943. eprint: https://doi.org/10.1063/1.1668742. https://doi.org/10.1063/1.1668742 (1968).

58. Dill, D. Fixed-molecule photoelectron angular distributions. *The Journal of Chemical Physics* **65,** 1130–1133. eprint: https://doi.org/10.1063/1.433187. https://doi.org/10.1063/1.433187 (1976).

59. Seideman, T., Ivanov, M. Y. & Corkum, P. B. Role of Electron Localization in Intense-Field Molecular Ionization. *Phys. Rev. Lett.* **75,** 2819–2822. https://link.aps.org/doi/10.1103/PhysRevLett.75.2819 (15 Oct. 1995).

60. Zuo, T. & Bandrauk, A. D. Charge-resonance-enhanced ionization of diatomic molecular ions by intense lasers. *Phys. Rev. A* **52,** R2511–R2514. https://link.aps.org/doi/10.1103/PhysRevA.52.R2511 (4 Oct. 1995).

61. Constant, E., Stapelfeldt, H. & Corkum, P. B. Observation of Enhanced Ionization of Molecular Ions in Intense Laser Fields. *Phys. Rev. Lett.* **76,** 4140–4143. https://link.aps.org/doi/10.1103/PhysRevLett.76.4140 (22 May 1996).

62. Mulliken, R. S. Intensities of Electronic Transitions in Molecular Spectra II. Charge-Transfer Spectra. *The Journal of Chemical Physics* **7,** 20–34. eprint: https://doi.org/10.1063/1.1750319. https://doi.org/10.1063/1.1750319 (1939).

63. Brabec, T. *Strong Field Laser Physics* ISBN: 9780387400778. http://www.springer.com/de/book/9780387400778 (Springer New York, 2008).

64. Bandrauk, A. D. & Sink, M. L. Photodissociation in intense laser fields: Predissociation analogy. *The Journal of Chemical Physics* **74,** 1110–1117. eprint: https://doi.org/10.1063/1.441217. https://doi.org/10.1063/1.441217 (1981).

65. Xu, H., Li, Z., He, F., Wang, X., Atia-Tul-Noor, A., Kielpinski, D., Sang, R. T. & Litvinyuk, I. V. Observing electron localization in a dissociating H2+ molecule in real time. *Nature Communications* **8,** 15849. http://dx.doi.org/10.1038/ncomms15849 (June 2017).

66. Wu, J., Kunitski, M., Pitzer, M., Trinter, F., Schmidt, L. P. H., Jahnke, T., Magrakvelidze, M., Madsen, C. B., Madsen, L. B., Thumm, U. & Dörner, R. Electron-Nuclear Energy Sharing in Above-Threshold Multiphoton Dissociative Ionization of $\mathbf{H}_2$. *Phys. Rev. Lett.* **111,** 023002. https://link.aps.org/doi/10.1103/PhysRevLett.111.023002 (2 July 2013).

67. Lu, P., Wang, J., Li, H., Lin, K., Gong, X., Song, Q., Ji, Q., Zhang, W., Ma, J., Li, H., Zeng, H., He, F. & Wu, J. High-order above-threshold dissociation of molecules. *Proceedings of the National Academy of Sciences.* ISSN: 0027-8424. eprint: http://www.pnas.org/content/early/2018/02/12/1719481115.full.pdf. http://www.pnas.org/content/early/2018/02/12/1719481115 (2018).

68. Lu, P., Zhang, W., Gong, X., Song, Q., Lin, K., Ji, Q., Ma, J., He, F., Zeng, H. & Wu, J. Electron-nuclear correlation in above-threshold double ionization of molecules. *Phys. Rev. A* **95,** 033404. https://link.aps.org/doi/10.1103/PhysRevA.95.033404 (Mar. 2017).

69. Strickland, D. & Mourou, G. Compression of amplified chirped optical pulses. *Optics Communications* **55,** 447–449. ISSN: 0030-4018. http://www.sciencedirect.com/science/article/pii/0030401885901518 (1985).

70. Chériaux, G. in *Strong Field Laser Physics* (ed Brabec, T.) 17–34 (Springer New York, New York, NY, 2009). ISBN: 978-0-387-34755-4. https://doi.org/10.1007/978-0-387-34755-4_2.

71. Sala, K., Kenney-Wallace, G. & Hall, G. CW autocorrelation measurements of picosecond laser pulses. *IEEE Journal of Quantum Electronics* **16,** 990–996 (1980).

72. *SLM-S640d USB/Ethernet* Jenoptik Optical Systems HmbH (Goeschwitzer Strasse 25, 07745 Jena, Jan. 2018).

73. Zhang, S., Ma, X., Liu, H., Li, B. & Zhu, X. Properties and applications of cold supersonic gas jet. *Science in China Series G: Physics, Mechanics and Astronomy* **49,** 709–715. ISSN: 1862-2844. https://doi.org/10.1007/s11433-006-2014-y (Dec. 2006).

74. Scoles, G., Miller, D., Gentry, W., Pauly, H., Bassi, D., U.Hefter, Bergman, K., Zen, M., Reuss, J., Meijdenberg, C., Abuerbach, D., Kappes, M., Leutwyler, S., Valbusa, U., Buck, U., Lee, Y., Dagdigian, P., Stolte, S., Düren, R. & Iannotta, S. *Atomic and Molecular Beam Methods: Vol. 1* ISBN: 0 -10-504280-8 (Jan. 1998).

75. Morse, M. D. Supersonic Beam Sources. *Experimental Methods in the Physical Sciences* **29.** Atomic, Molecular, and Optical Physics: Atoms and Molecules, 21–47. ISSN: 1079-4042. http://www.sciencedirect.com/science/article/pii/S0076695X0860784X (1996).

76. Fechner, L. *High resolution experiments on strong-field ionization of atoms and molecules: test of tunneling theory, the role of doubly excited states, and channel-selective electron spectra* PhD thesis (Ruprecht-Karls-Universität, Heidelberg, 2014). https://pure.mpg.de/pubman/faces/ViewItemFullPage.jsp?itemId=item_2075736_1.

77. GmbH, R. H. *The fADC8 fast sampling ADC unit* Accessed: 20.07.2020 (). http://www.roentdek.com/products/electronics_description/fADC8%20%20description.pdf.

78. Ullrich, J., Moshammer, R., Dorn, A., Dörner, R., Schmidt, L. P. H. & Schmidt-Böcking, H. Recoil-ion and electron momentum spectroscopy: reaction-microscopes. *Reports on Progress in Physics* **66,** 1463. http://stacks.iop.org/0034-4885/66/i=9/a=203 (2003).

79. Dörner, R., Mergel, V., Jagutzki, O., Spielberger, L., Ullrich, J., Moshammer, R. & Schmidt-Böcking, H. Cold Target Recoil Ion Momentum Spectroscopy: a 'momentum microscope' to view atomic collision dynamics. *Physics Reports* **330,** 95–192. ISSN: 0370-1573. http://www.sciencedirect.com/science/article/pii/S037015739900109X (2000).

80. Sharp, T. Potential-energy curves for molecular hydrogen and its ions. *Atomic Data and Nuclear Data Tables* **2,** 119–169. ISSN: 0092-640X. http://www.sciencedirect.com/science/article/pii/S0092640X70800079 (1970).

81. Baier, S. *Numerische Simulationen zur Einfach- und Doppelionisation von H_2 in kurzen intensiven Laserpulsen* PhD thesis (Fakultät für Physik der Universität Bielefeld, Nov. 2008).

82. Gong, X., He, P., Song, Q., Ji, Q., Pan, H., Ding, J., He, F., Zeng, H. & Wu, J. Two-Dimensional Directional Proton Emission in Dissociative Ionization of H_2. *Phys. Rev. Lett.* **113,** 203001. https://link.aps.org/doi/10.1103/PhysRevLett.113.203001 (20 Nov. 2014).

83. Xie, X., Roither, S., Kartashov, D., Persson, E., Arbó, D. G., Zhang, L., Gräfe, S., Schöffler, M. S., Burgdörfer, J., Baltu ška, A. & Kitzler, M. Attosecond Probe of Valence-Electron Wave Packets by Subcycle Sculpted Laser Fields. *Phys. Rev. Lett.* **108,** 193004. https://link.aps.org/doi/10.1103/PhysRevLett.108.193004 (19 May 2012).

84. Martín, F., Fernández, J., Havermeier, T., Foucar, L., Weber, T., Kreidi, K., Schöffler, M., Schmidt, L., Jahnke, T., Jagutzki, O., Czasch, A., Benis, E. P., Osipov, T., Landers, A. L., Belkacem, A., Prior, M. H., Schmidt-Böcking, H., Cocke, C. L. & Dörner, R. Single Photon-Induced Symmetry Breaking of H2 Dissociation. *Science* **315,** 629–633. ISSN: 0036-8075. eprint: https://science.sciencemag.org/content/315/5812/629.full.pdf. https://science.sciencemag.org/content/315/5812/629 (2007).

85. Shapiro, M. & Bony, H. Scattering theory of photodissociation in strong laser fields: Photon induced predissociation in IBr. *The Journal of Chemical Physics* **83,** 1588–1598. eprint: https://doi.org/10.1063/1.449395. https://doi.org/10.1063/1.449395 (1985).

86. Sussman, B. J., Ivanov, M. Y. & Stolow, A. Nonperturbative quantum control via the nonresonant dynamic Stark effect. *Phys. Rev. A* **71,** 051401. https://link.aps.org/doi/10.1103/PhysRevA.71.051401 (5 May 2005).

87. Sussman, B. J., Townsend, D., Ivanov, M. Y. & Stolow, A. Dynamic Stark Control of Photochemical Processes. *Science* **314,** 278–281. ISSN: 0036-8075. eprint: https://science.sciencemag.org/content/314/5797/278.full.pdf. https://science.sciencemag.org/content/314/5797/278 (2006).

88. Kerbstadt, S., Eickhoff, K., Bayer, T. & Wollenhaupt, M. Odd electron wave packets from cycloidal ultrashort laser fields. *Nature Communications* **10,** 658. ISSN: 2041-1723. https://doi.org/10.1038/s41467-019-08601-7 (2019).

89. Pengel, D., Kerbstadt, S., Englert, L., Bayer, T. & Wollenhaupt, M. Control of three-dimensional electron vortices from femtosecond multiphoton ionization. *Phys. Rev. A* **96,** 043426. https://link.aps.org/doi/10.1103/PhysRevA.96.043426 (4 Oct. 2017).

90. Odenweller, M., Lower, J., Pahl, K., Schütt, M., Wu, J., Cole, K., Vredenborg, A., Schmidt, L. P., Neumann, N., Titze, J., Jahnke, T., Meckel, M., Kunitski, M., Havermeier, T., Voss, S., Schöffler, M., Sann, H., Voigtsberger, J., Schmidt-Böcking, H. & Dörner, R. Electron emission from H_2^+ in strong laser fields. *Phys. Rev. A* **89,** 013424. `https://link.aps.org/doi/10.1103/PhysRevA.89.013424` (1 Jan. 2014).

91. Mi, Y., Peng, P., Camus, N., Sun, X., Fross, P., Martinez, D., Dube, Z., Cokrkum, P. B., Villeneuve, D. M., Staudte, A., Moshammer, R. & Pfeifer, T. Clocking enhanced ionization of hydrogen molecules with rotational wavepackets. *Submitted as Letter to Physical Review Letters; Not published yet* (May 2020).

Danksagung

Vielen Dank für deine immer währende Hilfsbereitschaft und deine beeindruckend hilfreichen Ratschläge, Robert. Dein intuitives und bildhaftes Verständnis von scheinbar komlizierter Physik hat mir so manches Aha-Erlebnis beschert! Unter all den zahlreichen Annehmlichkeiten, die deine Arbeitsgruppe bietet, habe ich eines immer ganz besonders geschätzt und genossen: Dein unkomplizierter und freundschaftlicher Umgang mit mir. Mit dir über Physik und Experimente zu diskutieren hat genau die selbe Leichtigkeit wie ein erfrischendes, humorvolles Gespräch mit guten Freunden. Nur dadurch ist die Arbeit an physikalischer Forschung erst zu einer richtigen Leidenschaft für mich geworden. Dafür danke ich dir von ganzem Herzen!

Dein grenzenloser Optimismus und deine stete Freundlichkeit waren mir wahrlich Balsam für die Seele, Thomas. Selbst in Momenten, in denen ich an meiner eigenen Arbeit vollends gezweifelt habe, hast du mir ehrliches grenzenloses Interesse entgegen gebracht. Das war für mich in vielen Augenblicken eine Quelle der Motivation und fachlicher Erkenntnis! Dafür mein herzlichstes Dankeschön an dich!

Nicolas Camus habe ich von der Durchführung der Experimente bis zur Datenauswertung sehr viel zu verdanken. Du hast mir die Arbeit mit Femtolasern, Reaktionsmikroskopen, der Datenerhebung, der Dateninterpretation, usw. erst beigebracht. Ohne dich wäre das hier alles nicht gelungen! Vielen Dank!

Ein herzliches Dankeschön an Stefanie Kerbstadt. Durch deinen immensen Fleiß, deine unermüdliche, engagierte Arbeit, deine stete Hilfs- und Einsatzbereitschaft sowie dein großes Talent für Physik ist der Pulse-Shaper erst zustande gekommen. Das ist größtenteils dein Verdienst! Vielen lieben Dank an dich!

Vielen Dank auch an dich, Denhi Martinez für die stets kollegiale, ausdauernde und freundliche Arbeit mit dir. Als Leidensgenossen in Sachen Laseralignment und Pulse-Shaper haben wir viel Zeit zusammen im Labor verbracht und Erfolge, sowie Misserfolge geteilt.

Ein herzliches Dankeschön auch an dich, Claus-Dieter. Als kompetenteste Fachkraft für alle praktischen Belange rund um unsere Experimentieranlagen war auf deine Ein-

schätzungen und Ratschläge stets Verlass.

Ich danke meinem Prüfungskomitee, bestehend aus Priv.-Doz. Dr. Robert Moshammer, apl. Prof. Dr. Andreas Wolf, Prof. Dr. Lorenz S. Cederbaum und Prof. Dr. Matthias Weidemüller und allen Korrekturleser/innen für ihre Bereitschaft.

Alle Arbeitskolleginnen und -kollegen hier aufzuzählen, die mir in der ein oder anderen Art und Weise hilfreich während meiner Promotion waren, wäre an dieser Stelle zu viel. Für alle kleinen und großen Hilfen, an die ich mich teilweise auch gar nicht mehr erinnere, möchte ich ebenso meine verbundene Dankbarkeit aussprechen.